

# Tuning the classical spin-liquid behaviour in a triangular-lattice, dipolar, Ising antiferromagnet

A. Smerald<sup>1\*</sup>, F. Mila<sup>1</sup>

<sup>1</sup> Institute of Physics, Ecole Polytechnique Fédérale de Lausanne (EPFL), CH-1015  
Lausanne, Switzerland

\* andrew.smerald@gmail.com

May 16, 2022

## Abstract

We study the triangular-lattice Ising model with dipolar interactions, inspired by its realisation in artificial arrays of nanomagnets. We show that a classical spin-liquid forms at intermediate temperatures, and that its behaviour can be tuned by temperature and/or a small lattice distortion between a “weakly-coupled” string Luttinger liquid and a “strongly-coupled” domain-wall-network state. We also study the transition out of the spin liquid, and show that the critical physics can be tuned between first order, Kasteleyn and 2D Ising transitions, with an intermediate Pokrovsky-Talapov tricritical point. The dipolar model is analysed using Monte Carlo simulations, guided by exact and perturbative solutions of related toy models and a phenomenological theory written in terms of spinless fermions.

---

## Contents

<b>1</b>	<b>Introduction</b>	<b>3</b>
<b>2</b>	<b>Useful mappings</b>	<b>6</b>
2.1	Mapping to dimer coverings of the dual lattice	6
2.2	Mapping to string configurations on the dual lattice	6
2.3	Winding number sectors	8
<b>3</b>	<b>Main physical features of the dipolar TLIAF</b>	<b>9</b>
3.1	Monte Carlo simulation method	9
3.2	Dipolar model on the isotropic triangular lattice	10
3.3	Dipolar model on the anisotropic triangular lattice	12
<b>4</b>	<b>Toy models</b>	<b>13</b>
4.1	$J_{1A}$ - $J_{1B}$ model with a constrained manifold	13
4.1.1	Dimer mapping	14
4.1.2	Evaluation of the partition function	14
4.1.3	Physical properties	16
4.1.4	Correlations	17

4.1.5	Mapping to 1D quantum model	19
4.2	$J_{1A}$ - $J_{1B}$ model with an unconstrained manifold	20
4.2.1	Dimer mapping	20
4.2.2	Evaluation of the partition function	21
4.2.3	Physical properties	22
4.2.4	Phase diagram and correlations	24
4.2.5	Mapping to 1D quantum model	25
4.3	$J_{1A}$ - $J_{1B}$ - $J_2$ model with a constrained manifold	27
4.3.1	General considerations	27
4.3.2	Diagrammatic perturbation theory	28
4.3.3	Phase diagram determined from Monte Carlo simulations	34
4.3.4	Monte Carlo simulations in the 2-string sector	35
4.3.5	Mapping to 1D quantum model and correlations	36
<b>5</b>	<b>Phenomenological theory of the phase transition</b>	<b>38</b>
5.1	Pokrovsky-Talapov second-order transition	38
5.2	Pokrovsky-Talapov to Ising crossover	40
5.3	Pokrovsky-Talapov/Ising tricritical point	41
5.4	Pokrovsky-Talapov first-order transition	43
<b>6</b>	<b>Universality and correlation in the Dipolar TLIAF</b>	<b>45</b>
6.1	Universality of phase transitions	45
6.2	Correlations between spins	47
<b>7</b>	<b>Discussion and Conclusion</b>	<b>51</b>
<b>A</b>	<b>Defect triangles in the dipolar TLIAF</b>	<b>54</b>
<b>B</b>	<b>The spin-spin correlation function for the nearest-neighbour TLIAF</b>	<b>55</b>
B.1	Spin-spin correlations in the constrained manifold	56
B.1.1	Correlations perpendicular to the strings	57
B.1.2	Correlations parallel to the strings	58
B.2	Spin-spin correlations in the unconstrained manifold	59
<b>C</b>	<b>Mapping between the 2D Kasteleyn partition function and a 1D fermionic coherent-state path integral</b>	<b>61</b>
C.1	Kasteleyn action in 4-site basis	62
C.2	Fermionic coherent-state path integral	63
C.3	Matching the fermionic and Kasteleyn actions	65
C.4	Matching the classical and quantum spectrums	66
<b>D</b>	<b>Perturbative expansion of the action: a simple example</b>	<b>67</b>
	<b>References</b>	<b>69</b>

---

## 1 Introduction

Spin liquids, which can be found in both quantum and classical systems, are often defined by the absence of symmetry breaking at low temperature. This raises the question of what *is* happening at low temperature, and the variety of possible behaviour is comparable to that of the vast array of symmetry-broken phases [1].

One of the oldest and best-understood examples of a classical spin liquid is the Ising model on the triangular lattice with nearest-neighbour interactions. It has been known for many years that this fails to order even at zero temperature [2, 3], instead forming a critical state with long-range, algebraic spin correlations [4, 5]. The key feature of the spin liquid is that there is robust local ordering associated with the requirement that every triangle has only two equivalent spins, but there are exponentially many configurations that respect this local order, resulting in long-range disorder [2].

This behaviour is not confined to  $T = 0$ , but holds to a good approximation throughout the region  $0 \leq T \lesssim J_1$ , where  $J_1$  is the nearest-neighbour coupling constant. For  $T > 0$  the correlations between spins are exponentially rather than algebraically decaying, but the correlation length remains large within the low-temperature region. The whole region  $0 \leq T \leq J_1$  can therefore be considered as a spin-liquid, and weakly-correlated, paramagnetic behaviour only occurs for  $T > J_1$ .

The reason that the nearest-neighbour, triangular-lattice, Ising antiferromagnet (TLIAF) is so well understood is that it can be mapped onto a 1D model of free spinless fermions [2, 4, 6]. This almost magical transformation converts a strongly-interacting spin problem into a non-interacting fermion problem, thus making possible the calculation of virtually all quantities of interest directly in the thermodynamic limit. The key to this “magic” is that the constraints imposed by the strong interactions between spins map directly to the Pauli exclusion principle, and can therefore be dealt with trivially in the fermionic picture.

The situation becomes more difficult, and more interesting, when additional interactions couple spins beyond nearest neighbour. Further-neighbour interactions tend to stabilise an ordered phase at temperatures below a characteristic, further-neighbour energy scale,  $J_{\text{fn}}$  [7, 8, 9, 10, 11], but this leaves open the possibility of spin-liquid behaviour in the temperature window  $J_{\text{fn}} \lesssim T \lesssim J_1$ .

The difficulty in analysing further-neighbour models is due to the fact that they cannot be mapped onto free-fermion models, and therefore lack simple analytical solutions. Nevertheless, the fermion picture can still provide useful insights, and in particular one can classify different regions of the spin liquid as being weakly or strongly coupled in a fermionic sense. Weak coupling can be expected for  $J_{\text{fn}} \ll T < J_1$  where the free-fermion model is only weakly perturbed, and therefore one expects to find the 2D classical equivalent of a Luttinger liquid. On the other hand, for  $T \sim J_{\text{fn}}$  the fermionic model is strongly coupled, making simple predictions more difficult.

There is an essentially infinite number of ways to include further-neighbour interactions, and rather than trying to study all possible combinations of couplings, we concentrate on dipolar coupling between spins, where the interactions fall off with the cube of the separation. Nevertheless, we suggest that the results we obtain are very likely to be qualitatively correct for any system in which the coupling constants are monotonically decreasing with distance (if this condition is not respected there are other possibilities [10, 11]). The Hamiltonian we

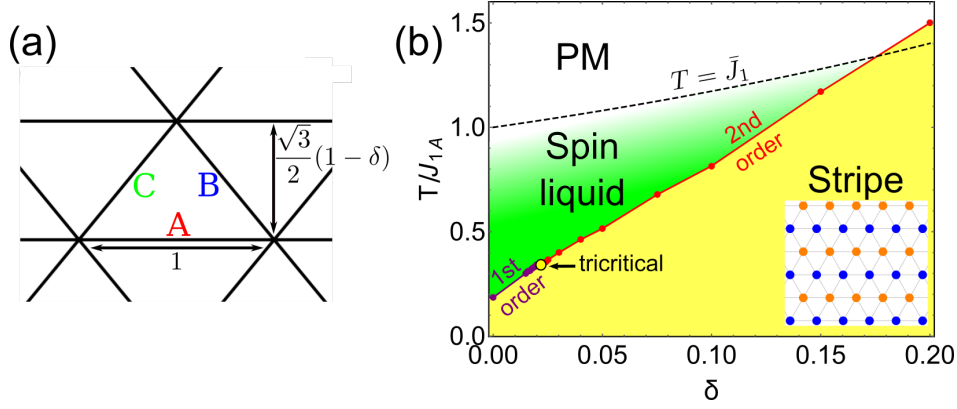


Figure 1: The phase diagram of the dipolar, triangular-lattice, Ising antiferromagnet,  $\mathcal{H}_{\text{dip}}$  [Eq. 1], with distortion parameter  $\delta$ . (a) Triangular-lattice bonds are labelled A, B and C and the distortion is such that the length of A bonds remains invariant while the height of each triangle is reduced by a factor  $1 - \delta$ , thus shrinking B and C bonds equally. (b) A strongly-correlated spin liquid is separated by a phase transition from a low-temperature stripe-ordered state and a crosses over to a high-temperature, weakly-correlated paramagnet at  $T \sim \bar{J}_1$  [Eq. 2]. The spin-liquid temperature window narrows with increasing  $\delta$  since the transition temperature increases faster than that of the crossover. The nature of the phase transition depends on  $\delta$ , and changes from first to second order via a tricritical point.

consider is therefore given by,

$$\mathcal{H}_{\text{dip}} = \sum_{(i,j)} J_{ij} \sigma_i \sigma_j, \quad J_{ij} = \frac{1}{|\mathbf{r}_i - \mathbf{r}_j|^3}, \quad (1)$$

where  $\sigma_i = \pm 1$  denotes an Ising spin at site  $i$ , the sum over  $(i, j)$  includes all possible pairs of spins with  $i \neq j$  and  $\mathbf{r}_i$  is the position of the  $i$ th spin.

Our choice to concentrate on dipolar interactions is not made at random, but is motivated by experiment. In particular, artificial spin systems consisting of arrays of nano-magnets arranged on a triangular lattice are starting to be fabricated, and these realise the dipolar TLIAF to a very good approximation [12, 13]. While artificial systems have been studied for a number of years [14, 15, 16, 17, 18, 19, 20, 21, 22, 23], recent advances have made it possible to make the nano-dots small enough that they remain thermally active at experimentally viable temperatures [24, 25], motivating our study of the equilibrium properties of  $\mathcal{H}_{\text{dip}}$  [Eq. 1].

While the primary experimental motivation comes from artificial spin systems, it is worth pointing out that there are many other realisations of TLIAFs with further-neighbour couplings. Examples include crystals of trapped ions [26], the disordered lattice structure of the spin-orbital liquid candidate material  $\text{Ba}_3\text{Sb}_2\text{CuO}_9$  [27] and frustrated Coulomb liquids [28].

The only tuneable parameter in  $\mathcal{H}_{\text{dip}}$  [Eq. 1] is the temperature, and this already leads to a wide variety of behaviour. Nevertheless, we also consider a second tuneable parameter, namely a small lattice distortion associated with squeezing the lattice. The distortion is parametrised by  $\delta$  and shown in Fig. 1, and is chosen both for its experimental convenience and theoretical interest. Experimentally, artificial spin systems can be fabricated to realise a vast variety of lattice structures, and therefore lattices with this type of distortion are relatively simple to construct [13]. Theoretically, the distortion increases the ordering temperature and therefore the spin-liquid state just above the transition crosses over from strong to weak coupling, with important consequences for the critical behaviour.



As a foretaste of the results to come, we show in Fig. 1 a simplified phase diagram of  $\mathcal{H}_{\text{dip}}$  [Eq. 1] as a function of  $T$  and  $\delta$ . It can be seen that there is a strongly-correlated spin-liquid region sandwiched between an ordered stripe phase and a weakly correlated paramagnet, and the nature of this spin-liquid regime will be one of the main focuses of this article.

The boundary between the spin-liquid and the paramagnet is a crossover and not a phase transition, and a naive guess puts this crossover at  $T \approx \bar{J}_1$ , where,

$$\bar{J}_1 = \frac{J_{1A} + J_{1B} + J_{1C}}{3}, \quad (2)$$

and  $J_{1A}$ ,  $J_{1B}$  and  $J_{1C}$  refer to nearest-neighbour interactions along A, B and C bonds (see Fig. 1 for bond labelling). We provide better ways of determining the boundary between the spin-liquid and paramagnetic regions below, but find that they essentially agree with the simple estimate given by  $\bar{J}_1$ .

It can also be seen that the phase transition changes from first to second order via a tricritical point, and understanding the nature of the critical behaviour will be the other main focus of this article.

The process by which we uncover the nature of the spin-liquid and critical behaviour are summarised below.

In Section 2 a review is given of different ways of representing Ising configurations on the triangular lattice. This includes mappings onto both dimer and string configurations on the dual honeycomb lattice, and these form the basis of most of the physical discussion throughout the remainder of the paper, as well as being useful starting points for calculations.

In Section 3 we present the basic physics of  $\mathcal{H}_{\text{dip}}$  [Eq. 1] using Monte Carlo simulation and determine the phase diagram. This section “sets the scene” for the more detailed investigation that follows.

In Section 4 we study a number of toy models constructed so as to isolate one or more of the characteristic features of the dipolar TLIAF. This includes the nearest-neighbour TLIAF, which can be solved exactly by mapping to a fermion model, as well as the TLIAF with first and second neighbour interactions, which we study by a combination of perturbation theory and Monte Carlo simulation. The motivation is that the intuition gained from studying relatively simple models can then be used to better understand the dipolar TLIAF.

In Section 5 we construct a phenomenological theory of the phase transition that ties together the different types of critical behaviour observed in the dipolar TLIAF phase diagram. We use this to make predictions for the critical behaviour and in particular to construct scaling hypotheses that can be used to analyse simulation data.

In Section 6 we return to  $\mathcal{H}_{\text{dip}}$  [Eq. 1] and carry out a detailed study of the phase transition, critical behaviour and spin-liquid region. This is performed using Monte Carlo simulation, and the analysis of these simulations uses the intuition gained by studying toy models in Section 4 and the predictions of the phenomenological theory constructed in Section 5.

Finally in Section 7 we discuss the main features of the dipolar TLIAF in a more intuitive manner and attempt to tease out the universal feature of TLIAFs with further-neighbour interactions.

While the article is designed to be read in a continuous fashion, the reader who is more interested in knowing what are the physical features of the dipolar TLIAF, and less in the details of why this is the case, is advised to concentrate in particular on Section 3 and Section 6, with occasional reference to the other sections when prompted in the text.

## 2 Useful mappings

The TLIAF has been the subject of research for many years, and a variety of different ways of representing the Ising configurations have been proposed. Here we review two representations, consisting of dimer and string configurations on the dual lattice. These will be made use of throughout the remainder of this article. We also review the related concept of winding number sectors.

It is useful to define two different manifolds of Ising configurations. The first contains all possible Ising configurations on the triangular lattice, and we refer to it as the unconstrained manifold. The second contains those configurations that are ground states of the nearest-neighbour TLIAF and therefore have no defect triangles (defined as triangles with three equivalent spins), and we refer to this as the constrained manifold. This manifold contains an extensive number of states, one consequence of which is that the zero temperature entropy of the nearest-neighbour TLIAF is finite [2].

### 2.1 Mapping to dimer coverings of the dual lattice

One of the most useful mappings is from Ising configurations on the triangular lattice to dimer configurations on the dual honeycomb lattice [29] (see Fig. 2). The dual honeycomb lattice is constructed such that its bonds cut exactly one bond of the original triangular lattice (and vice versa). If the triangular-lattice bond has two equivalent spins, then the honeycomb-lattice bond is covered by a dimer, while if the spins are inequivalent the honeycomb-lattice bond is left empty. The mapping between spin and dimer configurations is  $2 \rightarrow 1$ , since the dimer configuration is unaffected by a global flip of all the Ising spins.

Configurations within the constrained manifold (i.e. ground states of the nearest-neighbour TLIAF model) have one ferromagnetic bond per triangle, and therefore the number of dimers is fixed and equal to the number of triangular lattice sites,  $N$ . It follows that sites on the honeycomb lattice respect the usual dimer model constraint of being covered by exactly one dimer, as shown in Fig. 2(a).

In the unconstrained manifold, for each pair of defect triangles there are two additional dimers, and therefore the number of dimers is not fixed. The honeycomb-lattice site at the centre of a defect triangle is covered by three dimers, and therefore does not respect the usual dimer model constraint (see Fig. 2(b)).

For the unconstrained manifold of Ising configurations an alternative dimer mapping is possible, which is constructed such that the number of dimers is fixed and each site obeys the usual dimer-model constraint of being covered by exactly one dimer [30]. This involves extending the honeycomb lattice such that every original site is replaced by three new sites arranged in a triangle (see Fig. 2). Dimers are then placed on the original honeycomb lattice bonds in the same way as before, leaving a unique way of dimer covering the remaining sites of the extended honeycomb lattice such that every site is covered exactly once.

### 2.2 Mapping to string configurations on the dual lattice

A second useful mapping is onto string configurations on the dual honeycomb lattice [31, 32], and these strings will be referred to extensively throughout the article (see Fig. 3). One way to generate such a mapping is to first map the Ising configuration to the dimer configuration on the dual honeycomb lattice (as in Fig. 2) and then to compare this to a fixed reference

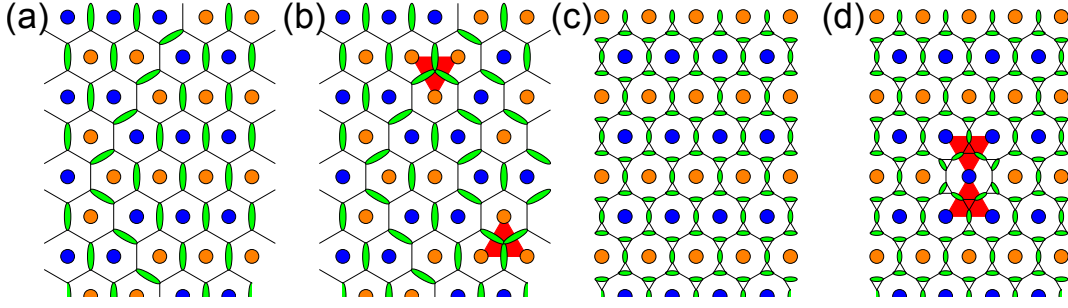


Figure 2: Mapping between Ising configurations on the triangular lattice and dimer configurations on the honeycomb and extended honeycomb lattices. (a) There is a correspondence between bonds of the triangular and honeycomb lattices, and this is used to define a honeycomb-lattice dimer model. If the spins are aligned on the triangular-lattice bond, the associated honeycomb bond is covered by a dimer. If the spins are opposite, then the honeycomb bond is empty. In the ground state of the nearest-neighbour TLIAF all honeycomb vertices are covered by one dimer (i.e. the model is hardcore). (b) The presence of defect triangles (coloured red) results in honeycomb sites that are covered with three dimers. (c) and (d) In order to obtain a dimer model that is hardcore for all Ising configurations the honeycomb lattice can be extended by the Fisher construction [30].

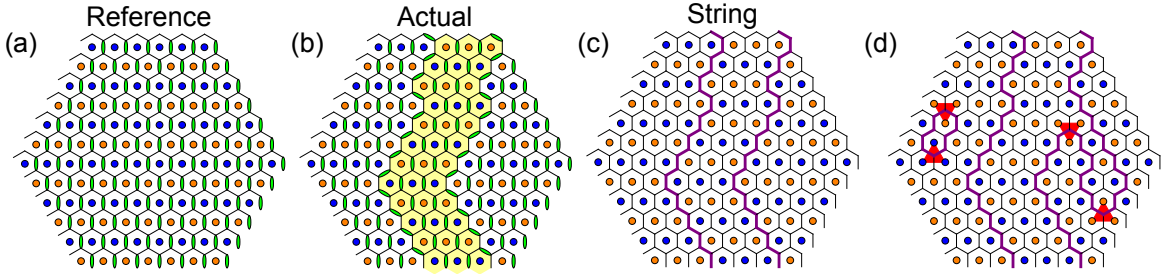


Figure 3: Mapping between Ising configurations on the triangular lattice and string configurations on the honeycomb lattice. (a) Reference Ising configuration. (b) A configuration of interest. Spins that differ from the reference configuration are highlighted in yellow. (c) The configuration of interest can be specified (up to a global spin flip) by a set of strings (purple), which measure the difference in dimer covering between the actual and reference configurations. These strings are always non-crossing, and for configurations within the constrained manifold are directed in the sense that they never turn back on themselves, and therefore wind the system. (d) Defect triangles (red) act as sources and sinks of pairs of strings, and allow strings to turn back on themselves.

state. Any honeycomb-lattice bonds on which there is a discrepancy between the actual dimer configuration and the reference configuration is assigned to be part of a string.

The chosen reference configuration consists of alternating horizontal stripes of aligned Ising spins, and this corresponds to all vertical bonds of the honeycomb lattice being covered by dimers (see Fig. 3(b)). This choice of reference configuration results in a number of useful properties of the strings, the most important of which is that strings never touch or cross (referred to from now on as the non-crossing constraint). For periodic boundary conditions there is the additional constraint that the number of strings crossing an arbitrary reference line that winds the system has to be even, meaning that the string parity is conserved. If the Ising configurations are restricted to be in the constrained manifold the strings are directed, in the sense that they cannot turn back on themselves, and therefore have to wind the system, as shown in Fig. 3(c). In the unconstrained manifold defect triangles act as sources and sinks of pairs of strings, resulting in (non-winding) closed loops of strings as well as strings that turn back on themselves, as shown in Fig. 3(d).

### 2.3 Winding number sectors

In the presence of periodic boundary conditions, Ising configurations within the constrained manifold can be labelled by a pair of winding numbers.

One way to define the winding numbers,  $\mathbf{W} = (W_1, W_2)$ , is to consider a pair of reference lines, as shown in Fig. 4. For each dimer crossing the horizontal part of the reference line the winding number is augmented by  $+1$ , and for each dimer crossing the angled part of the reference line it is augmented by  $-1$ . For hexagonal clusters of linear size  $L$  with  $N = 3L^2$  triangular-lattice sites, the allowed winding number sectors form a triangle with vertices at  $\mathbf{W} = (L, L)$ ,  $\mathbf{W} = (0, -L)$  and  $\mathbf{W} = (-L, 0)$ . Within this triangle, all even values of  $W_1$  and  $W_2$  are allowed.

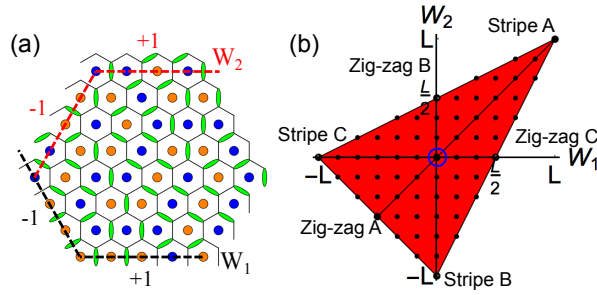


Figure 4: Winding numbers sectors of the triangular-lattice Ising antiferromagnet (reproduced from [11]). (a) A pair of reference lines is defined on hexagonal clusters with periodic boundary conditions, and the dimer crossing of these lines gives the winding number  $\mathbf{W} = (W_1, W_2)$ . Dimers crossing the horizontal lines increase  $W_i$  by 1, while those crossing angled lines decrease  $W_i$  by 1. This is simply related to the number of strings crossing the reference lines by Eq. 3. (b) The allowed winding number sectors for an  $L = 12$  cluster are shown by black dots.  $W_1$  and  $W_2$  are both even, and lie within a triangle with vertices at  $\mathbf{W} = (L, L)$ ,  $\mathbf{W} = (-L, 0)$  and  $\mathbf{W} = (0, -L)$ .

In the string picture, the winding number is simply given by,

$$\begin{aligned} W_1 &= L - \text{no. strings crossing ref line 1} \\ W_2 &= L - \text{no. strings crossing ref line 2,} \end{aligned} \quad (3)$$

and it follows that the density of strings for a hexagonal cluster can be defined as,

$$n_{\text{string}} = \frac{2}{3} - \frac{W_1 + W_2}{3L}. \quad (4)$$

in the constrained manifold. The string vacuum is therefore equivalent to the winding number sector  $\mathbf{W} = (L, L)$  and the sector  $\mathbf{W} = (0, 0)$  corresponds to a density  $n_{\text{string}} = 2/3$ .

The winding numbers split the constrained manifold into topological sectors, in the sense that it is not possible to move between configurations with different winding numbers by making a series of local spin flips. Instead it is necessary to flip clusters of spins that wind the system.

In the unconstrained manifold (defect triangles allowed)  $\mathbf{W}$  remains a useful quantity, but is no longer strictly a winding number, since the creation of a pair of defect triangles on the reference line is a local move that alters  $\mathbf{W}$ . Nevertheless, we continue to refer to it as a winding number in presence of a low-density of defect triangles, since this provides physically useful insights into the workings of the Monte Carlo algorithms discussed in Section 3.

### 3 Main physical features of the dipolar TLIAF

Here we provide an overview of the main physical features of the dipolar TLIAF using Monte Carlo simulations. This involves determining the phase diagram as a function of temperature,  $T$ , and distortion parameter,  $\delta$ , and using the density of defect triangles as a rough guide to the extent of the spin-liquid region. The section can be considered as “setting the scene” for a foray into analytical theory in Section 4 and 5, which will then be used to guide a more detailed Monte-Carlo based analysis of the dipolar model in Section 6.

#### 3.1 Monte Carlo simulation method

Monte Carlo is the standard way to simulate 2D Ising systems, but in the case of the dipolar TLIAF proves difficult to equilibriate. As a result we use a combination of update methods, including parallel tempering, single-spin-flip updates and worm updates.

The problem with equilibration is most acute for the isotropic triangular lattice ( $\delta = 0$ ), where simulations are complicated by the vanishingly small density of defect triangles at the ordering temperature. In consequence local-update algorithms (e.g. single-spin-flip) become stuck in a single winding number sector and therefore have problems with freezing.

Instead we use a worm algorithm [33, 34, 35] that works with dimer configurations on the dual honeycomb lattice [36, 37, 11, 38] (see Fig. 2 for definition of dimer configurations). Loops of honeycomb-lattice bonds are constructed taking into account the local interactions, and then the nature of each bond on the loop is exchanged such that dimer-covered bonds become empty and vice versa. This has the effect of flipping all Ising spins contained within the loop.

For systems with local interactions (e.g. up to 5th neighbour) the loops of the worm algorithm can be constructed such that detailed balance is automatically obeyed, and therefore the algorithm is rejection free [11]. However, for dipolar interactions the construction of rejection-free updates is prohibitively time consuming. Instead we create worm updates that take into account interactions up to third neighbour, and then accept or reject these based on the residual energy difference, using the Metropolis prescription. The loop creation depends on three parameters,  $J_1^{\text{worm}}$ ,  $J_2^{\text{worm}}$  and  $J_3^{\text{worm}}$ , that are not necessarily equal to the first, second and third-neighbour dipolar couplings, but are chosen so as to optimise the performance of the algorithm. Even so, equilibration is difficult close to the phase transition due to the jump in the winding number from  $\mathbf{W} \approx (0, 0)$  to  $\mathbf{W} \approx (L, L)$ . In consequence  $J_1^{\text{worm}}$ ,  $J_2^{\text{worm}}$  and  $J_3^{\text{worm}}$  have to be chosen very carefully, and equilibration is achieved by choosing values that result in the residual ground-state energy being at the centre of the Gaussian peak of residual energies associated with the high-temperature side of the transition. To further aid equilibration parallel tempering is also used.

Small distortions of the triangular lattice (see Fig. 1) increase the transition temperature, and, above a critical threshold, drive the transition second order. The higher transition temperature results in a higher density of defect triangles at the transition, and thus makes it easier to move between winding-number sectors. In consequence it is possible to simulate the system using a single-spin-flip algorithm combined with parallel tempering.

Simulations are run on hexagonal clusters that preserve all the symmetries of the triangular lattice and have periodic boundary conditions. The linear size of the clusters is  $L$  and the total number of triangular-lattice sites is  $N = 3L^2$ . For the dipolar TLIAF we typically use clusters sizes of  $L = 24$ ,  $L = 36$  and  $L = 48$ . Ewald summation is used to take into account

the slow decay of the dipolar interactions [39].

When performing Monte Carlo simulations a number of physical quantities are sampled. As well as the energy,  $E$ , and heat capacity,  $C$ , this includes the stripe order parameter,

$$m_{\text{stripe}} = \frac{1}{N} \sqrt{\sum_{\alpha} \left( \sum_i \tau_i^{\alpha} \sigma_i \right)^2} \quad (5)$$

where  $\alpha \in \{A, B, C\}$ ,  $i$  labels triangular lattice sites and  $\tau_i^{\alpha}$  is the spin at the  $i$ th site for perfect stripe order parallel to the  $\alpha$  bond direction. The associated susceptibility is given by,

$$\chi_{\text{stripe}} = \frac{N}{T} (\langle m_{\text{stripe}}^2 \rangle - \langle m_{\text{stripe}} \rangle^2). \quad (6)$$

It is also useful to track the triangular average of the winding number, given by,

$$W_{\text{tri}} = \frac{1}{L} \sqrt{W_1^2 - W_1 W_2 + W_2^2}. \quad (7)$$

This is designed such that  $W_{\text{tri}} = 1$  for  $\mathbf{W} = (L, L)$ ,  $\mathbf{W} = (-L, 0)$  and  $\mathbf{W} = (0, -L)$ , while  $W_{\text{tri}} = 0$  for  $\mathbf{W} = (0, 0)$ . The associated susceptibility is,

$$\chi_{\text{W}} = \frac{L}{T} (\langle W_{\text{tri}}^2 \rangle - \langle W_{\text{tri}} \rangle^2). \quad (8)$$

Alternatively one can track the Monte Carlo average of the density of strings,  $n_{\text{string}}$ , which in the constrained manifold is related to the winding number,  $\mathbf{W}$ , according to Eq. 4.

### 3.2 Dipolar model on the isotropic triangular lattice

Having constructed a Monte Carlo update algorithm, we first use it to study the isotropic, dipolar TLIAF (i.e.  $\delta = 0$ ).

The ground state is 6-fold degenerate and consists of alternating stripes of equivalent Ising spins running parallel to A, B or C bonds (see Fig. 1). The 3-fold degeneracy associated with the choice of stripe direction is multiplied by a 2-fold Ising degeneracy associated with a global spin flip, giving the overall 6-fold degeneracy.

At low temperature there is a stripe-ordered phase, which is dominated by the ground state configurations. Local fluctuations are highly suppressed because they involve the creation of pairs of defect triangles, and the associated energy cost is large. In principle it is also possible to create strings that wind the system, but these are forbidden in the thermodynamic limit as they cost a finite free energy per unit length [10, 11].

On further increasing the temperature, there is a transition from the stripe phase into a disordered phase. A previous study determined the transition temperature to be  $T/J_1 \approx 0.18$ , but was not able to determine the nature of the transition or achieve equilibration across the transition [40]. Our simulations, which do achieve equilibration, show that the transition is first order, and this is clear from histogram analysis of the energy close to the transition temperature, as shown in Fig. 5. The transition temperature can be determined from the peak in the heat capacity,  $C$ , the order parameter susceptibility  $\chi_{\text{stripe}}$  [Eq. 6] or the winding number susceptibility  $\chi_{\text{W}}$  [Eq. 8]. The positions of the peaks in these different quantities coincide for a given system size,  $L$ , and we show results for  $\chi_{\text{W}}$  in Fig. 5. The position of the



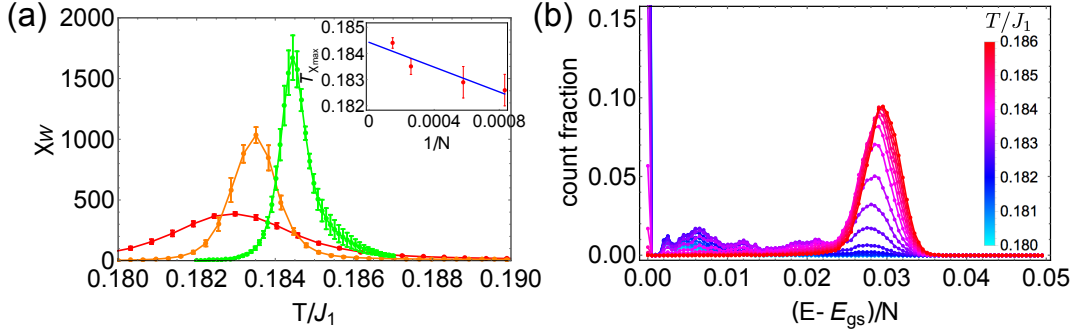


Figure 5: Monte Carlo simulations probing the phase transition in  $\mathcal{H}_{\text{dip}}$  [Eq. 1]. (a) The winding number susceptibility,  $\chi_W$  [Eq. 8], is shown in a narrow temperature window surrounding the transition for hexagonal clusters of size  $L = 24$  (red),  $L = 36$  (orange) and  $L = 48$  (green). (Inset) The maximum of  $\chi_W$  scales approximately with  $1/N$ , as is standard for a 1st order phase transition, leading to our estimate that in the thermodynamic limit the transition temperature is  $T_1/J_1 = 0.1845 \pm 0.0010$ . (b) Energy-histogram analysis of an  $L = 36$  cluster for temperatures close to the  $\chi_W$ -maximum of  $T_1/J_1 \approx 0.183$ . Energies are measured in units of  $J_1$  and energy bins have width  $0.0005J_1$ . A sharp low-energy peak, associated with an almost fluctuationless low-temperature phase, is separated from a Gaussian peak associated with the high-temperature phase by an energy gap of approximately  $0.03J_1$  per site. The separation of the two peaks is evidence of a first-order transition.

peak shows a weak  $L$  dependence, and using the standard scaling of a first-order transition temperature with  $1/N$ , we determine a transition temperature of  $T_1/J_1 = 0.1845 \pm 0.0010$ .

Above the transition the system forms a highly-correlated spin liquid, which crosses over at higher temperatures to a weakly-correlated paramagnet. Since the correlations in the spin liquid are driven by the approximately-realised local constraint that triangles should not have three equivalent spins, measurement of the density of defect triangles provides a better guide to the temperature of the crossover than the first-neighbour coupling  $J_1$ .

The density of defect triangles,  $n_{\text{def}}$ , can be defined as the total number of triangular plaquettes with three equivalent spins divided by the total number of plaquettes,  $2N$ , and simulation results for this quantity are shown in Fig. 6. Just above the transition temperature the density is very low, and at  $T/J_1 = 0.2$ , one finds  $n_{\text{def}} \approx 10^{-4}$ . On the other hand, in the uncorrelated, infinite-temperature limit the defect-triangle density saturates at  $n_{\text{def}} = 0.25$ , since triangles can take 8 possible equally probable configurations, 2 of which have three spins aligned. We consider strong correlation to be associated with a defect-triangle density of less than 10% of the saturation value (i.e.  $n_{\text{def}} < 0.025$ ) and this occurs in the temperature range  $T_1 < T < 0.75J_1$ .

It is possible to estimate the typical energy of an isolated defect triangle by making fits to  $n_{\text{def}}$  in the temperature range  $T \lesssim J_1$ . This shows activated behaviour, with functional form,

$$n_{\text{def}} = \frac{Ae^{-\frac{E_{\text{def}}}{T}}}{1 + e^{-\frac{E_{\text{def}}}{T}}}, \quad (9)$$

where  $E_{\text{def}}$  is the typical energy of a defect triangle (see Appendix A for a crude justification of this expression). The best fit is shown in Fig. 6 and we find  $A = 0.23$  and  $E_{\text{def}} = 1.57J_1$ . This shows that one effect of the further-neighbour interactions is to slightly decrease the typical energy of a defect triangle relative to the nearest-neighbour TLIAF where  $E_{\text{def}} = 2J_1$ .



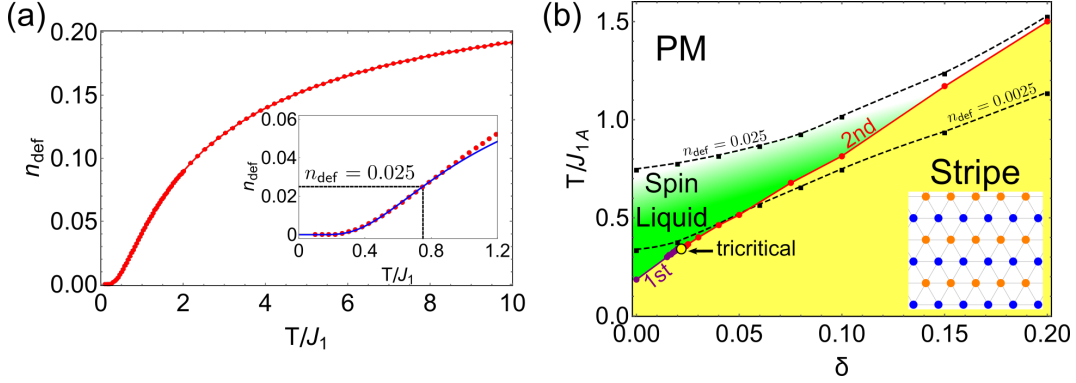


Figure 6: The density of defect triangles,  $n_{\text{def}}$ , and the phase diagram of the dipolar, triangular-lattice Ising antiferromagnet,  $\mathcal{H}_{\text{dip}}$  [Eq. 1]. (a) Monte Carlo measurement of  $n_{\text{def}}$  in the isotropic, dipolar TLIAF on an  $L = 24$  hexagonal cluster. Error bars are smaller than the point size. (Inset) At low temperatures  $n_{\text{def}}$  follows an activated behaviour, and the blue line is the best fit to Eq. 9, with  $A = 0.23$  and  $E_{\text{def}} = 1.57$  (see Appendix A for a justification of Eq. 9). (b) The phase diagram as a function of  $T$  and  $\delta$ , as determined from Monte Carlo simulation. The nature of the phase transition changes from first to second order at  $\delta = 0.022$  via a tricritical point. The crossover from spin-liquid to paramagnetic (PM) behaviour is taken to be at  $n_{\text{def}} = 0.025$  (10% of the saturation value) and also shown is the line where  $n_{\text{def}} = 0.0025$  (1% of the saturation value).

### 3.3 Dipolar model on the anisotropic triangular lattice

Next we turn to the distorted triangular lattice, and show that even quite small distortions can lead to significant changes in the physical behaviour compared to the isotropic lattice.

The distortion, which is parameterised by  $\delta$ , leaves the length of A bonds invariant, while reducing the length of B and C bonds and therefore breaks the 6-fold ground-state degeneracy of the isotropic lattice down to a 2-fold degeneracy. Stripes form parallel to A bonds, and the 2-fold degeneracy is simply due to an Ising degree of freedom, associated with a global flip of all the spins.

As in the isotropic case, the transition from the stripe phase to the disordered phase can be located using the peaks in the heat capacity,  $C$ , the order parameter susceptibility  $\chi_{\text{stripe}}$  [Eq. 6] or the winding number susceptibility  $\chi_{\text{W}}$  [Eq. 8], and the result of this is shown in Fig. 6. Histogram analysis of both  $n_{\text{string}}$  and  $E$  show that the transition changes from first order at low  $\delta$  to second order at high  $\delta$ , and the change occurs at  $\delta_{\text{tri}} \approx 0.02$ . However, this type of analysis is not a very precise gauge of  $\delta_{\text{tri}}$ , due to both finite-size effects and the fact that the first-order nature of the transition becomes weaker approaching  $\delta_{\text{tri}}$ . In Section 6 we use finite-size scaling analysis to determine how the critical exponents depend on  $\delta$ , and thus demonstrate that the change from first to second order occurs via a tricritical point located at  $\delta = \delta_{\text{tri}} = 0.022$  and  $T = T_{\text{tri}} = 0.343$ . It is also worth noting that the nature of the second-order phase transition changes with increasing  $\delta$ , and this will be analysed in Section 6, after developing a related analytic theory in Section 4 and Section 5.

The spin-liquid region, in which strong local correlation co-exists with long-range disorder, is found to extend until approximately  $\delta \gtrsim 0.15$ , with the associated temperature window decreasing with increasing  $\delta$ . This is shown in Fig. 6, where a defect-triangle density,  $n_{\text{def}}$ , of 10% of the saturation value is taken to signify the upper extent of the spin liquid. The nature of the correlations will be investigated more thoroughly in Section 6, and we will show that the region is far from uniform in its behaviour.

Also shown in Fig. 6 is the temperature at which the defect-triangle density reaches 1%

of the saturation value. In the ordered phase this can be used as a rough guide for where fluctuations become significant, and it can be seen that, even close to the phase transition, the system is essentially fluctuationless when  $\delta \lesssim 0.1$ . As will be shown below, the presence of significant fluctuations close to the transition indicates a change in the critical behaviour.

## 4 Toy models

The dipolar TLIAF is complicated due to the many competing interactions, and this makes it difficult to determine which features of the model lead to which physical consequences. In this section we study a number of toy models, each of which is designed to reproduce a subset of the physical features of the dipolar TLIAF, and thus allow these features to be studied in a simpler setting. The models we study are also simple enough that they can be solved either exactly or approximately by analytical means, which makes possible a deeper understanding of the physical features. The insights gained from this will be used to provide a more detailed analysis of the dipolar model in Section 6.

The first model we study is the TLIAF with anisotropic nearest-neighbour interactions and a constraint forbidding defect triangles. The features of this model are already well known due to the mapping to free fermions, and were studied by Wannier in the case of isotropic interactions [2], and can be transformed to the Kasteleyn model for anisotropic interactions [29]. The purpose of revisiting this model is to remind the reader of the nature of the correlations in the spin-liquid phase and of the Pokrovsky-Talapov critical behaviour [41, 42]. This will be relevant to the dipolar model at  $\delta_{\text{tri}} < \delta \lesssim 0.1$ , where the further-neighbour interactions will turn out to be relatively unimportant.

The next toy model we consider is the TLIAF with anisotropic nearest-neighbour interactions but now with defect triangles allowed (i.e. in the unconstrained manifold). This makes it possible to study the crossover between a spin liquid and a weakly-correlated paramagnet, and the presence of defect triangles also has implications for the phase transition and spin-spin correlation function.

The last model we study consists of a TLIAF with first and second-neighbour interactions and a constraint forbidding defect triangles, and this is the simplest example of a model with further-neighbour interactions. The presence of further-neighbour couplings means that it doesn't map onto a free fermion model, but instead fermion-fermion interactions need to be taken into account. We will study how this affects the phase transition and how it changes the behaviour of the spin-liquid region.

### 4.1 $J_{1A}$ - $J_{1B}$ model with a constrained manifold

The first and simplest toy model we consider has a Hamiltonian given by,

$$\mathcal{H}_{\text{ABB}} = J_{1A} \sum_{\langle ij \rangle_A} \sigma_i \sigma_j + J_{1B} \sum_{\langle ij \rangle_B} \sigma_i \sigma_j + J_{1C} \sum_{\langle ij \rangle_C} \sigma_i \sigma_j, \quad (10)$$

where  $\langle ij \rangle_\alpha$  denotes nearest-neighbour bonds in the  $\alpha$  direction (see Fig. 1 for the definition of bond directions). An alternative parametrisation can be achieved by writing,

$$J_{1B} = J_{1A} + \delta J, \quad (11)$$

and we consider the case  $\delta J > 0$  (equivalently  $J_{1A} < J_{1B}$ ). We also impose the constraint that defect triangles are forbidden, which corresponds to taking the limit  $J_{1A}/\delta J \rightarrow \infty$ .

#### 4.1.1 Dimer mapping

$\mathcal{H}_{ABB}$  [Eq. 10] can be mapped onto the Kasteleyn model of dimer coverings of the honeycomb lattice, which has an exact solution [29]. The mapping from Ising spins on the triangular lattice to dimers on the dual honeycomb lattice is described in Section 2.1, and the energy of a dimer configuration is given by,

$$E_{ABB} = -\frac{1}{3}(J_{1A} + 2J_{1B})N_{\text{bond}} + 2J_{1A}N_{\text{dim}}^A + 2J_{1B}(N_{\text{dim}}^B + N_{\text{dim}}^C), \quad (12)$$

where  $N_{\text{bond}} = 3N$  is the total number of bonds (this is the same for the triangular and dual honeycomb lattices) and  $N_{\text{dim}}^\alpha$  is the number of dimers covering  $\alpha$ -type bonds. Since defect triangles are forbidden, the total number of dimers is fixed as  $N_{\text{dim}}^A + N_{\text{dim}}^B + N_{\text{dim}}^C = N_{\text{bond}}/3$ . In the ground state  $N_{\text{dim}}^A = N_{\text{bond}}/3$  and  $N_{\text{dim}}^B = N_{\text{dim}}^C = 0$ , and therefore the energy of a given configuration relative to the ground state energy is,

$$\Delta E_{ABB} = 2 \delta J (N_{\text{dim}}^B + N_{\text{dim}}^C). \quad (13)$$

It follows that the partition function can be written, up to a configuration independent prefactor, as,

$$\mathcal{Z}_{ABB} \propto \mathcal{Z}_{\text{hon}} = \sum_{\text{dimer cov}} z^{N_{\text{dim}}^B + N_{\text{dim}}^C}, \quad (14)$$

where the sum is over all dimer coverings of the honeycomb lattice. It can be seen from Eq. 13 that the weight associated with dimer covering a B or C bond is given by,

$$z = e^{-\frac{2\delta J}{T}}. \quad (15)$$

#### 4.1.2 Evaluation of the partition function

It has been known how to evaluate partition functions of the type  $\mathcal{Z}_{\text{hon}}$  [Eq. 14] for many years [29, 6]. Here we will briefly sketch the solution, since it will prove a useful basis from which to consider more complicated models.

The starting point is to introduce a real, anticommuting Grassmann variable at each site of the honeycomb lattice [6, 43, 44]. These variables obey the usual rules:  $a_i a_j = -a_j a_i$ ,  $\int da_i = 0$  and  $\int da_i a_i = 1$ . Since the honeycomb lattice has a 2-site basis, it is useful to label Grassmann variables as  $a$  and  $b$  on the two sublattices, and the partition function is therefore given by,

$$\mathcal{Z}_{\text{hon}} = \int \prod_i da_i db_i e^{\mathcal{S}_2[a,b]} = \det K, \quad \mathcal{S}_2[a,b] = \sum_{ij} a_i K_{ij} b_j, \quad (16)$$

where  $i$  labels unit cells and  $\mathcal{S}_2[a,b]$  is the Kasteleyn action. Here  $K$  is a signed adjacency matrix, known as the Kasteleyn matrix [29], and contains the weights  $z$  [Eq. 15]. The reason for the appearance of  $\det K$  rather than the more usual Pfaffian is that the matrix connects sites on different sublattices, but not those on the same sublattice.

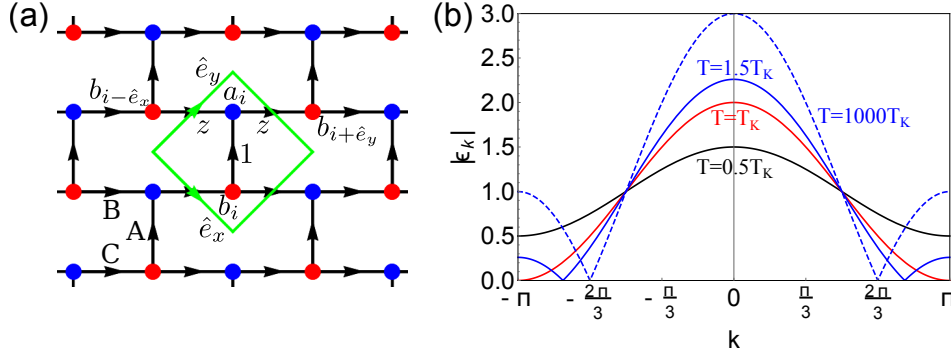


Figure 7: The brick lattice and Kasteleyn-matrix spectrum,  $|\epsilon_{\mathbf{k}}|$  [Eq. 22], for  $\mathcal{H}_{\text{ABB}}$  [Eq. 10] in the constrained manifold. (a) Bond directions (black arrows) are chosen so as to respect Kasteleyn's theorem [29], and bond weights are chosen to be  $z$  on B and C bonds and 1 on A bonds, in accordance with  $\mathcal{Z}_{\text{hon}}$  [Eq. 14]. The  $i$ th unit cell (green) contains two sites with associated Grassmann variables  $a_i$  (blue) and  $b_i$  (red). The translation vectors of the unit cell are  $\hat{e}_x$  and  $\hat{e}_y$ , and these are taken to be unit length. (b) The spectrum  $|\epsilon_{\mathbf{k}}|$  is shown along the path  $\mathbf{k} = (k, k + \pi)$ . For  $T < T_K$  (black) the spectrum is gapped at all  $\mathbf{k}$ , and this corresponds to the stripe-ordered phase. At  $T = T_K$  (red) the gap closes at  $\mathbf{k} = (\pi, 0)$  and a Kasteleyn transition occurs. For  $T > T_K$  (blue) the gapless point migrates from  $\mathbf{k} = (\pi, 0)$  to  $\mathbf{k} = (2\pi/3, -\pi/3)$  with increasing temperature, and the location of this gap is related to the density of strings,  $n_{\text{string}}$  [Eq. 25].

To simplify the geometry the honeycomb lattice is distorted into the brick lattice, as shown in Fig. 7. Bonds are assigned a direction in accordance with the Kasteleyn theorem, which states that transition cycles should have an odd number of arrows in each sense [29]. The bond weights are assigned according to Eq. 14, with weight 1 on A bonds and weight  $z$  on B and C bonds. It follows that the action can be written as,

$$\mathcal{S}_2[a, b] = \sum_i (za_i b_{i+\hat{e}_y} + zb_{i-\hat{e}_x} a_i + b_i a_i), \quad (17)$$

where the coordinate system is defined by the unit vectors  $\hat{e}_x$  and  $\hat{e}_y$ , as shown in Fig. 7. The action is simply diagonalised by taking the Fourier Transform,

$$a_i = \frac{1}{\sqrt{N}} \sum_{\mathbf{k}} a_{\mathbf{k}} e^{i\mathbf{k}\cdot\mathbf{r}_i} e^{-i\frac{k_x - k_y}{2}}, \quad b_i = \frac{1}{\sqrt{N}} \sum_{\mathbf{k}} b_{\mathbf{k}} e^{i\mathbf{k}\cdot\mathbf{r}_i}, \quad (18)$$

to give,

$$\mathcal{S}_2[a, b] = \sum_{\mathbf{k}} \epsilon_{\mathbf{k}} a_{\mathbf{k}} b_{-\mathbf{k}}, \quad (19)$$

where,

$$\epsilon_{\mathbf{k}} = -2iz \sin \left[ \frac{k_x + k_y}{2} \right] - e^{-i\frac{k_x - k_y}{2}}. \quad (20)$$

Finally the partition function can be evaluated as,

$$\mathcal{Z}_{\text{hon}} = \prod_{\mathbf{k}} \epsilon_{\mathbf{k}} = \prod_{\mathbf{k}} \sqrt{\epsilon_{\mathbf{k}} \epsilon_{-\mathbf{k}}} = \prod_{\mathbf{k}} |\epsilon_{\mathbf{k}}|, \quad (21)$$

where  $\epsilon_{\mathbf{k}}^* = \epsilon_{-\mathbf{k}}$  has been used, and,

$$|\epsilon_{\mathbf{k}}| = \sqrt{1 + 2z(\cos k_x - \cos k_y) + 2z^2(1 - \cos[k_x + k_y])}. \quad (22)$$

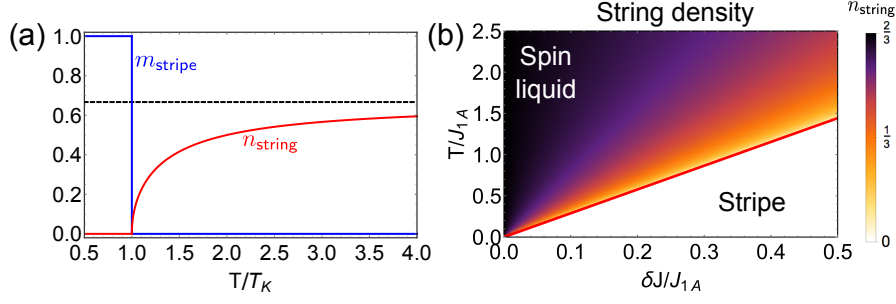


Figure 8: The string density,  $n_{\text{string}}$  [red, Eq. 30], and the phase diagram for  $\mathcal{H}_{\text{ABB}}$  [Eq. 10] in the constrained manifold. (a) Comparison between  $n_{\text{string}}$  [red, Eq. 30] and the stripe order parameter,  $m_{\text{stripe}}$  [blue, Eq. 5].  $m_{\text{stripe}}$  shows a step-like behaviour at the critical point,  $T = T_{\text{K}}$ , while  $n_{\text{string}}$  has Pokrovsky-Talapov critical behaviour, with  $n_{\text{string}} \propto (T - T_{\text{K}})^{\beta}$  and  $\beta = 1/2$  for small  $T - T_{\text{K}} > 0$ . In the limit  $T \rightarrow \infty$  it saturates at  $n_{\text{string}} = 2/3$ . (b) The phase diagram showing stripe and spin-liquid phases separated by a second-order transition at  $T = T_{\text{K}}$  [Eq. 24], and overlaid with the string density,  $n_{\text{string}}$  [Eq. 25].

### 4.1.3 Physical properties

In order to understand better the physical properties of  $\mathcal{H}_{\text{ABB}}$  [Eq. 10] it is useful to notice that the free energy, which is given by,

$$\mathcal{F}_{\text{hon}} = -T \log \mathcal{Z}_{\text{hon}} = -T \sum_{\mathbf{k}} \log |\epsilon_{\mathbf{k}}|, \quad (23)$$

is typically dominated by the minimal values of  $|\epsilon_{\mathbf{k}}|$ . The physical characteristics of the system are therefore determined predominantly by the “low-energy” part of  $|\epsilon_{\mathbf{k}}|$ .

At low temperature, the spectrum of  $|\epsilon_{\mathbf{k}}|$  is gapped at all  $\mathbf{k}$ , as shown in Fig. 7, and this corresponds to the stripe-ordered state. The gap closes at  $\mathbf{k} = (\pi, 0)$  at the temperature,

$$2z(T_{\text{K}}) = 1, \quad T_{\text{K}} = \frac{2\delta J}{\log 2}, \quad (24)$$

and this corresponds to the temperature at which the free energy of strings goes to zero (see Section 2.2 for the definition of strings).

At  $T = T_{\text{K}}$  strings condense into the system, and there is a Kasteleyn transition out of the stripe-ordered phase and into the spin liquid. This is second order due to the non-crossing constraint of the strings, which results in an entropically-driven string-string repulsion. The transition is in the Pokrovsky-Talapov universality class [41, 42].

For all  $T > T_{\text{K}}$  the spectrum of  $|\epsilon_{\mathbf{k}}|$  is gapless. The position of the gapless point moves from  $\mathbf{k} = (\pi, 0)$  at  $T = T_{\text{K}}$  to  $\mathbf{k} = (2\pi/3, -\pi/3)$  at  $T \rightarrow \infty$  and the position of this point is simply related to the string density, which smoothly increases with increasing temperature. We show below that the gaplessness of the spectrum is associated with algebraic decay of the spin-spin correlations [4, 5].

In order to detect the transition between the stripe-ordered phase and the paramagnet, one possibility is to measure the local stripe order parameter  $m_{\text{stripe}}$  [Eq. 5]. However, this is somewhat unsatisfactory, since  $m_{\text{stripe}} = 1$  in the ordered phase, and there is a discontinuous jump to  $m_{\text{stripe}} = 0$  at  $T = T_{\text{K}}$  (see Fig. 8). Thus  $m_{\text{stripe}}$  does not show critical behaviour, and this is due to the fact that the transition is not driven by the proliferation of local defects, but by strings that wind the system.

A more useful physical quantity is the density of strings,  $n_{\text{string}}$ , and this does show critical behaviour. However, unlike a conventional order parameter,  $n_{\text{string}} = 0$  in the ordered phase, and only takes a finite value for  $T > T_K$ . It can most simply be calculated in terms of dimer densities, according to,

$$n_{\text{string}} = \frac{1}{2} + \frac{\langle N_{\text{dim}}^{\text{B}} + N_{\text{dim}}^{\text{C}} - N_{\text{dim}}^{\text{A}} \rangle}{2N}, \quad (25)$$

where the normalisation is such that  $0 \leq n_{\text{string}} \leq 1$ . In the case of the constrained manifold, the total number of dimers is fixed (see Section 4.1.1) and this leads to the simplified expression [31],

$$n_{\text{string}} = \frac{\langle N_{\text{dim}}^{\text{B}} + N_{\text{dim}}^{\text{C}} \rangle}{N} = \frac{z}{N} \frac{\partial \log \mathcal{Z}_{\text{hon}}}{\partial z} = \frac{1}{N} \sum_{\mathbf{k}} \frac{z}{|\epsilon_{\mathbf{k}}|} \frac{\partial |\epsilon_{\mathbf{k}}|}{\partial z}, \quad (26)$$

where the second equality follows from the expression for  $\mathcal{Z}_{\text{hon}}$  [Eq. 14].

When working in the constrained manifold, the string density can be calculated in a simple closed form. Substituting the expression for  $|\epsilon_{\mathbf{k}}|$  [Eq. 22] into  $n_{\text{string}}$  [Eq. 26], making the change of variables  $p_x = (k_x + k_y - \pi)/2$  and  $p_y = (k_x - k_y - \pi)/2$ , and taking the thermodynamic limit results in,

$$\begin{aligned} n_{\text{string}} &= \frac{1}{\pi^2} \int_0^\pi dp_x \int_0^\pi dp_y \frac{4z^2 \cos^2 p_x - 2z \cos p_x \cos p_y}{1 - 4z \cos p_x \cos p_y + 4z^2 \cos^2 p_x} \\ &= \frac{1}{\pi^2} \int_0^\pi dp_x \frac{u}{2} \frac{\partial}{\partial u} \int_0^\pi dp_y \log[1 - 2u \cos p_y + u^2], \end{aligned} \quad (27)$$

where  $u = 2z \cos p_x$ . The integral over  $p_y$  is tabulated and given by [2],

$$\int_0^\pi dp_y \log[1 - 2u \cos p_y + u^2] = 2\pi[1 - D(u)] \log u, \quad (28)$$

where,

$$D(u) = \begin{cases} 1 & |u| < 1 \\ 0 & |u| > 1 \end{cases}. \quad (29)$$

As a result one finds,

$$n_{\text{string}} = \begin{cases} \frac{2}{\pi} \arccos \left[ \frac{1}{2z} \right] & z > \frac{1}{2} \\ 0 & z < \frac{1}{2} \end{cases}, \quad (30)$$

and this is plotted in Fig. 8. It can be seen that for  $T \rightarrow \infty$  ( $z \rightarrow 1$ ) the string density saturates at  $n_{\text{string}} = 2/3$ , while for  $T \approx T_K$  it shows Pokrovsky-Talapov critical behaviour with  $n_{\text{string}} \propto (T - T_K)^\beta$  and  $\beta = 1/2$ .

#### 4.1.4 Correlations

In order to better understand the correlations it is useful to study the spin-spin structure factor. In real space this is given by,

$$S(\mathbf{r}) = \langle \sigma_i \sigma_j \rangle, \quad (31)$$

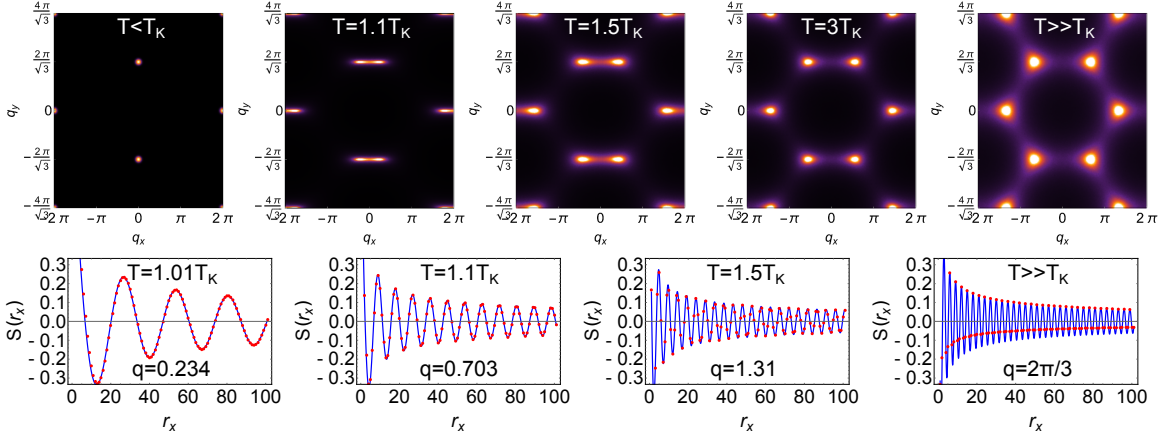


Figure 9: The structure factor of  $\mathcal{H}_{\text{ABB}}$  [Eq. 10]. (Top) The reciprocal-space structure factor  $S(\mathbf{q})$  [Eq. 32] at various temperatures, calculated by Monte Carlo simulation for a hexagonal cluster with  $L = 72$ . For  $T < T_K$  there are Bragg peaks at  $\mathbf{q}_{\text{stripe}} = (0, 2\pi/\sqrt{3})$ , and these have been artificially broadened for clarity. For  $T > T_K$  there are divergencies at the wavevectors  $\mathbf{q}_{\text{string}}(T) = (\pm\pi n_{\text{string}}, 2\pi/\sqrt{3})$  that go as  $S(\mathbf{q}_{\text{string}} + \delta\mathbf{q}) \propto |\delta\mathbf{q}|^{-3/2}$ . For  $T \gg T_K$  the physics of the isotropic TLIAF is recovered, with  $n_{\text{string}} = 2/3$  and  $\mathbf{q}_{\text{string}}(T) = (\pm 2\pi/3, 2\pi/\sqrt{3})$ . (Bottom) The real-space structure factor,  $S(r_x)$  [Eq. 31], in the direction perpendicular to the strings (i.e. parallel to A bonds), calculated in the thermodynamic limit using the Grassmann path integral approach (see Appendix B). Red dots show calculations and the blue line shows the best fit to  $S(r_x) = A \cos(\pi n_{\text{string}} r_x) / \sqrt{r_x}$ , where  $A$  is the only free parameter.

where  $\mathbf{r} = \mathbf{r}_i - \mathbf{r}_j$ , and in reciprocal space by,

$$S(\mathbf{q}) = \frac{1}{N} \sum_{\mathbf{r}} e^{i\mathbf{q}\cdot\mathbf{r}} S(\mathbf{r}), \quad (32)$$

where  $\mathbf{q}$  is in the Brillouin zone of the triangular lattice (care should be taken when relating this to the wavevector  $\mathbf{k}$  associated with the Brillouin zone of the brick lattice).

The structure factor can be calculated in the thermodynamic limit using the Grassmann path integral approach, following the general method proposed in [45].

For  $\delta J = 0$  this reproduces the results of [4, 5]. A detailed summary of the calculation is given in Appendix B, both for pairs of spins separated by an arbitrary number of A bonds (i.e. in the direction perpendicular to the strings, denoted  $r_x$ ) and for separations orthogonal to A bonds (i.e. in the direction parallel to the strings, denoted  $r_y$ ). In both cases the structure factor can be written as the determinant of a Toeplitz matrix, whose dimension is proportional to the separation between the spins. Exact expressions can be written for the matrix elements, but we find it necessary to calculate the determinant numerically.

In the case of isotropic interactions it has been argued that in the long distance limit the structure factor takes the form [4, 5],

$$S(\mathbf{r}) \propto \frac{\cos \mathbf{q} \cdot \mathbf{r}}{\sqrt{|\mathbf{r}|}}, \quad (33)$$

where  $\mathbf{q} = (\pm 2\pi/3, 2\pi/\sqrt{3})$ , and this is consistent with our calculations (see Fig. 9). The algebraic decay of correlations shows that the  $T = 0$  nearest-neighbour TLIAF is critical, and is on the verge of forming 3-sublattice order. The combination of long-range disorder and local correlation means that the system forms a classical spin liquid.



For  $\delta J \neq 0$  and  $T > T_K$  the structure factor retains the long-distance functional form given in Eq. 33, but the wavevector becomes temperature dependent and is given by  $\mathbf{q} = \pm \mathbf{q}_{\text{string}}(T) = (\pm \pi n_{\text{string}}(T), 2\pi/\sqrt{3})$ . This is clearly physically sensible, since the strings separate regions in which Ising spins have opposite sign, and the oscillation of the correlation function in the direction perpendicular to the strings should therefore have a period given by the average string separation. Some typical examples are shown in Fig. 9. Also shown is  $S(\mathbf{q})$ , which has pairs of algebraically diverging peaks at  $\mathbf{q} = \pm \mathbf{q}_{\text{string}}(T)$ . In the vicinity of these peaks  $S(\mathbf{q}_{\text{string}} + \delta \mathbf{q}) \propto |\delta \mathbf{q}|^{-3/2}$  in agreement with the algebraic decay of  $S(\mathbf{r})$  [Eq. 33]. It can be seen that the critical nature of the correlations is not broken by a non-zero  $\delta J$  as long as  $T > T_K$ , and this is due to the constraint forbidding defect triangles. In Section 4.2 this constraint will be relaxed, and the correlations will become exponentially decaying at finite  $T$ .

Having stated that the structure factor has the functional form given in Eq. 33 in the long distance limit, it is useful to be more precise over what counts as long distance. This has been considered in the closely related field of adsorption of a gas onto a substrate, where there exist domain walls with similar properties to the strings of the TLIAF [46]. A correlation length can be defined *beyond which* the long-distance algebraic correlation function given in Eq. 33 applies. In the direction perpendicular to the strings it is intuitively obvious that this is given by the average string-string separation, and therefore  $\zeta_{\perp} \sim 1/n_{\text{string}}$ . In the direction parallel to the strings it can be argued that  $\zeta_{\parallel} \sim 1/n_{\text{string}}^2$  [46]. In the case of  $\delta J = 0$  (or  $T \gg \delta J$ ), where  $n_{\text{string}} = 2/3$ , the correlation lengths,  $\zeta_{\perp}$  and  $\zeta_{\parallel}$ , are not much longer than a single lattice spacing, and the long distance asymptotic form of the structure factor is recovered for spins separated by only a few lattice spacings. On the other hand, for  $\delta J \neq 0$  and  $T \approx T_K$  the string density is low, and the correlation lengths become very large, especially in the direction parallel to the strings. For  $T \rightarrow T_K$  an expansion of  $n_{\text{string}}$  [Eq. 30] shows that the correlation lengths diverge as  $\zeta_{\perp} \sim (T - T_K)^{-\nu_{\perp}}$  and  $\zeta_{\parallel} \sim (T - T_K)^{-\nu_{\parallel}}$ , with  $\nu_{\perp} = 1/2$  and  $\nu_{\parallel} = 1$ .

For  $T < T_K$  the spin structure factor clearly does not follow the functional form of Eq. 33. Instead it is constant in real space, since the stripe state admits no fluctuations, and has Bragg peaks in reciprocal space. On cooling through  $T = T_K$  the pair of algebraically-diverging peaks in  $S(\mathbf{q})$  coalesce to form a single Bragg peak at  $\mathbf{q} = \mathbf{q}_{\text{stripe}} = (0, 2\pi/\sqrt{3})$  (see Fig. 9).

#### 4.1.5 Mapping to 1D quantum model

A slightly different perspective on the nearest-neighbour TLIAF is achieved by making a mapping onto a 1D quantum model of spinless fermions. The idea is that the strings can be viewed as the worldlines of spinless fermions, and the spatial direction parallel to the strings interpreted as imaginary time. The non-crossing constraint of the strings corresponds to the Pauli exclusion principle, and periodic boundary conditions in the 2D classical model enforce periodicity in imaginary time in the 1D quantum model. This type of mapping has been frequently used for related 2D classical models with non-crossing domain walls [41, 42, 47, 48, 49, 50].

We show in Appendix C that  $\mathcal{H}_{\text{ABB}}$  [Eq. 10] maps exactly onto the 1D quantum model,

$$\mathcal{H}_{\text{1D}} = \sum_i \left[ -\mu c_i^{\dagger} c_i + t \left( c_i^{\dagger} c_{i+1} + c_{i+1}^{\dagger} c_i \right) \right], \quad (34)$$

where,

$$t = z^2, \quad \mu = 2z^2 - 1. \quad (35)$$

The mapping demonstrates that the Grassmann variables,  $a_i$  and  $b_i$ , describe coherent states of fermions/strings (for details see Appendix C).

$\mathcal{H}_{1D}$  [Eq. 34] is simply diagonalised by Fourier transform, giving,

$$\mathcal{H}_{1D} = \sum_k \omega_k c_k^\dagger c_k, \quad \omega_k = 2t \cos k - \mu, \quad (36)$$

and the phase diagram of the fermion model can be matched to that of the nearest-neighbour TLIAF. For  $\mu/2t < -1$  there are no fermions in the system and this is analagous to the stripe phase in which there are no strings. At  $\mu/2t = -1$  there is a phase transition due to the minima of the fermion band touching zero, and for  $\mu/2t > -1$  the fermion density,  $n_f$ , is given by,

$$n_f = 1 - \frac{1}{\pi} \arccos \frac{\mu}{2t}, \quad (37)$$

which can be seen to be exactly equal to  $n_{\text{string}}$  [Eq. 30]. According to the mapping given in Eq. 35,  $\mu$  and  $t$  are not independent parameters, and the maximum value of their ratio is given by  $\mu/2t = 1/2$ . This corresponds to  $z = 1$  (equivalently  $T \rightarrow \infty$ ) and at this point  $n_f = n_{\text{string}} = 2/3$  as expected. Other physical quantities, such as the heat capacity or the spin-spin structure factor can be calculated within the 1D fermion picture, and in some cases this simplifies the procedure.

It should be noted that if the 2D classical model has periodic boundary conditions, then the number of strings in the system is constrained to be even. The 1D quantum model is therefore restricted to the even-parity fermion subsector. If the 2D model is instead defined on a cylinder with the periodic direction parallel to the strings, then this restriction is lifted.

One of the utilities of the 2D classical to 1D quantum mapping is that for more complicated 2D models with longer range interactions it provides a good starting point for phenomenological theories.

## 4.2 $J_{1A}$ - $J_{1B}$ model with an unconstrained manifold

We next consider a TLIAF with Hamiltonian  $\mathcal{H}_{ABB}$  [Eq. 10], but, unlike in Section 4.2, the manifold of Ising configurations is unconstrained and defect triangles are therefore allowed.

### 4.2.1 Dimer mapping

$\mathcal{H}_{ABB}$  [Eq. 10] with an unconstrained manifold can be mapped onto a dimer model on the honeycomb lattice, but there is no longer a hardcore constraint, since vertices at the centre of defect triangles are covered by 3 dimers. Since the Grassmann path integral approach to determining the partition function requires the dimers to obey a hardcore constraint, it is necessary to instead consider the mapping onto a dimer model on the extended honeycomb lattice (described in Section 2.1 and Fig. 2). This type of mapping was suggested in a more general context in [30], and makes possible an exact evaluation of the partition function.

The dimers can be categorised as those covering A, B or C bonds of the original triangular lattice (see Fig. 1 for bond labelling) or “extra” dimers, covering the bonds introduced in the act of extending the honeycomb lattice. The total number of dimers is fixed and given by,

$$N_{\text{dim}}^A + N_{\text{dim}}^B + N_{\text{dim}}^C + N_{\text{dim}}^{\text{ext}} = N_{\text{bond}}, \quad (38)$$

where  $N_{\text{bond}} = 3N$  refers to the number of bonds of the original triangular lattice and  $N_{\text{dim}}^{\text{ext}}$  is the number of dimers on “extra” bonds. The energy of a given configuration relative to that of the ground state can be written as,

$$\Delta E_{\text{ABB}} = \frac{4}{3} J_{1A} N_{\text{bond}} + 2\delta J (N_{\text{dim}}^{\text{B}} + N_{\text{dim}}^{\text{C}}) - 2J_{1A} N_{\text{dim}}^{\text{ext}}, \quad (39)$$

and therefore,

$$\mathcal{Z}_{\text{ABB}} \propto \mathcal{Z}_{\text{exhon}} = z_{\text{A}}^{2N} \sum_{\text{dimer cov}} z^{\text{N}_{\text{dim}}^{\text{B}} + \text{N}_{\text{dim}}^{\text{C}}} z_{\text{A}}^{-\text{N}_{\text{dim}}^{\text{ext}}}, \quad (40)$$

where the sum is over all dimer coverings of the extended honeycomb lattice,

$$z_{\text{A}} = e^{-\frac{2J_{1A}}{T}}, \quad z_{\text{B}} = e^{-\frac{2J_{1B}}{T}}, \quad z = \frac{z_{\text{B}}}{z_{\text{A}}}, \quad (41)$$

and the factor  $z_{\text{A}}^{2N}$  ensures that  $\mathcal{Z}_{\text{exhon}}$  is equal to  $\mathcal{Z}_{\text{hon}}$  [Eq. 14] in the limit where  $z_{\text{A}} \rightarrow 0$  and  $z_{\text{B}} \rightarrow 0$  with  $z$  finite (i.e. the condition for being in the constrained manifold of Ising configurations).

#### 4.2.2 Evaluation of the partition function

The evaluation of the partition function proceeds as in Section 4.1, with the main difference being that there are 6 rather than 2 lattice sites in the unit cell.

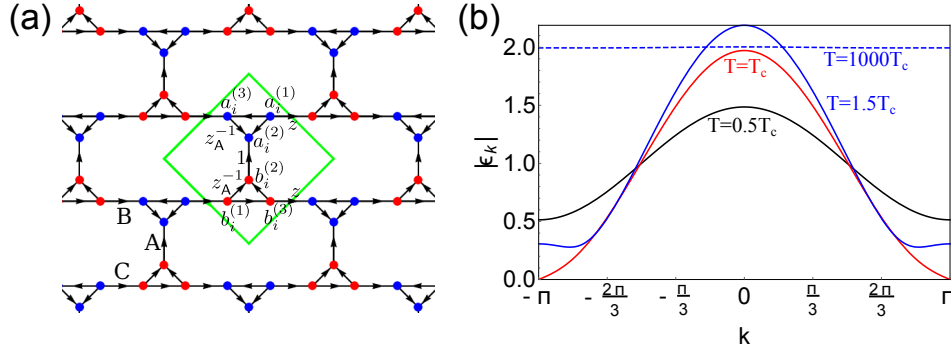


Figure 10: The extended brick lattice and spectrum  $|\epsilon_{\mathbf{k}}|$  [Eq. 46] used to calculate the partition function of  $\mathcal{H}_{\text{ABB}}$  [Eq. 10] in the unconstrained manifold. (a) Bond directions (black arrows) are chosen so as to respect Kasteleyn’s theorem [29], and bond weights are chosen to be  $z$  on B and C bonds, 1 on A bonds and  $z_{\text{A}}^{-1}$  on “extra” bonds, in accordance with  $\mathcal{Z}_{\text{exhon}}$  [Eq. 40]. The  $i$ th unit cell (green) contains 6 sites with associated Grassmann variables  $a_i^{(1)}$ ,  $a_i^{(2)}$  and  $a_i^{(3)}$  (blue) and  $b_i^{(1)}$ ,  $b_i^{(2)}$  and  $b_i^{(3)}$  (red). The translation vectors of the unit cell are  $\hat{e}_x$  and  $\hat{e}_y$  (see Fig. 7), and these are taken to be unit length. (b) The spectrum  $|\epsilon_{\mathbf{k}}|$  [Eq. 46] along the path  $\mathbf{k} = (k, k + \pi)$  for  $J_{1A} = 1$  and  $J_{1B} = 1.5$ . For  $T < T_c$  (black) the spectrum is gapped at all  $\mathbf{k}$ , and this corresponds to the stripe-ordered phase. At  $T = T_c$  (red) the gap closes at  $\mathbf{k} = (\pi, 0)$  and an Ising transition occurs. For  $T > T_c$  (blue) the gap reopens. For  $T_c < T < T_{\text{is}}$  the minimum of  $|\epsilon_{\mathbf{k}}|$  is at  $\mathbf{k} = (\pi, 0)$ . For  $T > T_{\text{is}}$  the minimum migrates away from  $\mathbf{k} = (\pi, 0)$ . In the limit  $T \rightarrow \infty$  the spectrum becomes flat.

Each site of the extended honeycomb lattice is assigned a real Grassmann variable, as shown in Fig. 10, and these are labelled  $a_i^l$  and  $b_i^l$  where  $i$  labels the unit cell, and  $l \in \{1, 2, 3\}$  labels sites within the unit cell. Bond weights are  $z$  on B and C bonds, 1 on A bonds and  $z_{\text{A}}^{-1}$  on “extra” bonds, in accordance with  $\mathcal{Z}_{\text{exhon}}$  [Eq. 40]. The partition function is given by,

$$\mathcal{Z}_{\text{exhon}} = z_{\text{A}}^{2N} \int \prod_{i,l} da_i^{(l)} db_i^{(l)} e^{\mathcal{S}_2}, \quad (42)$$

where,

$$\begin{aligned} \mathcal{S}_2 = \sum_i & \left[ b_i^{(2)} a_i^{(2)} + z \left( b_i^{(3)} a_{i+\hat{e}_x}^{(3)} + a_i^{(1)} b_{i+\hat{e}_y}^{(1)} \right) \right. \\ & \left. + z_{\mathbf{A}}^{-1} \left( b_i^{(1)} b_i^{(3)} + b_i^{(1)} b_i^{(2)} + b_i^{(3)} b_i^{(2)} + a_i^{(1)} a_i^{(3)} + a_i^{(1)} a_i^{(2)} + a_i^{(3)} a_i^{(2)} \right) \right]. \end{aligned} \quad (43)$$

This can be diagonalised by taking the Fourier Transform of the Grassmann variables (see Eq. 18), resulting in,

$$\begin{aligned} \mathcal{S}_2 = \sum_{\mathbf{k}} & \left[ b_{-\mathbf{k}}^{(2)} a_{\mathbf{k}}^{(2)} e^{-i\frac{k_x - k_y}{4}} + z \left( b_{-\mathbf{k}}^{(3)} a_{\mathbf{k}}^{(3)} + a_{-\mathbf{k}}^{(1)} b_{\mathbf{k}}^{(1)} \right) e^{i\frac{k_x + k_y}{4}} \right. \\ & \left. + z_{\mathbf{A}}^{-1} \left( b_{-\mathbf{k}}^{(1)} b_{\mathbf{k}}^{(3)} e^{i\frac{k_x + k_y}{4}} + b_{-\mathbf{k}}^{(1)} b_{\mathbf{k}}^{(2)} e^{i\frac{k_y}{4}} + b_{-\mathbf{k}}^{(3)} b_{\mathbf{k}}^{(2)} e^{-i\frac{k_x}{4}} + a_{\mathbf{k}}^{(1)} a_{-\mathbf{k}}^{(3)} e^{i\frac{k_x + k_y}{4}} + a_{\mathbf{k}}^{(1)} a_{-\mathbf{k}}^{(2)} e^{i\frac{k_y}{4}} + a_{\mathbf{k}}^{(3)} a_{-\mathbf{k}}^{(2)} e^{-i\frac{k_x}{4}} \right) \right]. \end{aligned} \quad (44)$$

After rewriting the action as a matrix equation, taking the Pfaffian of the matrix and absorbing the  $z_{\mathbf{A}}^{2N}$  factor, one can show that,

$$\mathcal{Z}_{\text{exhon}} = \prod_{\mathbf{k}} |\epsilon_{\mathbf{k}}|, \quad (45)$$

where,

$$\begin{aligned} |\epsilon_{\mathbf{k}}| = & \left\{ 1 + 2z(\cos k_x - \cos k_y) + 2z^2(1 - \cos[k_x + k_y]) \right. \\ & \left. + 2z_{\mathbf{B}}^2 \cos[k_x + k_y] - 2z_{\mathbf{B}}^2 z(\cos k_x - \cos k_y) + z_{\mathbf{B}}^4 \right\}^{\frac{1}{2}}. \end{aligned} \quad (46)$$

It can be seen that this reduces to the  $|\epsilon_{\mathbf{k}}|$  of the constrained manifold [Eq. 22] when the limit  $z_{\mathbf{A}} \rightarrow 0$  and  $z_{\mathbf{B}} \rightarrow 0$  is taken such that  $z$  remains finite (equivalently  $J_{1\mathbf{A}} \rightarrow \infty$  and  $J_{1\mathbf{B}} \rightarrow \infty$  while  $\delta J$  remains finite). It can also easily be checked that in the  $T \rightarrow \infty$  limit the entropy per site is  $S/N = \log 2$  as expected.

### 4.2.3 Physical properties

The spectrum  $|\epsilon_{\mathbf{k}}|$  [Eq. 46], which is shown in Fig. 10, determines the physical properties of  $\mathcal{H}_{\text{ABB}}$  [Eq. 10]. As in the case of the constrained manifold there is a phase transition between an ordered and disordered phase. However, we label the transition temperature  $T_c$  rather than  $T_K$ , since it is not technically a Kasteleyn transition, as will be explained below.

For  $T < T_c$  the spectrum is gapped at all  $\mathbf{k}$ , and this corresponds to the stripe-ordered phase. The main difference from the case of the constrained manifold is that local fluctuations involving the creation of pairs of defect triangles are possible, though, depending on the value of  $T_c$ , they can be highly suppressed.

There is a phase transition at  $T = T_c$  associated with the closing of the gap in  $|\epsilon_{\mathbf{k}}|$ , and this occurs at  $\mathbf{k} = (\pi, 0)$ . It can be seen from Eq. 46 that this requires,

$$1 - 2z(T_c) - z_{\mathbf{B}}(T_c)^2 = 0, \quad (47)$$

and the solution of this equation gives the critical temperature.

For  $T > T_c$  a gap reopens in  $|\epsilon_{\mathbf{k}}|$ , and this signifies that correlations are exponential in the paramagnetic state [46].

In order to investigate the nature of the phase transition, it is natural to define a second temperature,  $T_{\text{Is}}$ , such that in the temperature range  $T_c < T < T_{\text{Is}}$  the minimum of  $|\epsilon_{\mathbf{k}}|$  is at  $\mathbf{k} = (\pi, 0)$ , while for  $T > T_{\text{Is}}$  the minimum of  $|\epsilon_{\mathbf{k}}|$  is at a temperature-dependent incommensurate wavevector.  $T_{\text{Is}}$  can be determined from the equation,

$$(1 - 2z)^2 + 4\frac{z_{\text{B}}^2}{z} - 10z_{\text{B}}^2 + 4z_{\text{B}}^2z + 4\frac{z_{\text{B}}^4}{z^2} - 4\frac{z_{\text{B}}^4}{z} + z_{\text{B}}^4 \Big|_{T \rightarrow T_{\text{Is}}} = 0, \quad (48)$$

and it can be seen from Eq. 46 that for  $T_c < T < T_{\text{Is}}$  the gap is given by,

$$\min |\epsilon_{\mathbf{k}}| = |1 - 2z - z_{\text{B}}^2|. \quad (49)$$

After setting  $T = T_c + \delta T$ , with  $\delta T \ll T_c$  and  $\delta T < T_{\text{Is}} - T_c$ , one can show that the gap goes as  $\min |\epsilon_{\mathbf{k}}| \propto \delta T$ . Taking the correlation length to be inversely proportional to the gap,  $\xi \propto 1/\min |\epsilon_{\mathbf{k}}|$ , results in  $\xi \propto \delta T^{-\nu}$  with  $\nu = 1$ , and this is typical of a 2D Ising transition [49]. Therefore Ising critical exponents are realised in the temperature window  $T_c < T < T_{\text{Is}}$ . However, the caveat to this is that the Ising temperature window can be exponentially small, and this is the case for  $\delta J \ll J_{1A}$  where,

$$T_{\text{Is}} - T_c \propto e^{-\frac{J_{1A}}{\delta J}}. \quad (50)$$

For  $T > T_{\text{Is}}$  the minimum of  $|\epsilon_{\mathbf{k}}|$  moves away from  $\mathbf{k} = (\pi, 0)$  and the critical behaviour crosses over to that of the Pokrovsky-Talapov universality class. Thus in the situation where  $\delta J \ll J_{1A}$  the transition is technically an Ising transition, but all practical measurements, whether in experiment or simulation, will show the features of a Kasteleyn transition. The values of  $T_c$  and  $T_{\text{Is}}$  are shown as a function of  $\delta J/J_{1A}$  in Fig. 12, and it can be seen that the Ising temperature window only starts to be significant for  $\delta J/J_{1A} \gtrsim 0.3$ .

Further increases in  $T$  increase the size of the gap and in the limit  $T \rightarrow \infty$  the spectrum,  $|\epsilon_{\mathbf{k}}|$ , becomes completely flat, corresponding to an uncorrelated paramagnet where all configurations are equally likely.

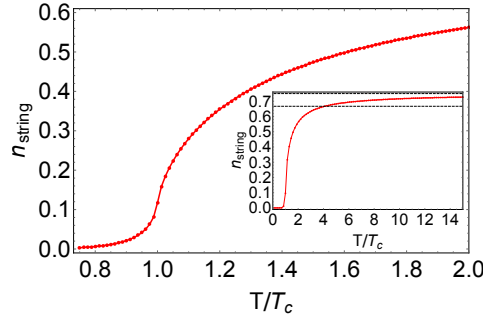


Figure 11: The density of strings,  $n_{\text{string}}$  [Eq. 25] calculated from  $|\epsilon_{\mathbf{k}}|$  [Eq. 46] in the unconstrained manifold. The parameters used are  $J_{1A} = 1$  and  $J_{1B} = 1.5$ . In the low-temperature, stripe-ordered phase ( $T < T_c$ ) the string density is low but non-zero, before rapidly increasing at  $T = T_c$ . (Inset) At higher temperatures it passes through  $n_{\text{string}} = 2/3$  (the value realised in the constrained manifold) before saturating at  $n_{\text{string}} = 3/4$ .

The density of strings,  $n_{\text{string}}$ , can be calculated using Eq. 25 and the result is shown in Fig. 11. In the stripe-ordered phase  $n_{\text{string}}$  is low, but not fixed to zero, as it is possible to create bound pairs of defect triangles, connected by a pair of strings. Its value increases rapidly at  $T = T_c$ , since the defect triangles unbind, and therefore strings can wind the system.

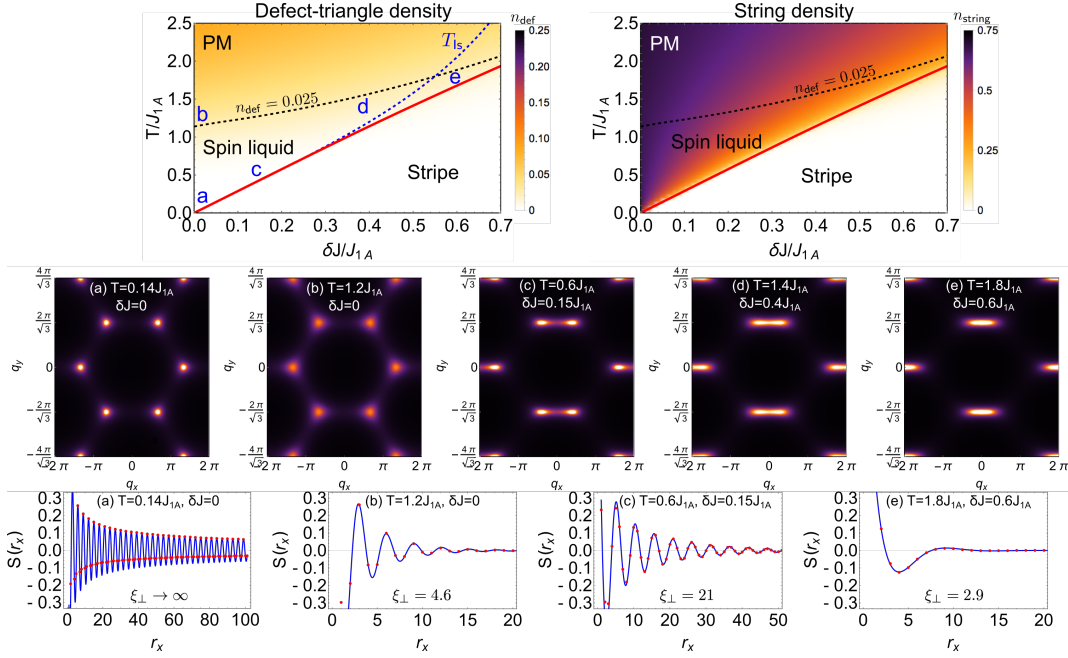


Figure 12: The phase diagram and structure factor of  $\mathcal{H}_{ABB}$  [Eq. 10] in the unconstrained manifold. (Top) Phase diagram showing stripe-ordered, spin-liquid and paramagnetic (PM) regions, with lines showing the critical temperature  $T_c$  [Eq. 47, red] as well as  $T_{1s}$  [Eq. 88, blue dashed]. Colour overlays show the density of defect triangles,  $n_{def}$ , and string density,  $n_{string}$ , calculated from the Grassmann path integral approach. (Middle) The structure factor  $S(\mathbf{q})$  [Eq. 32] calculated on an  $L = 72$  hexagonal cluster using Monte Carlo simulation. (Bottom) The real space structure factor  $S(r_x)$  [Eq. 31] in the direction perpendicular to the strings (i.e. parallel to A bonds), calculated in the thermodynamic limit using the Grassmann path integral approach. The blue line shows a fit to the long-distance asymptotic form given in Eq. 51, with the fitting parameters  $\xi_{\perp}$ ,  $q_x$  and a multiplicative prefactor. (a) At  $\delta J = 0$  and  $T \ll J_{1A}$  the structure factor is indistinguishable from  $T = 0$ , with sharp essentially algebraic peaks at  $\mathbf{q} = (\pm 2\pi/3, 2\pi/\sqrt{3})$  and a correlation length  $\xi_{\perp} \rightarrow \infty$ . (b) At  $\delta J = 0$  and  $T \sim J_{1A}$  the peaks remain at  $\mathbf{q} = (\pm 2\pi/3, 2\pi/\sqrt{3})$  but broaden and the correlation length is only a few times larger than the lattice spacing. (c) For  $\delta J \ll J_{1A}$  and for temperatures deep in the spin-liquid regime there are a pair of peaks whose positions approximately track the string density according to  $\mathbf{q}_{string}(T) = (\pm \pi n_{string}, 2\pi/\sqrt{3})$ . The correlation length is typically many times the lattice spacing. (d) At  $\delta J \ll J_{1A} = 0.4$  the spin-liquid region is narrow, but weight at  $\mathbf{q}_{string}(T)$  remains more significant than that at  $\mathbf{q}_{stripe} = (0, 2\pi/\sqrt{3})$ . (e) At  $\delta J \ll J_{1A} = 0.6$  the spin-liquid regime has disappeared and above the transition the structure factor is dominated by correlations at the ordering vector,  $\mathbf{q}_{stripe} = (0, 2\pi/\sqrt{3})$ .

On further increasing  $T$  the density of strings passes through  $n_{string} = 2/3$  (the value realised in the constrained manifold) before saturating at  $n_{string} = 3/4$ .

Since  $n_{string}$  is not zero in the stripe phase, it is not, strictly speaking, an order parameter. However, it remains a useful indicator of where the transition occurs as well as providing a way of characterising the disordered phase.

#### 4.2.4 Phase diagram and correlations

The phase diagram for  $\mathcal{H}_{ABB}$  [Eq. 10] in the unconstrained manifold can be calculated exactly, and is shown in Fig. 12. The nature of the correlations can be explored via the spin structure factor [Eq. 31], and this is shown in the same figure for a representative set of parameters.

The phase diagram shows three regions, a stripe-ordered phase, a strongly-correlated spin-liquid region and a weakly correlated paramagnet. The stripe-ordered phase is separated from

the disordered region by a phase transition at  $T_c$  [Eq. 47], while we take the crossover between the spin-liquid and paramagnetic regions to occur when the density of defect triangles,  $n_{\text{def}}$  reaches 10% of its saturation value (i.e.  $n_{\text{def}} = 0.025$ ). As  $\delta J$  is increased, the transition temperature  $T_c$  increases faster than the crossover temperature, and therefore the spin-liquid region shrinks.

The nature of the correlations in the disordered phase changes significantly with varying  $T$  and  $\delta J$ , and this can be seen from studying the structure factor [Eq. 31].  $S(\mathbf{r})$  can be calculated in the thermodynamic limit via the Grassmann path integral approach (see Appendix B), and some examples are shown in Fig. 12. Also shown is  $S(\mathbf{q})$ , which for simplicity is calculated using Monte Carlo simulation.

We make the ansatz that in the disordered regions  $S(\mathbf{r})$  takes the long-distance asymptotic form [5],

$$S(\mathbf{r}) \propto \frac{\cos \mathbf{q} \cdot \mathbf{r} e^{-\frac{rx}{\xi_{\perp}}} e^{-\frac{ry}{\xi_{\parallel}}}}{\sqrt{|\mathbf{r}|}}, \quad (51)$$

where in the case of  $\delta J \neq 0$  the correlation length perpendicular to the strings,  $\xi_{\perp}$ , can be different from that parallel to the strings,  $\xi_{\parallel}$ . This is found to give good fits to the calculated values of  $S(\mathbf{r})$  after taking into account the definition of long distance given in Section 4.1.4.

In the spin-liquid region the correlation length is considerably larger than the lattice spacing, and the system approximately realises the algebraically decaying correlation function studied in Section 4.1.4 for the constrained manifold. In particular for  $\delta J = 0$  and  $T \ll J_{1A}$  then to all practical purposes  $\xi_{\perp} = \xi_{\parallel} \rightarrow \infty$ . At the crossover to the paramagnetic region, which we have somewhat arbitrarily defined as the temperature at which the defect triangle density,  $n_{\text{def}}$ , is 10% of its saturation value, the correlation length is approximately  $\xi_{\perp} \sim 5$ , with  $\xi_{\parallel} \geq \xi_{\perp}$ . Since the density of defect triangles is by definition low within the spin-liquid region, most of the strings wind the system, and therefore the relationship  $\mathbf{q} \approx \pm \mathbf{q}_{\text{string}}(T) = (\pm \pi n_{\text{string}}(T), 2\pi/\sqrt{3})$  holds to a good approximation.

In the paramagnetic region the correlation lengths become comparable with the lattice spacing, and the structure factor has a very different form to the algebraic decay found for the constrained manifold. In this region the strings mostly form short closed loops, and therefore the relationship between  $\mathbf{q}$  and  $n_{\text{string}}$  breaks down. For  $\delta J \gtrsim 0.5$  there is a direct transition from the stripe-ordered phase to the paramagnet. In the Ising critical region close to the transition the correlation function shows the usual 2D Ising scaling and is peaked in reciprocal space at  $\mathbf{q}_{\text{stripe}}$ .

In the stripe-ordered phase the asymptotic form of  $S(\mathbf{r})$  given in Eq. 51 is no longer relevant, and Bragg peaks form in  $S(\mathbf{q})$  at the ordering vector  $\mathbf{q}_{\text{stripe}} = (0, 2\pi/\sqrt{3})$ . Fluctuations around the ground state are not strictly forbidden, but are rare unless  $T \sim J_{1A}$ , which is only possible for large anisotropies.

#### 4.2.5 Mapping to 1D quantum model

$\mathcal{H}_{\text{ABB}}$  [Eq. 10] in the unconstrained manifold can be exactly mapped onto a 1D quantum model of spinless fermions, as was found to be the case for the constrained manifold in Section 4.1.5. The main difference is that in the unconstrained manifold defect triangles act as sources and sinks of pairs of strings. In consequence, pair creation and annihilation terms appear in the 1D quantum model.



Following a similar logic to that of Appendix C, there is an exact mapping of  $\mathcal{H}_{\text{ABB}}$  [Eq. 10] onto,

$$\mathcal{H}_{\text{1D}} = \sum_i \left[ -\mu c_i^\dagger c_i + t \left( c_i^\dagger c_{i+1} + c_{i+1}^\dagger c_i \right) + \Delta \left( c_i^\dagger c_{i+1}^\dagger + c_{i+1} c_i \right) \right], \quad (52)$$

where,

$$t = z^2 + z_{\text{B}}^2, \quad \mu = 2z^2 - (1 + z_{\text{B}}^4), \quad \Delta = 2z_{\text{B}}z, \quad (53)$$

and the evolution of these parameters with the temperature of the classical model is shown in Fig. 13.

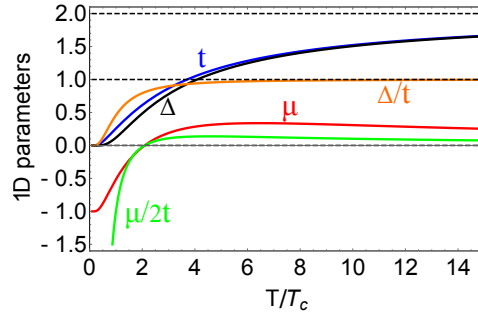


Figure 13: Mapping between the 2D classical model  $\mathcal{H}_{\text{ABB}}$  [Eq. 10] and the 1D quantum model  $\mathcal{H}_{\text{1D}}$  [Eq. 52]. The parameters of the 1D quantum model depend on those of the classical model according to Eq. 53, and the relationship is shown for  $J_{\text{1B}}/J_{\text{1A}} = 1.5$ . As  $T \rightarrow 0$  then  $t \rightarrow 0$ ,  $\mu \rightarrow -1$ ,  $\Delta \rightarrow 0$ ,  $\mu/2t \rightarrow -\infty$  and  $\Delta/t \rightarrow 0$ . The phase transition occurs when  $\mu/2t = -1$ . In the limit  $T \rightarrow \infty$  then  $t \rightarrow 2$ ,  $\mu' \rightarrow 0$ ,  $\Delta \rightarrow 2$ ,  $\mu/2t \rightarrow 0$  and  $\Delta/t \rightarrow 1$ .

$\mathcal{H}_{\text{1D}}$  [Eq. 52] can be diagonalised by Fourier and Bogoliubov transformations, resulting in,

$$\mathcal{H}_{\text{1D}} = \sum_k \omega_k a_k^\dagger a_k + \frac{1}{2} \sum_k (A_k - \omega_k), \quad (54)$$

where,

$$A_k = 2t \cos k - \mu, \quad B_k = 2\Delta \sin k, \quad \omega_k = \sqrt{A_k^2 + B_k^2}, \quad (55)$$

and,

$$\begin{pmatrix} a_k \\ a_{-k}^\dagger \end{pmatrix} = \begin{pmatrix} u_k & -iv_k \\ -iv_k & u_k \end{pmatrix} \begin{pmatrix} c_k \\ c_{-k}^\dagger \end{pmatrix}. \quad (56)$$

The parameters of the Bogoliubov transformation are given by,

$$2u_k v_k = \frac{B_k}{\omega_k}, \quad u_k^2 - v_k^2 = \frac{A_k}{\omega_k}, \quad u_k^2 + v_k^2 = 1. \quad (57)$$

Physical properties of the classical TLIAF can be calculated directly from the quantum model. For example the classical quantity  $n_{\text{string}}$  [Eq. 25] is equal to the fermion density [49].

It is interesting to note that  $\mathcal{H}_{\text{1D}}$  [Eq. 52] is the model studied in [51], where it was shown that there is a phase transition between a topologically trivial state, and a 2-fold degenerate

state with Majorana-fermion edge excitations. Here the topologically trivial state maps to the stripe-ordered phase, while the topologically non-trivial state maps to the disordered phase. For the Ising model the presence of periodic boundary conditions means that there is always an even number of strings in the system, and therefore the string parity is conserved. However, for open boundary conditions (i.e. on a cylinder) this even-parity condition no longer holds, and it would be interesting to explore the nature of the edge modes.

### 4.3 $J_{1A}$ - $J_{1B}$ - $J_2$ model with a constrained manifold

In order to get a better understanding of the role of further-neighbour interactions we next study the toy model,

$$\mathcal{H}_{\text{ABB2}} = J_{1A} \sum_{\langle ij \rangle_A} \sigma_i \sigma_j + J_{1B} \sum_{\langle ij \rangle_{B,C}} \sigma_i \sigma_j + J_2 \sum_{\langle ij \rangle_2} \sigma_i \sigma_j, \quad (58)$$

in the constrained manifold. An isotropic second-neighbour interaction has been added on top of the nearest-neighbour interacting model  $\mathcal{H}_{\text{ABB}}$  [Eq. 10]. The second-neighbour bonds are labelled  $\langle ij \rangle_2$  and we consider the case of  $J_2 > 0$ .  $\mathcal{H}_{\text{ABB2}}$  [Eq. 58] does not have a simple exact solution and we therefore study it using approximate techniques, including Monte Carlo simulations and perturbation theory.

#### 4.3.1 General considerations

Before turning to detailed calculations, it is worth considering some of the qualitative features of  $\mathcal{H}_{\text{ABB2}}$  [Eq. 58], both in terms of the nature of the phase transition and of the correlations in the spin-liquid phase (there is no paramagnetic region due being in the constrained manifold).

The second-neighbour interaction,  $J_2$ , and the nearest-neighbour anisotropy,  $\delta J$ , act in concert with one another, in the sense that they both favour a stripe-ordered ground state. However, they act in opposition in the sense that  $J_2$  favours a first-order phase transition, while  $\delta J$  favours a second-order transition.

This can be seen by comparing the  $\delta J = 0$  case to that with  $\delta J \gg J_2$ . At  $\delta J = 0$  the  $J_2$  interaction selects a 6-fold degenerate, stripe-ordered ground state from the manifold of constrained Ising configurations [10]. The  $J_1$ - $J_2$  TLIAF has been extensively studied, both analytically and by Monte Carlo simulation, and it is known that there is a first-order phase transition into the stripe phase [7, 8, 10, 9, 11]. In the limit of  $J_1 \rightarrow \infty$  the transition occurs at  $T_1 = 6.39J_2$  [11]. Therefore we expect that, in the region where  $J_2 \gg \delta J$ , the transition between the paramagnet and stripe-ordered state will be first order.

In contrast, the first-neighbour anisotropy,  $\delta J$ , favours a 2-fold degenerate stripe-ordered ground state, with stripes running parallel to A bonds (see Fig. 1 for the definition of bond directions). For  $\delta J \gg J_2$  the  $J_2$  interaction is irrelevant, and to a good approximation the analysis of Section 4.1 applies, indicating that the transition is second order. One focus here will be to study the crossover between the first and second-order phase transitions, which occurs when  $J_2$  and  $\delta J$  are comparable in magnitude.

When the transition is second order it is driven by the creation of isolated strings that wind the system (in [10] this is discussed in terms of the closely related concept of double domain walls). In order for a second-order transition to occur it is necessary that there is a repulsive interaction between these strings, and this repulsion is entropically driven and associated with the no-crossing constraint [41, 42]. We show below that further-neighbour interactions result

in an energetically-driven attraction between the strings, and that the second to first order crossover occurs when this balances the entropically-driven repulsion.

The free energy of an isolated string can be calculated exactly, and this can be used to find the exact transition temperature in the case of a second-order transition. Relative to the ground-state energy, strings cost an energy per unit length of  $E_{\text{string}} = 2\delta J + 4J_2$  and corners, at which the string changes direction, have an energy cost  $E_c = 2J_2$  [10, 11]. It follows that the free energy per unit length of an isolated string relative to the stripe ground state is given by [10],

$$f_{\text{string}}(T) = E_{\text{string}} - T \log \left[ 1 + e^{-\frac{E_c}{T}} \right]. \quad (59)$$

The second order transition temperature,  $T_K$ , can be calculated from solving the equation  $f_{\text{string}}(T_K) = 0$ , and in the case of  $J_2 = 0$  it can be seen that this reduces to Eq. 24.

The behaviour in the spin-liquid state should be closely related to the nature of the phase transition, since it is also sensitive to whether the interaction between strings is attractive or repulsive. In the introduction it was argued that the associated fermionic model can be weakly or strongly coupled, and it makes intuitive sense that weakly-coupled fermions correspond to repulsive string-string interactions, while strongly-coupled fermions correspond to attractive string-string interactions. In the weak-coupling case it can be expected that the spin liquid realises a 2D classical equivalent of a Luttinger liquid. In the strong coupling case it is less clear what to expect *a priori*. The crossover between weak and strong coupling is controlled by the ratio  $J_2/T$ , with weak coupling for  $T \gg J_2$ .

### 4.3.2 Diagrammatic perturbation theory

The first approximate method we use to better understand  $\mathcal{H}_{\text{ABB2}}$  [Eq. 58] in the constrained manifold is that of perturbation theory around the high-temperature limit. This approach cannot hope to compete with Monte Carlo simulations in terms of quantitative measures of, for example, the transition temperature, but does provide useful physical insights that are not apparent in Monte Carlo. While the approach is well motivated in the “weak-coupling” regime, we find that it also gives some clues as to how the system crosses over to the “strong-coupling” regime and to the appearance of a first-order phase transition.

The starting point of the perturbation expansion is the exact solution of  $\mathcal{H}_{\text{ABB}}$  [Eq. 10], which is summarised in Section 4.1. This captures the behaviour of  $\mathcal{H}_{\text{ABB2}}$  [Eq. 58] in the limit  $J_2/T \rightarrow 0$ . The perturbation expansion involves introducing the effect of the  $J_2$  interactions order by order in the small parameter  $|z_2 - 1|$ , where,

$$z_2 = e^{-\frac{2J_2}{T}}. \quad (60)$$

This can be done using a Grassmann path integral approach, following in spirit [52].

The first step is to map the Ising model,  $\mathcal{H}_{\text{ABB2}}$  [Eq. 58], onto a dimer model on the dual honeycomb lattice. For the nearest-neighbour interactions the mapping is the same as in Section 4.1. The second-neighbour coupling maps onto dimer-dimer interactions, where dimers on the same hexagon interact if they are separated by one unfilled bond (see Fig. 14). It follows that the partition function can be written as,

$$\mathcal{Z}_{\text{ABB2}} \propto \mathcal{Z}_{\text{hon2}} = \sum_{\text{dimer cov}} z^{N_{\text{dim}}^{\text{B}} + N_{\text{dim}}^{\text{C}}} z_2^{N_2}, \quad (61)$$

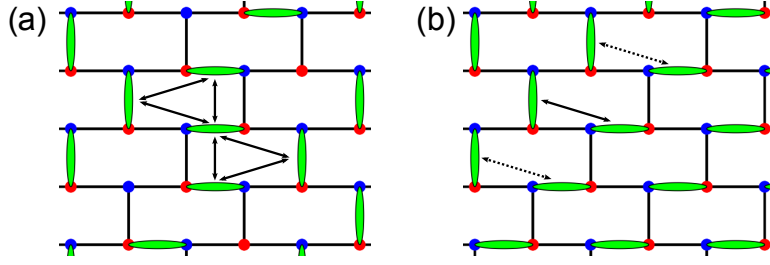


Figure 14: Dimer-dimer interactions on the brick (honeycomb) lattice. Dimers interact if they are on the same hexagonal plaquette and are separated by a single unfilled bond, and interactions are shown by black arrows. Each interaction carries a weight  $z_2$  in the partition function  $\mathcal{Z}_{\text{hon2}}$  [Eq. 61]. The system can be split into connected clusters of mutually interacting dimers, and these are only assigned the correct weight when the expansion of the action reaches that of the cluster size (see Eq. 62). (a) The largest connected cluster has 5 dimers, and it is therefore necessary to consider terms up to  $\mathcal{S}_{10}[a, b]$ . (b) The largest connected cluster has only 2 dimers, and the weight is correctly assigned by considering terms up to  $\mathcal{S}_4[a, b]$ .

where  $N_2$  is the number of dimer-dimer interactions (see Fig. 14).

The mapping of  $\mathcal{Z}_{\text{hon2}}$  [Eq. 61] onto a Grassmann path integral does not result in a purely quadratic action, and therefore it is not exactly solvable by this method. Instead the mapping results in an action including terms with  $2, 4, 6 \dots 2N$  Grassmann variables, and one can write,

$$\mathcal{Z}_{\text{hon2}} = \int \prod_i da_i db_i e^{\mathcal{S}_2[a, b] + \mathcal{S}_4[a, b] + \mathcal{S}_6[a, b] + \dots + \mathcal{S}_{2N}[a, b]}, \quad (62)$$

where the quadratic term  $\mathcal{S}_2[a, b]$  is given in Eq. 17 and contains products of 2 Grassmann variables, the quartic term,  $\mathcal{S}_4[a, b]$ , contains products of 4 Grassmann variables and similarly for higher order terms, with  $2N$  the number of honeycomb lattice sites.

For a particular dimer configuration, one can ask which terms in the expansion of the action are required to correctly assign the weight. The answer depends on the size of the largest cluster of dimers connected by pairwise interactions (see Fig. 14). If the largest cluster contains  $n$  dimers, then it is necessary to consider the terms  $\mathcal{S}_{2m}[a, b]$  with  $m \leq n$ . Since clusters that include a sizeable fraction of all the dimers are common, many dimer configurations require one to consider terms up to  $n \sim N$ .

For an infinite lattice it is necessary to truncate the expansion of the action in order to be able to perform calculations. This can be done systematically by considering  $z_2 - 1$  to be a small parameter, which is valid for  $T \gg 2J_2$ . The reason that this is a useful expansion parameter is due to the fact that  $\mathcal{S}_{2n}[a, b]$  has a lowest order contribution proportional to  $(z_2 - 1)^{n-1}$ . Thus for a chosen value of  $n$ , it is only necessary to consider terms in the action up to  $\mathcal{S}_{2n}[a, b]$ . A simple worked example on a finite-size lattice is given in Appendix D to show how this type of expansion works in detail. Here we will consider  $n = 2$ , and therefore only retain the  $\mathcal{S}_2[a, b]$  and  $\mathcal{S}_4[a, b]$  terms in the action, thus working at first order in the small parameter  $|z_2 - 1|$ .

The quartic term in the action can be determined by observing that for a 2-site unit cell there are 6 terms containing 4 Grassmann variables, and these are shown schematically in Fig. 15. Thus one finds,

$$\begin{aligned} \mathcal{S}_4[a, b] = (z_2 - 1) \sum_i & [z (b_i a_i b_{i+\hat{e}_y} a_{i+\hat{e}_x+\hat{e}_y} + b_i a_i a_{i+\hat{e}_x} b_{i+\hat{e}_x+\hat{e}_y} + b_i a_i b_{i-\hat{e}_x-\hat{e}_y} a_{i-\hat{e}_y} + b_i a_i a_{i-\hat{e}_x-\hat{e}_y} b_{i-\hat{e}_x}) \\ & + z^2 (b_i a_{i+\hat{e}_x} a_i b_{i+\hat{e}_y} + a_{i-\hat{e}_y} b_i b_{i-\hat{e}_x} a_i)] \end{aligned} \quad (63)$$

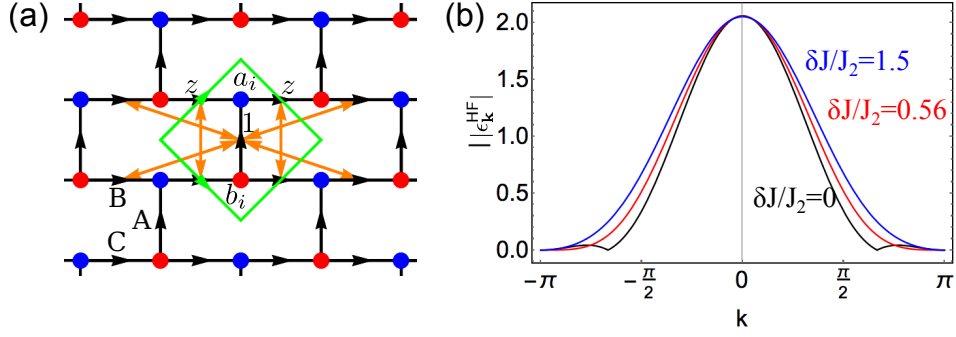


Figure 15: The interacting brick lattice and Hartree-Fock spectrum  $\epsilon_{\mathbf{k}}^{\text{HF}}$  [Eq. 73] used to perturbatively calculate  $\mathcal{Z}_{\text{hon2}}$  [Eq. 61]. (a) At first order in the perturbation expansion interactions occur between pairs of bonds that are on the same hexagon and separated by a single unfilled bond (shown in orange), resulting in a quartic interaction,  $\mathcal{S}_4[a, b]$  [Eq. 64]. Higher-order terms in the action are associated with connected pairwise interactions, and thus involve 3 or more bonds (b) The spectrum  $\epsilon_{\mathbf{k}}^{\text{HF}}$  [Eq. 73] at the temperature for which  $\epsilon_{(\pi,0)}^{\text{HF}}(T) = 0$  along the path  $\mathbf{k} = (k, k + \pi)$ . For  $\delta J/J_2 = 1.5$  (blue) the minimum of the dispersion occurs at  $\mathbf{k} = (\pi, 0)$ , indicating a second-order phase transition. For  $\delta J/J_2 = 0$  (black) there is an additional zero at  $\mathbf{k} \neq (\pi, 0)$ , indicating a break-down of the perturbation theory and a first-order phase transition. The crossover between these two types of behaviour occurs at  $\delta J/J_2 = 0.56$  (red), which corresponds to a Pokrovsky-Talapov tricritical point.

and taking the Fourier transform using Eq. 18 results in,

$$\mathcal{S}_4[a, b] = \frac{z_2 - 1}{N} \sum_{\mathbf{k}_1, \mathbf{k}_2, \mathbf{k}_3, \mathbf{k}_4} \delta_{\mathbf{k}_1 + \mathbf{k}_2 + \mathbf{k}_3 + \mathbf{k}_4, 0} V_4^{\text{sym}}(\mathbf{k}_1, \mathbf{k}_2, \mathbf{k}_3, \mathbf{k}_4) a_{\mathbf{k}_1} b_{\mathbf{k}_2} a_{\mathbf{k}_3} b_{\mathbf{k}_4}, \quad (64)$$

where,

$$V_4^{\text{sym}}(\mathbf{k}_1, \mathbf{k}_2, \mathbf{k}_3, \mathbf{k}_4) = \frac{1}{4} [V_4(\mathbf{k}_1, \mathbf{k}_2, \mathbf{k}_3, \mathbf{k}_4) - V_4(\mathbf{k}_3, \mathbf{k}_2, \mathbf{k}_1, \mathbf{k}_4) - V_4(\mathbf{k}_1, \mathbf{k}_4, \mathbf{k}_3, \mathbf{k}_2) + V_4(\mathbf{k}_3, \mathbf{k}_4, \mathbf{k}_1, \mathbf{k}_2)], \quad (65)$$

is the interaction vertex symmetrised over the pairs  $\{\mathbf{k}_1, \mathbf{k}_3\}$  and  $\{\mathbf{k}_2, \mathbf{k}_4\}$  and,

$$V_4(\mathbf{k}_1, \mathbf{k}_2, \mathbf{k}_3, \mathbf{k}_4) = z e^{-i \frac{k_{1x} - k_{1y}}{2}} \left[ z \left( e^{i \frac{k_{3x} + k_{3y}}{2}} e^{ik_{4y}} + e^{-i \frac{k_{3x} + k_{3y}}{2}} e^{-ik_{4x}} \right) + e^{i \frac{k_{3x} + 3k_{3y}}{2}} e^{ik_{4y}} - e^{-i \frac{3k_{3x} + k_{3y}}{2}} e^{-ik_{4x}} - e^{i \frac{k_{3x} + k_{3y}}{2}} e^{i(k_{4x} + k_{4y})} + e^{-i \frac{k_{3x} + k_{3y}}{2}} e^{-i(k_{4x} + k_{4y})} \right]. \quad (66)$$

The truncated action, which is given by the sum of  $\mathcal{S}_2[a, b]$  [Eq. 19] and  $\mathcal{S}_4[a, b]$  [Eq. 64], has a quartic interaction term, and therefore it is not possible to perform the path integral exactly. Instead a perturbative diagrammatic approach can be used, as is standard in quantum field theory [52]. It is important to note that the expansion order of the perturbation theory is set by the truncation of the action, and only diagrams consistent with this order should be considered.

The first step in the construction of a diagrammatic perturbation theory is the calculation of the free Green's function, and this is given by,

$$\langle a_{\mathbf{k}_1} b_{\mathbf{k}_2} \rangle_0 = \frac{1}{\mathcal{Z}_{\text{hon}}} \int \prod_{\mathbf{k}} da_{\mathbf{k}} db_{-\mathbf{k}} a_{\mathbf{k}_1} b_{\mathbf{k}_2} e^{\mathcal{S}_2[a, b]} = \frac{\delta_{\mathbf{k}_1 + \mathbf{k}_2, 0}}{\epsilon_{\mathbf{k}_1}}. \quad (67)$$

This can be used to perturbatively construct the interacting Green's function, which is given by,

$$\langle a_{\mathbf{k}_1} b_{\mathbf{k}_2} \rangle = \frac{1}{\mathcal{Z}_{\text{hon}}} \int \prod_{\mathbf{k}} da_{\mathbf{k}} db_{-\mathbf{k}} a_{\mathbf{k}_1} b_{\mathbf{k}_2} e^{\mathcal{S}_2[a,b] + \dots + \mathcal{S}_{2N}[a,b]} = \frac{\delta_{\mathbf{k}_1 + \mathbf{k}_2, 0}}{\tilde{\epsilon}_{\mathbf{k}_1}}, \quad (68)$$

where  $\tilde{\epsilon}_{\mathbf{k}} = \epsilon_{\mathbf{k}} + \Sigma_{\mathbf{k}}$  and  $\Sigma_{\mathbf{k}}$  is the self energy.

In the case we are considering, the anomalous Green's functions  $\langle a_{\mathbf{k}_1} a_{\mathbf{k}_2} \rangle$  and  $\langle b_{\mathbf{k}_1} b_{\mathbf{k}_2} \rangle$  vanish at all orders of perturbation theory, and this is related to the absence of defect triangles. In consequence the effective quadratic action takes the simple form,

$$\mathcal{S}_{2,\text{eff}}[a, b] = \sum_{\mathbf{k}} \tilde{\epsilon}_{\mathbf{k}} a_{\mathbf{k}} b_{-\mathbf{k}}, \quad (69)$$

and it follows that the partition function can be written as,

$$\mathcal{Z}_{\text{hon2}} = \prod_{\mathbf{k}} \tilde{\epsilon}_{\mathbf{k}}. \quad (70)$$

In order to be consistent with the expansion of the action to first order in the small parameter  $|z_2 - 1|$ , we consider the Hartree-Fock diagrams, and therefore approximate the self energy as,

$$\Sigma_{\mathbf{k}} \approx \Sigma_{\mathbf{k}}^{\text{HF}} = (z_2 - 1)\Omega_{\mathbf{k}}, \quad (71)$$

where,

$$\Omega_{\mathbf{k}} = \frac{1}{N} \sum_{\mathbf{k}'} \frac{2}{\epsilon_{\mathbf{k}'}} [V_4^{\text{sym}}(\mathbf{k}, -\mathbf{k}, \mathbf{k}', -\mathbf{k}') - V_4^{\text{sym}}(\mathbf{k}, -\mathbf{k}', \mathbf{k}', -\mathbf{k})]. \quad (72)$$

At this level of approximation the partition function is given by,

$$\mathcal{Z}_{\text{hon2}} \approx \prod_{\mathbf{k}} \epsilon_{\mathbf{k}}^{\text{HF}}, \quad \epsilon_{\mathbf{k}}^{\text{HF}} = \epsilon_{\mathbf{k}} + \Sigma_{\mathbf{k}}^{\text{HF}}. \quad (73)$$

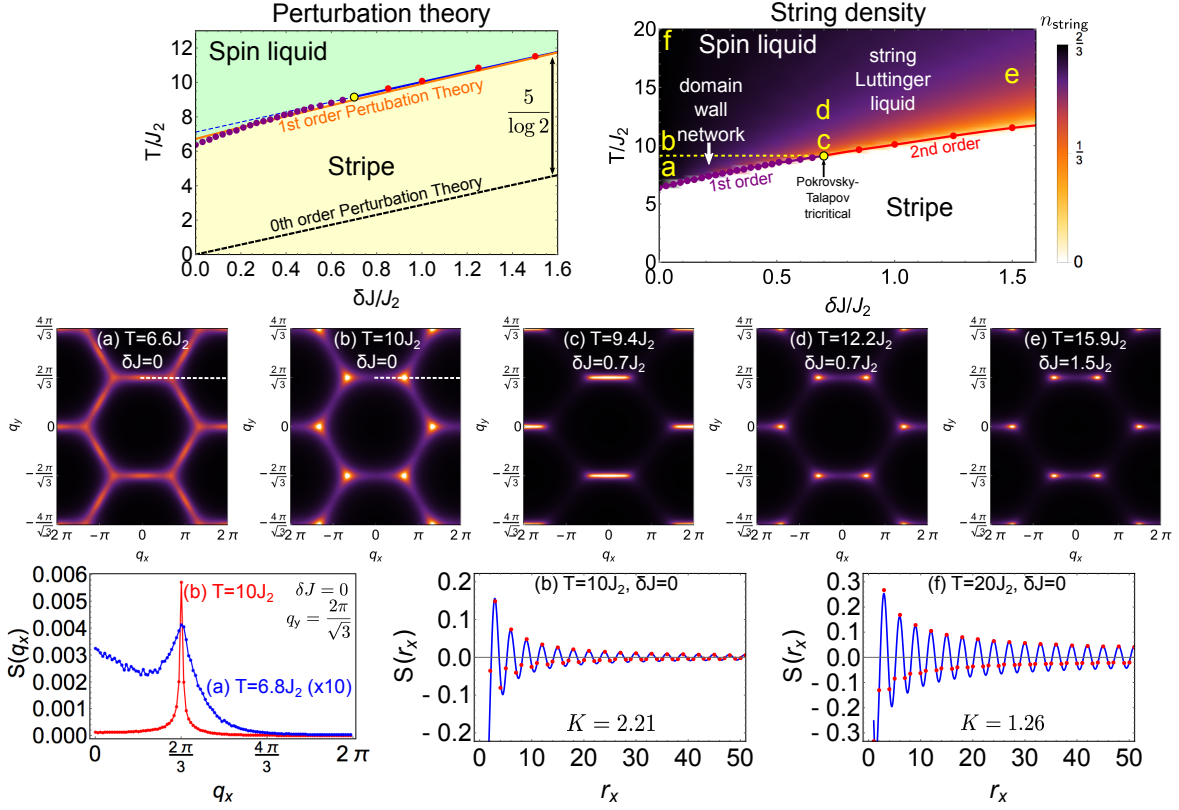


Figure 16: The phase diagram and structure factor of  $\mathcal{H}_{\text{ABB}_2}$  [Eq. 58] in the constrained manifold. (Top) Phase diagram showing the stripe-ordered and spin-liquid phases. First (purple), second (red) and Pokrovsky-Talapov tricritical (large yellow dot) transitions are determined from finite-size scaling analysis of Monte Carlo simulations [Eq. 75], and in the case of the second-order transition compare well to the exact value (blue solid line). Zeroth (black-dashed) and first-order (orange) perturbation theory calculations of the critical temperature (orange) are shown on the left hand plot (i.e. the temperature at which  $\epsilon_{(\pi,0)}^{\text{HF}} = 0$  [Eq. 69]). On the right-hand plot the spin-liquid is split into a string Luttinger liquid for  $T > T_{\text{tri}} = 9.14J_2$  and a domain-wall network for  $T < T_{\text{tri}}$  (separated by dashed yellow line). (Middle) Structure factor  $S(\mathbf{q})$  [Eq. 32] calculated by Monte Carlo simulation of an  $L = 72$  hexagonal cluster (letters correspond to those on the phase diagram). (Bottom) Cuts through both  $S(\mathbf{q})$  and  $S(\mathbf{r})$ . (a) For  $\delta J = 0$  and close to the first-order phase transition  $S(\mathbf{q})$  has significant spectral weight around the perimeter of the triangular-lattice Brillouin zone, as is typical of a domain-wall network. (b) On increasing the temperature spectral weight rapidly accumulates at  $\mathbf{q} = (\pm 2\pi/3, 2\pi/\sqrt{3})$ , as is typical for a string Luttinger liquid. In the whole string Luttinger liquid region the asymptotic form of  $S(\mathbf{r})$  follows Eq. 77 with a parameter-dependent Luttinger parameter,  $K \geq 1$ . (c) At temperatures just above the Pokrovsky-Talapov tricritical point, there is a near-degeneracy between string sectors and the structure factor therefore shows extended spectral weight in the  $q_x$  direction. (d) Further increasing the temperature breaks this quasi-degeneracy and sharp peaks form at  $\mathbf{q}_{\text{string}}(T) = (\pm \pi n_{\text{string}}, 2\pi/\sqrt{3})$ . (e) At temperatures just above the second-order transition the structure factor is sharply peaked at  $\mathbf{q}_{\text{string}}(T)$ . (f) For  $T \gg J_2$  the behaviour of the nearest-neighbour TLIAF in the constrained manifold is recovered, with  $K = 1$ .

The effective action  $\mathcal{S}_{2,\text{eff}}[a, b]$  [Eq. 69] can be used to study the physical properties of the system, as in Section 4.1. In particular we focus on the crossover between a second and first-order phase transition, which corresponds to the crossover from the weak to the strong coupling regimes (in fermionic language). Information about the nature of the phase transition can be extracted from the spectrum,  $\epsilon_{\mathbf{k}}^{\text{HF}}$  [Eq. 73], and it can be seen in Fig. 15 that this undergoes a change of structure at  $\delta J/J_2 = 0.56$ .

For  $\delta J/J_2 > 0.56$  the spectrum,  $\epsilon_{\mathbf{k}}^{\text{HF}}$  [Eq. 73], shows the characteristic features of a second-



order transition. In the disordered phase it has a gapless point at a temperature-dependent and incommensurate wavevector. As the temperature is lowered towards the critical point the gapless point migrates towards the wavevector  $\mathbf{k} = (\pi, 0)$ , and the critical temperature can be found from solving the equation  $\epsilon_{(\pi,0)}^{\text{HF}}(T) = 0$ . Below the transition the spectrum is gapped at all wavevectors, and the minimum is at  $\mathbf{k} = (\pi, 0)$ .

The second-order transition temperature is known exactly from Eq. 59, and Fig. 16 shows a comparison between the exact value and the estimate from first-order perturbation theory. While the two only become equal in the limit  $\delta J/J_2 \rightarrow \infty$ , first-order perturbation theory can be seen to give a good estimate of the critical temperature even in the region  $\delta J/J_2 \sim 1$ . This is surprising given the extreme inaccuracy of zeroth order perturbation theory, where the  $J_2$  interaction is ignored and the critical temperature is given by Eq. 24. The reason for this discrepancy can be understood by making an expansion of the exact critical temperature in terms of  $J_2/\delta J$ , which gives,

$$\frac{T_K}{\delta J} = \frac{2}{\log 2} + \frac{5}{\log 2} \frac{J_2}{\delta J} + \mathcal{O}\left(\frac{J_2^2}{\delta J^2}\right). \quad (74)$$

The second term in the expansion, which is negligible for  $\delta J/J_2 \rightarrow \infty$ , is larger than the first term in the region  $\delta J/J_2 \sim 1$ , and, since it is captured by first but not zeroth order perturbation theory, explains the discrepancy. Given the accuracy of the first-order perturbation theory, higher order terms must be either relatively unimportant or cancel one another, even for  $\delta J/J_2 \sim 1$ .

Exactly at the critical temperature the spectrum has qualitatively the same behaviour as the  $J_2 = 0$  case (see Section 4.1) close to the gapless point. Along the path  $\mathbf{k} = (k, k + \pi)$  the spectrum grows as  $(k - \pi)^2$ . This behaviour is typical of a Pokrovsky-Talapov transition [41, 42], and this type of phenomenological approach will be developed further in Section 5.

At  $\delta J/J_2 = 0.56$  the spectrum shows a change of character. The coefficient in front of the quadratic term goes to zero, and the spectrum grows as  $(k - \pi)^4$  around the gapless point. We refer to this point as a Pokrovsky-Talapov tricritical point, as the critical exponents are different from the standard ones of the Kasteleyn transition. This change of behaviour is not just an artifact of first-order perturbation theory, since its effects can be observed in Monte Carlo simulation (albeit at  $\delta J/J_2 = 0.7$  – see Section 4.3.3).

For  $\delta J/J_2 < 0.56$  the perturbative approach breaks down, but can be used to find some clues as to the true situation. In the paramagnet there is a gapless point at an incommensurate wavevector, as shown for the case of  $\delta J = 0$  in Fig. 17. As the temperature is reduced this migrates towards  $\mathbf{k} = (\pi, 0)$ , as is the case for a second-order transition. However, before the gapless point reaches  $\mathbf{k} = (\pi, 0)$  the gap at  $\mathbf{k} = (\pi, 0)$  closes, resulting in a pair of gapless points. This situation is not physical, and does not obviously correspond to the expected first-order phase transition. However, it can be seen that the spectrum is very flat between the two gapless points. We suggest that in reality gapless lines should develop in this region, and this would correspond to a first-order phase transition. This type of behaviour can never be exactly recovered using a perturbative approach, since a gapless line relies on the correct relationship between all coefficients in the expansion of the free energy. A phenomenological theory for the spectrum at a first-order transition will be further developed in Section 5.

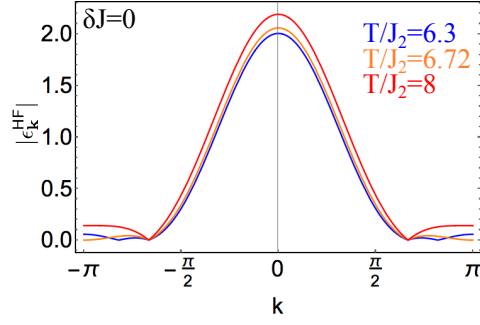


Figure 17: The spectrum  $\epsilon_{\mathbf{k}}^{\text{HF}}$  [Eq. 73] at  $\delta J = 0$  and for varying temperature. The path through 2D reciprocal space is parametrised by  $\mathbf{k} = (k, k + \pi)$ . In the paramagnet (red) there is a single gapless point in the region  $k > 0$  and this occurs at an incommensurate wavevector. At  $T/J_2 = 6.72$  (orange) the gap at  $\mathbf{k} = (\pi, 0)$  closes, but there remains a gapless point at an incommensurate wavevector. At lower  $T$  (blue) the gapless points approach one another, and the spectrum is very flat in their vicinity. While it is clear that the perturbative approach has broken down at such a small value of  $\delta J/J_2$ , the results are suggestive that lines of zeros appear in the spectrum, and this would be consistent with a first-order phase transition.

### 4.3.3 Phase diagram determined from Monte Carlo simulations

As a complement to the perturbation theory approach, we also study  $\mathcal{H}_{\text{ABB2}}$  [Eq. 58] using Monte Carlo simulation. In this section we show the results for the phase diagram, but postpone the study of critical exponents until Section 5, since it is first necessary to develop phenomenological and scaling theories.

The simulations are carried out using a worm algorithm very similar to that presented in [11]. This works in the dimer representation (see Section 2.1), and creates loops of alternating dimer-filled and empty bonds, which are then flipped, resulting in the reversal of all the Ising spins contained within the loop. The loop creation is carefully controlled such that detailed balance is maintained, and the absence of rejection results in an efficient algorithm. Hexagonal shaped clusters with periodic boundary conditions are used, containing  $N = 3L^2$  Ising spins, where  $L$  measures the length of one side. Simulations are performed using system sizes from  $L = 24$  up to  $L = 192$ .

The phase diagram of  $\mathcal{H}_{\text{ABB2}}$  [Eq. 58], as determined by Monte Carlo simulation, is shown in Fig. 16. The phase transitions can be located either from measuring the triangular average of the winding number and associated susceptibility, defined in Eq. 7 and Eq. 8, or by measuring the heat capacity, and the results are consistent.

In the region where the phase transition is second order, the critical temperature is found from finite-size scaling analysis. We use the standard relation for a Kasteleyn transition [53],

$$T_{\mathbf{k}}(L) = T_{\mathbf{k}}(\infty) - cL^{-1/\nu_{\parallel}}, \quad (75)$$

where  $c$  is a constant,  $L$  is the linear dimension of the system and  $\nu_{\parallel} = 1$  is the critical exponent of the correlation length in the direction parallel to the double domain walls, below which the algebraic scaling of spin correlations breaks down [42, 54, 46]. We consider the parallel correlation length,  $\nu_{\parallel}$ , rather than the perpendicular correlation length,  $\nu_{\perp}$ , due to the anisotropy of the system which results in  $\nu_{\perp} = 1/2 \neq \nu_{\parallel}$ . Since the clusters used in the simulations are hexagonal in shape, and therefore isotropic, the growth of correlations parallel to the strings dominates the finite size effects. The exact second-order transition temperature is known from solving Eq. 59, and it can be seen in Fig. 16 that the finite-size-scaled Monte Carlo results are in good agreement with this.

The line of second order transitions ends at a Pokrovsky-Talapov tricritical point, which is found to be at  $\delta J/J_2 = 0.7$  and  $T = T_{\text{tri}} = 9.14J_2$ . The presentation of the evidence for this is postponed until Section 5, since it is first necessary to develop a phenomenological theory for the critical exponents. The findings from Monte Carlo can be seen to be in reasonable agreement with first order perturbation theory (see Section 4.3.2), where a Pokrovsky-Talapov tricritical point was found at  $\delta J/J_2 = 0.56$ .

For  $\delta J/J_2 < 0.7$  the transition is first order, and it is typically possible to simulate large-enough systems that the finite-size effects are small. In consequence the transition temperatures plotted in Fig. 16 are taken from the largest simulated systems. For  $0.5 < \delta J/J_2 < 0.7$  this is  $L = 192$ , while for  $\delta J/J_2 < 0.5$  it is sufficient to consider  $L = 48$ .

#### 4.3.4 Monte Carlo simulations in the 2-string sector

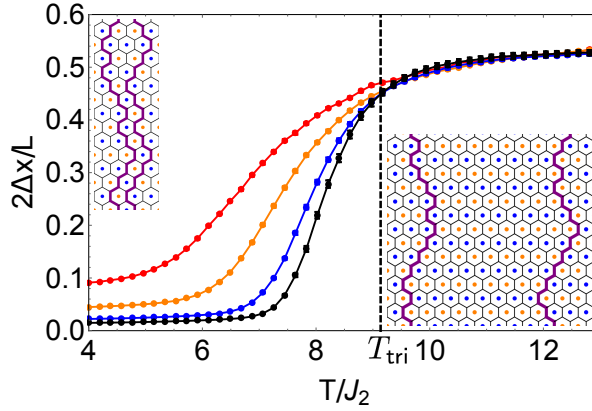


Figure 18: The average separation of a pair of strings,  $2\Delta x/L$  [Eq. 76]. Monte Carlo simulations are carried out in a reduced manifold of Ising configurations, constrained to have exactly two strings. The simulations use a square cluster with linear sizes  $L = 24$  (red),  $L = 48$  (orange),  $L = 96$  (blue) and  $L = 144$  (black). At low temperature the strings bind together (see left-hand inset), while at higher temperatures the strings repel one another (see right-hand inset). The dashed line shows the temperature of the Pokrovsky-Talapov tricritical point,  $T_{\text{tri}}$ , as measured by Monte Carlo simulation (see Fig. 16).

In order to gain physical insight into the crossover between a second and first-order phase transition, which in the spin-liquid region corresponds to the crossover between weak and strong coupling, we perform Monte Carlo simulations in a reduced manifold of states. The number of strings is fixed to be two, and the idea is to study the interaction between a pair of strings.

Monte Carlo simulations are performed on a square cluster with periodic boundary conditions, linear dimension  $L$  and total number of sites  $L^2$ . In the 2-string manifold, allowed Ising configurations are distinguished by their  $J_2$  energy, but all have the same energy in terms of  $\delta J$ , since there are a fixed number of dimers occupying B and C bonds. In consequence it is not necessary to vary  $\delta J/J_2$ , but only  $T/J_2$ . This shows that the string-string interactions are independent of  $\delta J$ , and therefore the temperature at which weak coupling crosses over to strong coupling is also  $\delta J$  independent.

For each considered temperature we measure the average separation between the strings, taking into account the periodic boundary conditions, and this is given by,

$$\Delta x = \langle \min[x_2 - x_1, L - (x_2 - x_1)] \rangle, \quad (76)$$

where  $x_1$  and  $x_2$  are the positions of the strings along the  $x$  axis at a given height.

It can be seen in Fig. 18 that as the temperature is reduced there is a change in  $\Delta x$  starting at about  $T = T_{\text{tri}}$ . For  $T > T_{\text{tri}}$  the strings repel one another, and  $\Delta x/(L/2) \approx 1/2$ . This repulsion is entropically driven, and is due to the no-crossing constraint obeyed by the strings, which reduces the available fluctuations of a string if it is in close proximity to another string. This type of pairwise repulsion is crucial for the existence of a second-order phase transition out of the stripe phase, since it limits the number of strings that are condensed into the system when the free energy of an isolated,  $f_{\text{string}}$  [Eq. 59], goes to zero.

For  $T < T_{\text{tri}}$  the pair of strings start to approach one another, showing that the energetically-driven attractive interaction starts to dominate over the repulsive interaction. The strings gain some binding free energy by being, on average, proximate to one another, and this is consistent with the crossover from a second to a first-order phase transition at  $T = T_{\text{tri}}$  seen in the full Monte-Carlo simulations (see Fig. 16). The lower the temperature the more tightly the strings bind, suggesting that the transition should become more first-order as the temperature is decreased, and this is also consistent with the full simulations.

Since the string-string interactions are independent of  $\delta J$ , the spin liquid region should have attractive string-string interactions in the temperature window  $T_1 < T < T_{\text{tri}}$ , and we will discuss the implications of this in the next section.

### 4.3.5 Mapping to 1D quantum model and correlations

The nature of the correlations in  $\mathcal{H}_{\text{ABB2}}$  [Eq. 58] can be used to understand the behaviour of the spin liquid, and can be determined by combining Monte Carlo simulation of the spin structure factor with insights from fermionic mappings.

It is useful to first consider at a qualitative level how the mapping to a 1D quantum model of spinless fermions is altered by the further-neighbour interactions (see Section 4.1.5 and Appendix C for the nearest-neighbour case). At the level of an isolated string the  $J_2$  interaction both increases the internal energy, and adds an energy penalty to ‘‘corners’’ where the string changes direction [10, 11]. In the fermion model this alters the values of  $\mu$  and  $t$  and adds a history dependence to the motion of the fermion, such that the passage from the imaginary timestep  $\tau$  to  $\tau + \Delta\tau$  depends not only on the fermion configuration at  $\tau$  but also on the configuration at  $\tau - \Delta\tau$ .

A second effect of the  $J_2$  coupling is to drive an attractive interaction between strings. When strings neighbour one another their  $J_2$  energy is reduced, and therefore the fermionic model also has an attractive interaction of the form  $V(z_2)c_i^\dagger c_i c_{i+1}^\dagger c_{i+1}$ . In the string picture this attractive interaction is energetically-driven and competes with the entropically-driven repulsive interaction arising from the string non-crossing constraint. In the fermionic language the entropic repulsion maps onto the Pauli exclusion principle, which is a property of free fermions, and therefore the fermionic model is always attractive.

One advantage of mapping onto a fermion model is that it is known that fermions with weak attractive interactions form a Luttinger liquid, with Luttinger parameter  $K > 1$  ( $K = 1$  for free fermions) [55]. We therefore make the ansatz that the spin structure factor in the 2D classical model takes the asymptotic form [54, 55],

$$S(\mathbf{r}) \propto \frac{\cos[\mathbf{q}_{\text{string}} \cdot \mathbf{r}]}{|\mathbf{r}|^{\frac{K}{2}}}, \quad (77)$$

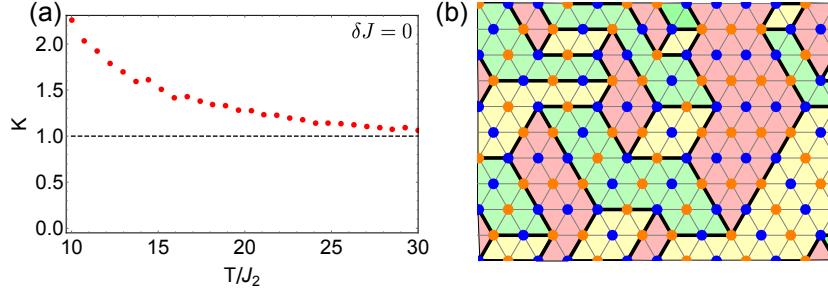


Figure 19: String Luttinger liquid and domain-wall network states. (a) The String Luttinger liquid is characterised by the parameter,  $K$ , and this is determined from Monte Carlo simulations of an  $L = 72$  hexagonal cluster by fitting  $S(\mathbf{r})$  with the asymptotic form given in Eq. 77. This type of fitting breaks down at  $T \approx T_{\text{tri}} = 9.14J_2$  (b) Snapshot of a domain-wall network configuration, taken from a Monte Carlo simulation at  $\delta J = 0$  and  $T = 6.5J_2$ . Domains have stripes parallel to A (red), B (green) or C (yellow) bonds. A domains correspond to an absence of strings while B and C domains to parallel neighbouring strings, and this type of configuration is driven by string-string attraction.

where  $K > 1$ . This corresponds to a reciprocal space structure factor with algebraically sharp peaks at  $\mathbf{q} = \mathbf{q}_{\text{string}}$ . The asymptotic form given in Eq. 77 can be tested against Monte Carlo simulations, and we find that it gives a good fit to the simulations for  $T \gtrsim T_{\text{tri}}$ , and some examples are shown in Fig. 16. The value of  $K$  can be extracted from the fits to the simulations, and the result of doing this for  $T > T_{\text{tri}}$  and  $\delta J = 0$  is shown in Fig. 19. It can be seen that close to  $T = T_{\text{tri}}$  the Luttinger parameter,  $K$ , becomes significantly different from the free fermion case of  $K = 1$ , while in the limit  $T/J_2 \rightarrow \infty$  the free fermion case is recovered, corresponding to  $1/\sqrt{|\mathbf{r}|}$  spin correlations (see Eq. 33). As a result of these findings we label the region of the spin liquid with  $T > T_{\text{tri}}$  as a string Luttinger liquid.

At  $T = T_{\text{tri}}$  the entropic repulsion and energetic attraction between strings becomes comparable (see Fig. 18) and the strings start to bind together. At this temperature the distribution of spectral weight in the structure factor starts to rearrange itself such that  $S(\mathbf{q})$  is no longer dominated by a single  $\mathbf{q}$  value, and Eq. 77 is inapplicable. Instead the weight is distributed around the perimeter of the triangular-lattice Brillouin zone (see Fig. 16), and this is typical of a domain-wall network (see supplementary material of [11]). Neighbouring parallel strings form domains in which Ising stripes are parallel to either B or C bonds, while domains with stripes parallel to A bonds correspond to an absence of strings, and an example of this is shown in Fig. 19. We find that the spin-liquid region of  $\mathcal{H}_{\text{ABB}_2}$  [Eq. 58] is best described as a domain-wall network in the region  $T_1 < T < T_{\text{tri}}$ , as shown in Fig. 16. The domain-wall network state can be thought of as being a fluctuating, phase-separated state, with a loose analogy to the clustering of holes in superconductors [56, 57].

The more the energetically-driven attraction between strings dominates over the entropic repulsion, the more tightly bound the strings and the larger the average domain size. In the case of  $\mathcal{H}_{\text{ABB}_2}$  [Eq. 58] and for  $\delta J = 0$  a first-order phase transition into the stripe phase occurs while the average domain size is relatively small. The addition of a third-neighbour interaction with  $0 < J_3 < J_2/2$  suppresses the transition temperature, and therefore allows the average domain size to become larger since the attractive interaction becomes more important at low temperature [10, 11].

Increasing  $\delta J$  causes domains with stripes parallel to A bonds to grow, which corresponds to decreasing the string density,  $n_{\text{string}}$ . At the tricritical point the A-domains coalesce and cover the whole system and there is a continuous transition into the stripe phase.

## 5 Phenomenological theory of the phase transition

In order to connect the insights gained from studying toy models in Section 4 to the dipolar TLIAF,  $\mathcal{H}_{\text{dip}}$  [Eq. 1], it is useful to construct a phenomenological theory that applies close to the phase transition. The theory we construct interpolates the four different regions of critical behaviour – first order for  $\delta < 0.022$ , tricritical for  $\delta = 0.022$ , Pokrovsky-Talapov for  $0.022 < \delta \lesssim 0.1$  and Ising for  $\delta \gtrsim 0.1$  – and this is done using essentially three parameters, one that depends on temperature, one that depends on the distortion and one that measures the energy cost of defect triangles. This allows predictions to be made for the critical exponents in the four different regions, and we construct finite-size scaling hypotheses for Monte Carlo simulation data that can be tested using the toy models and that will be used in Section 6 to analyse the dipolar TLIAF.

### 5.1 Pokrovsky-Talapov second-order transition

Phenomenological theories of a second-order Kasteleyn/Pokrovsky-Talapov phase transition have already been considered in the literature in a variety of contexts, including adsorption of gas monolayers onto solid surfaces [42, 54, 46] and anisotropic square-lattice Ising models with competing interactions [47, 48]. The theory we construct here has a similar content to previous theories, but we include a relatively detailed discussion in order to make explicit the connection to triangular-lattice Ising models and as a useful starting point from which to construct theories in other regions of the phase diagram.

The phenomenological theory we construct is expressed in terms of a 1D quantum model of spinless fermions. In this construction the worldlines of the fermions represent strings in the 2D classical model (see Section 2.2 for the definition of strings), and the Pauli exclusion principle is equivalent to the hardcore string repulsion.

When working in the constrained Ising manifold, we consider an effective Hamiltonian,

$$\mathcal{H}_{1\text{D}} = \sum_q \omega_q c_q^\dagger c_q. \quad (78)$$

In the case of the 2D classical model with only nearest-neighbour interactions,  $\mathcal{H}_{\text{ABB}}$  [Eq. 10], the mapping onto this 1D quantum model is relatively simple (see Section 4.1.5 and Appendix C). In more complicated classical models with longer-range interactions, such as  $\mathcal{H}_{\text{ABB2}}$  [Eq. 58] or  $\mathcal{H}_{\text{dip}}$  [Eq. 1], the exact 1D quantum Hamiltonian will also include fermion-fermion interaction terms. However, since the fermion/string density is vanishingly small close to the transition, these interactions can be considered to just renormalise the parameters appearing in  $\omega_q$ .

The dispersion  $\omega_q$  is in general not known exactly, but close to the phase transition and for small  $q$  it can be approximated by,

$$\omega_q = a(T_{\text{K}} - T) + bq^2 + \dots \quad (79)$$

where  $a > 0$ ,  $b > 0$  and the tunable parameter  $T$  is understood to be the temperature of the 2D classical model (in terms of the 1D quantum model  $T$  is just a tuneable parameter and not related to temperature). In the case of the nearest-neighbour model  $\mathcal{H}_{\text{ABB}}$  [Eq. 10], one finds  $a = 2 \log 2/T_{\text{K}}$  and  $b = 1/4$ , while for more complicated models  $a$  and  $b$  can be treated as phenomenological parameters.



A phase transition between the fermion vacuum (stripe phase) and a phase with a finite density of fermions (spin liquid) occurs at  $T = T_K$ . For  $T < T_K$  all fermion states have positive energy, and therefore there are no fermions in the ground state. Furthermore, excitations cost an energy of at least  $a(T_K - T)$ , and the system is insulating. For  $T > T_K$  the filling of the negative energy states results in a Fermi wavevector  $q_f = \sqrt{a(T - T_K)/b}$ . The system is gapless and therefore metallic, and there is an approximately linear dispersion for low-energy excitations.

The density of strings in the 2D classical model is equal to the density of fermions in the 1D quantum model, and can be very simply calculated as,

$$n_{\text{string}} = \frac{1}{\pi} \int_0^{q_f} dq = \frac{q_f}{\pi}, \quad (80)$$

and therefore,

$$n_{\text{string}} = \begin{cases} 0 & T < T_K \\ \frac{1}{\pi} \sqrt{\frac{a(T - T_K)}{b}} & T > T_K \end{cases} \quad (81)$$

In the metallic (spin liquid) phase one can write  $n_{\text{string}} \propto (T - T_K)^\beta$ , which leads to the identification of the critical exponent  $\beta = 1/2$ .

The free energy of the classical 2D model is given by the energy of the 1D quantum model, and therefore one can derive a Ginzburg-Landau type theory from  $\omega_q$  [Eq. 79],

$$F_{\text{PT}} = \frac{1}{\pi} \int_0^{q_f} \omega_q dq = a(T_K - T)n_{\text{string}} + \frac{b\pi^2}{3}n_{\text{string}}^3 + \dots \quad (82)$$

where  $n_{\text{string}} = q_f/\pi$  has been used. This is the phenomenological model analysed in [42], where it is shown that the cubic term encapsulates the entropic repulsion between strings.

When performing Monte Carlo simulations of analytically intractable models, such as  $\mathcal{H}_{\text{dip}}$  [Eq. 1], measurement of the critical exponent  $\beta = 1/2$  for the string density,  $n_{\text{string}}$ , would provide convincing evidence that the critical behaviour in question is in the Pokrovsky-Talapov universality class. In practice finite-size effects make it difficult to measure such an exponent directly. Instead one can make a scaling hypothesis for  $n_{\text{string}}$  and use this to determine  $\beta$ . We consider,

$$n_{\text{string}}(T, L) = (T - T_K)^\beta g_{\text{PT}} \left( \frac{L}{\zeta_{\parallel}} \right), \quad (83)$$

where  $g_{\text{PT}}$  is an unknown scaling function and  $\zeta_{\parallel}$  is the correlation length in the direction parallel to the domain walls, below which the asymptotic form of the structure factor given in Eq. 33 does not apply. As discussed in Section 4.1.4, in the critical region  $\zeta_{\parallel} \propto (T - T_K)^{-\nu_{\parallel}}$  with  $\nu_{\parallel} = 1$ , and this can be compared to the correlation length perpendicular to the domain walls, which is given by  $\zeta_{\perp} \propto (T - T_K)^{-\nu_{\perp}}$  with  $\nu_{\perp} = 1/2$  [42, 54, 46]. Since we typically consider hexagonal shaped clusters, finite-size effects will be dominated by  $\zeta_{\parallel}$ , since this diverges faster than  $\zeta_{\perp}$ .

In practice we simulate the system at a number of different temperatures, and then find the values of  $\beta$  and  $\nu_{\parallel}$  for which the data best collapse onto a single curve. In order to test the goodness of collapse, we use the measure proposed in [58].



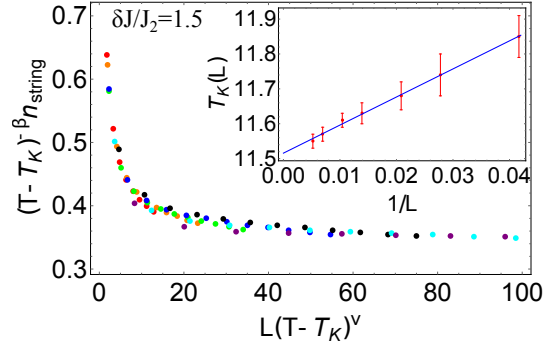


Figure 20: Data collapse demonstrating a second-order Pokrovsky-Talapov phase transition. The model in question is  $\mathcal{H}_{\text{ABB2}}$  [Eq. 58] in the constrained manifold and  $\delta J/J_2 = 1.5$ . Simulations are run on hexagonal clusters with  $N = 3L^2$  and  $L = 24$  (red),  $L = 36$  (orange),  $L = 48$  (green),  $L = 72$  (blue),  $L = 96$  (black),  $L = 144$  (cyan),  $L = 192$  (purple). The data are plotted according to the scaling hypothesis given in Eq. 83, and the best collapse is found for  $\beta = 0.47 \pm 0.04$  and  $\nu_{\parallel} = 1.05 \pm 0.09$ . This is consistent with  $\beta = 1/2$  and  $\nu_{\parallel} = 1$ , which are the expected values for a second-order Pokrovsky-Talapov transition. The inset shows the scaling of the critical temperature, which follows Eq. 75.

As an example of such data collapse one can consider  $\mathcal{H}_{\text{ABB2}}$  [Eq. 58] in the constrained manifold. We set  $\delta J/J_2 = 1.5$ , since this is far enough from the tricritical point that deviations from the Pokrovsky-Talapov universality class are expected to be negligible. The results are shown in Fig. 20, and a convincing data collapse is found for  $\beta = 0.47 \pm 0.04$  and  $\nu_{\parallel} = 1.05 \pm 0.09$ , which is consistent with the expected  $\beta = 1/2$  and  $\nu_{\parallel} = 1$ .

## 5.2 Pokrovsky-Talapov to Ising crossover

Next we consider a phenomenological theory of how a Pokrovsky-Talapov, second-order transition can turn into an Ising transition. This is relevant for  $\mathcal{H}_{\text{dip}}$  [Eq. 1], where for small distortions (e.g.  $\delta = 0.05$ ) the transition is indistinguishable from a Pokrovsky-Talapov transition, while for larger distortions (e.g.  $\delta = 0.2$ ) it is in the Ising universality class (see Section 6 for simulation results showing these features).

In the unconstrained Ising manifold, where defect triangles are allowed, the second-order phase transition is always in the Ising universality class. However, defect triangles typically have a high energy cost, and at low temperatures they occur with a very low probability. In consequence the temperature window over which an Ising transition is relevant is exponentially suppressed, and to all intents and purposes the transition is in the Pokrovsky-Talapov universality class. If the transition temperature is increased, for example by distorting the lattice, it can become comparable with the energy cost of creating defect triangles, and as a result the Ising temperature window becomes significant.

Defect triangles act as sources and sinks of pairs of strings (see Fig. 3), and therefore a 1D quantum model of fermions has to include pair creation and annihilation. In consequence we consider the 1D quantum Hamiltonian,

$$\mathcal{H}_{\text{1D}} = \sum_{q>0} \left[ A_q \left( c_q^\dagger c_q + c_{-q}^\dagger c_{-q} \right) + B_q \left( c_q^\dagger c_{-q}^\dagger + c_{-q} c_q \right) \right], \quad (84)$$

which should be understood as an effective Hamiltonian to describe a system of interacting fermions. Close to the phase transition the parameter  $A_q$  can be expanded in even powers of

$q$  as,

$$A_q = a(T_c - T) + bq^2 + \mathcal{O}(q^4), \quad (85)$$

while  $B_q$  can be expanded in odd powers of  $q$  as,

$$B_q = 4qe^{-\frac{E_{\text{def}}}{2T}} + \mathcal{O}(q^3), \quad (86)$$

where  $E_{\text{def}}$  is a measure of the energy cost of a defect triangle.

As in Section 4.2.5,  $\mathcal{H}_{1D}$  [Eq. 84], can be diagonalised by a Bogoliubov transformation, resulting in,

$$\mathcal{H}_{1D} = \sum_q \omega_q a_q^\dagger a_q + \frac{1}{2} \sum_q (A_q - \omega_q), \quad (87)$$

where  $\omega_q = \sqrt{A_q^2 + B_q^2}$  and  $a_q$  and  $a_q^\dagger$  are defined as in Eq. 146.

For  $T < T_c$  the dispersion,  $\omega_q$ , is gapped. However, the fermion density is not strictly zero, but instead follows a similar functional form to that shown for  $n_{\text{string}}$  in Fig. 11, with a low but non-zero density that increases with temperature. At the critical point,  $T = T_c$ , the gap closes and there is a rapid change in the fermion density. For  $T > T_c$  the gap in  $\omega_q$  reopens and the system forms a p-wave superconductor. This is the 1D quantum analogue of the 2D classical paramagnet.

Close to the phase transition it can be seen that the minimum of the dispersion occurs at  $q = 0$  for  $T_c < T < T_{\text{Is}}$ , where,

$$T_{\text{Is}} = T_c + \frac{8}{ab} e^{-\frac{E_{\text{def}}}{T}}. \quad (88)$$

In this region the gap is given by  $\omega_0 = |a(T - T_c)|$ , and therefore the correlation length goes as  $\xi_{\text{Is}} \sim |T - T_c|^{-1}$ , which is typical of a 2D Ising transition [49]. On the low-temperature side of the transition it is also possible to show that the order parameter,  $m_{\text{stripe}}$  [Eq. 5], has the Ising behaviour  $m_{\text{stripe}} \sim (T_c - T)^{1/8}$  [49].

For  $T > T_{\text{Is}}$  the system no longer exhibits critical behaviour in the Ising universality class and crosses over to Pokrovsky-Talapov critical behaviour. If  $T \ll E_{\text{def}}$  then the Ising temperature window is negligible, and the universality class of the transition is to all intents and purposes in the Pokrovsky-Talapov class.

In order to test for Ising behaviour in simulations one can check for data collapse using the Ising order parameter  $m_{\text{stripe}}$  [Eq. 5] and the scaling hypothesis,

$$m_{\text{stripe}}(T, L) = (T - T_K)^\beta g_{\text{Is}} \left( \frac{L}{\xi_{\text{Is}}} \right), \quad (89)$$

where it is expected that data collapse occurs for  $\beta = 1/8$  and  $\xi_{\text{Is}} \sim |T - T_c|^{-1}$ .

### 5.3 Pokrovsky-Talapov/Ising tricritical point

Exactly at the point at which a second-order phase transition changes into a first-order phase transition there is a change in the critical exponents, signifying that the universality class is no longer Ising or Pokrovsky-Talapov. Depending on the details of the system in question, this can be either an Ising or Pokrovsky-Talapov tricritical point.

First we consider a Pokrovsky-Talapov tricritical point, and construct a simple phenomenological model that can be tested against simulation data. This type of Pokrovsky-Talapov tricriticality can, for example, be found in the model  $\mathcal{H}_{\text{ABB2}}$  [Eq. 58] in the constrained manifold, and this can be used to guide the phenomenological model. In particular the perturbation theory analysis presented in Section 4.3.2 shows a change in the structure of  $\tilde{\epsilon}_{\mathbf{k}}$  [Eq. 69], and this is closely related to the 1D fermionic dispersion  $\omega_q$ .

We consider the same quantum 1D model of fermions,  $\mathcal{H}_{1\text{D}}$ , as in Eq. 78, but with the dispersion,

$$\omega_q = a(T_{\text{K}} - T) + bq^2 + cq^4 + \dots \quad (90)$$

where  $a > 0$ ,  $c > 0$  and  $b(\delta - \delta_{\text{tri}})$  is an odd function of  $\delta - \delta_{\text{tri}}$  that changes sign when  $\delta = \delta_{\text{tri}}$ . When  $b = 0$  the Fermi wavevector is given by,

$$q_{\text{f}} = \left( \frac{a(T - T_{\text{K}})}{c} \right)^{\frac{1}{4}}, \quad (91)$$

and it follows that the density of fermions (strings) in the metallic (paramagnetic) phase is given by,

$$n_{\text{string}} = \begin{cases} 0 & T < T_{\text{c}} \\ \frac{1}{\pi} \left( \frac{a(T - T_{\text{K}})}{c} \right)^{\frac{1}{4}} & T > T_{\text{c}} \end{cases} \quad (92)$$

which results in a critical exponent of  $\beta = 1/4$ .

As in Section 5.1, the free energy of the 2D classical model can be expanded in terms of  $n_{\text{string}}$ , and is given by,

$$F_{\text{tri}} = a(T_{\text{K}} - T)n_{\text{string}} + \frac{c\pi^4}{5}n_{\text{string}}^5 + \dots, \quad (93)$$

where it can be seen that the cubic terms describing the string-string repulsion has disappeared.

In order to test for the presence of a Pokrovsky-Talapov tricritical point in Monte Carlo simulations one can use the scaling hypothesis,

$$n_{\text{string}}(T, L) = (T - T_{\text{K}})^{\beta} g_{\text{tri}} \left( \frac{L}{\zeta_{\parallel}} \right). \quad (94)$$

If the data for different system sizes can be collapsed using  $\beta = 1/4$ , then this provides good evidence of the presence of a Pokrovsky-Talapov tricritical point. We apply this scaling hypothesis to  $\mathcal{H}_{\text{ABB2}}$  [Eq. 58] in the constrained manifold in Fig. 21, and find that for  $\delta J = 0.7$  the data can be convincingly collapsed using  $\beta = 0.21 \pm 0.04$  and  $\zeta_{\parallel} = 0.91 \pm 0.25$ .

In a system where defect triangles are allowed, the tricritical point will be in the Ising tricritical universality class in a temperature window close to the phase transition. However, as discussed for the Ising/Pokrovsky-Talapov critical point, the Ising/Pokrovsky-Talapov tricritical point will be essentially Pokrovsky-Talapov tricritical as long as the temperature is low enough that the Ising temperature window is negligible.

For the Pokrovsky-Talapov/Ising critical point the question of what is a low enough temperature is answered by the calculation of  $T_{\text{Is}}$  [Eq. 88], and the width of the Ising temperature

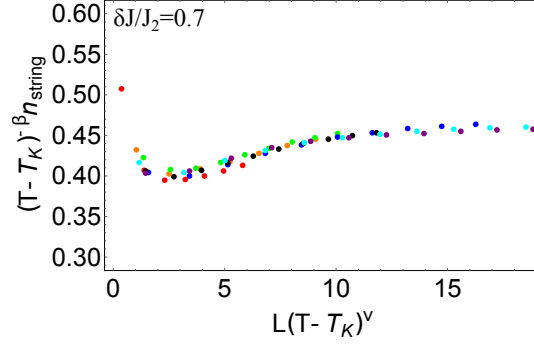


Figure 21: Data collapse demonstrating a Pokrovsky-Talapov tricritical point. The model in question is  $\mathcal{H}_{\text{ABB2}}$  [Eq. 58] in the constrained manifold and  $\delta J/J_2 = 0.7$ . Simulations are run on hexagonal clusters with  $N = 3L^2$  and  $L = 24$  (red),  $L = 36$  (orange),  $L = 48$  (green),  $L = 72$  (blue),  $L = 96$  (black),  $L = 144$  (cyan),  $L = 192$  (purple). The data are plotted according to the scaling hypothesis given in Eq. 94, and the best collapse is found for  $\beta = 0.21 \pm 0.04$  and  $\nu_{\parallel} = 0.91 \pm 0.25$ . This is consistent with  $\beta = 1/4$ , which is the expected value at a Pokrovsky-Talapov tricritical point.

window is given by  $T_{\text{Is}} - T_c \propto \exp[-E_{\text{def}}/T]/b$ . Approaching the tricritical point  $b \rightarrow 0$  and this results in a divergence of the Ising temperature window. Of course the temperature window doesn't truly diverge, but is cut-off by the fourth order term in  $\omega_q$  [Eq. 90]. However, this will typically result in the Ising temperature window being considerably broader close to the tricritical point than it would be at comparable temperatures for a critical point.

The width of the Ising temperature window at the tricritical point can be calculated by considering the 1D quantum Hamiltonian  $H_{1\text{D}}$  given in Eq. 84 with,

$$A_q = a(T_{\text{K}} - T) + cq^4 + \dots, \quad B_q = 4qe^{-\frac{E_{\text{def}}}{2T}} + \dots \quad (95)$$

This gives,

$$T_{\text{Is}} = T_{\text{K}} + \frac{6}{ac^{\frac{1}{3}}} e^{-\frac{2E_{\text{def}}}{3T}}. \quad (96)$$

While the value of  $T_{\text{Is}}$  could be modified by inclusion of extra terms in  $B_q$ , the main point is to show that the temperature window for tricritical Ising behaviour is significantly greater than that for critical Ising behaviour (see Eq. 88).

In the case of a significant tricritical Ising temperature window, the expected order parameter and correlation length behave as  $m_{\text{stripe}} \sim (T_c - T)^{1/4}$  and  $\xi_{\text{Is}} \sim |T - T_c|^{-1}$  and therefore  $\beta = 1/4$  and  $\nu = 1$ . This can be tested for in simulations by considering the scaling hypothesis given in Eq. 89.

#### 5.4 Pokrovsky-Talapov first-order transition

Finally we turn to a phenomenological theory of a first-order transition. Unlike for the Pokrovsky-Talapov and Pokrovsky-Talapov-tricritical phenomenological theories (Section 5.1 and Section 5.3), it is not clear that a free-fermion model is applicable, since attractive interactions between strings lead to a qualitatively different situation with non-vanishing string density at the transition (see Section 4.3.5). However, we argue that it is possible to construct an effective free-fermion model by enforcing that the dispersion should have lines of zeros at the transition temperature.

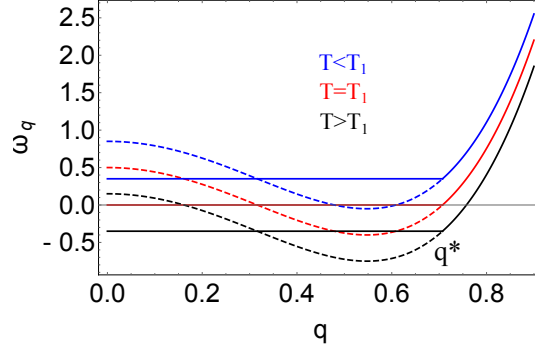


Figure 22: The dispersion,  $\omega_q$  [Eq. 101], of fermions close to a first-order phase transition. The dispersion  $\omega'_q$  [Eq. 100] (shown dashed) contains a number of features that are not consistent with a first-order phase transition. A simple way to fix this is to make a construction where  $\omega'_q$  is replaced by  $\omega'_q$  in the region  $0 < q < q^*$ , where  $q^*$  is given in Eq. 102 (shown with solid line). This results in an  $\omega_q$  having a line of zeros at the transition temperature  $T = T_1$  [Eq. 98], and this is consistent with a discontinuous jump in  $n_{\text{string}}$ .

We consider the constrained manifold of configurations where strings are forced to wind the system, and therefore the fermions are well defined particles with infinite lifetimes. In consequence the effective Hamiltonian has the form given in Eq. 78. In order to determine  $\omega_q$  one can first posit the simplest free energy consistent with  $F_{\text{PT}}$  [Eq. 82] and  $F_{\text{tri}}$  [Eq. 93], which is given by,

$$F_1 = a(T_K - T)n_{\text{string}} + \frac{b\pi^2}{3}n_{\text{string}}^3 + \frac{c\pi^4}{5}n_{\text{string}}^5 + \dots \quad (97)$$

where  $a > 0$ ,  $b < 0$  and  $c > 0$  and the negative sign in front of the cubic term describes a string-string attraction.

Analysis of  $F_1$  [Eq. 97] shows that there is a first-order phase transition for,

$$T_1 = T_K - \frac{5b^2}{36ac}, \quad (98)$$

and the density of strings jumps discontinuously from  $n_{\text{string}} = 0$  to  $n_{\text{string}} = \sqrt{-5b/(6\pi^2c)}$  at this temperature. As expected from Monte Carlo simulations (see Section 4.3.3) the first-order transition occurs at a lower temperature than the putative second-order transition, and this difference is related to the binding energy between strings. As  $b \rightarrow 0$  it can be seen that the size of the jump in  $n_{\text{string}}$  also goes to 0, and a second-order phase transition is recovered. In general the string density is given by,

$$n_{\text{string}} = \begin{cases} 0 & T < T_1 \\ \frac{1}{\pi} \sqrt{\frac{-3b + 2\sqrt{b^2 + 9ac(T - T_1)}}{6c}} & T > T_1 \end{cases} \quad (99)$$

A naive guess for a fermion dispersion relation that is consistent with  $F_1$  [Eq. 97] is given by,

$$\omega'_q = a(T_K - T) + bq^2 + cq^4 + \dots \quad (100)$$

However, it can be seen in Fig. 22 that this has a number of non-physical features. It predicts a phase transition at  $T = T_K - b^2/(4ac) \neq T_1$  and, even worse, there is no discontinuous

jump in  $n_{\text{string}}$  and the transition is second order. In order to fix this theory we make the construction shown in Fig. 22, and given mathematically by,

$$\omega_q = \begin{cases} \omega'_{q^*} & q < q^* \\ \omega'_q & q > q^* \end{cases} \quad (101)$$

where  $q^*$  is defined by,

$$\frac{q^*}{\pi} = n_{\text{string}}(T_1) = \frac{1}{\pi} \sqrt{\frac{-5b}{6c}}. \quad (102)$$

As a result the theory predicts a first-order transition at  $T = T_1$  and  $n_{\text{string}}$  is given by Eq. 99 as required.

This construction enforces a line of zeros in  $\omega_{\mathbf{q}}$  at the transition, and this can be justified in two ways. Firstly, in the absence of defect triangles, the fermions are infinitely long-lived particles, and the absence of decay processes means that the dispersion should be sharp (i.e. there is no imaginary part to the self energy). The only way in which a sharp fermion dispersion can be consistent with a discontinuous jump in the fermion density is by having a line of zeros for some range of  $\mathbf{q}$  values exactly at the transition.

The second justification comes from the perturbative solution to the  $J_1$ - $J_2$  Ising model developed in Section 4.3.2. The infinite lifetime of the fermions is reflected in the absence of anomalous Green's functions for the Grassmann variables, and the spectrum  $\tilde{\epsilon}_{\mathbf{k}}$  [see Eq. 69] can therefore be related to that of  $\omega_{\mathbf{q}}$  by an equivalent calculation to that given in Appendix C. The first-order, perturbative calculation of  $\tilde{\epsilon}_{\mathbf{k}}$  given in Section 4.3.2 suggests that  $\tilde{\epsilon}_{\mathbf{k}}$  has a line of zeros at the transition temperature, though it should be noted that a true line of zeros would only appear in infinite order perturbation theory. If  $\tilde{\epsilon}_{\mathbf{k}}$  has a line of zeros at the transition temperature, then it follows that  $\omega_{\mathbf{q}}$  should also have a line of zeros at the transition.

Taking all the results of this section together, one can see that with relatively few parameters, it is possible to understand the full gamut of critical behaviour in the dipolar TLIAF. The important parameters are the reduced temperature,  $(T - T_K)/T_K$ , which changes sign at a second-order phase transition, the distortion-dependent parameter  $b$ , which changes sign at the tricritical point, and the ratio  $E_{\text{def}}/T_K$ , which determines the temperature window of Ising criticality at the transition. Of course it is also necessary to include the parameter  $c$  in order to ensure that the free energy is bounded from below. In the following section the phenomenological theory will be used to analyse the dipolar TLIAF.

## 6 Universality and correlation in the Dipolar TLIAF

Finally we return to the dipolar TLIAF, armed with the results of Section 4 and Section 5. The intuition gained from the study of toy models and the development of a phenomenological theory make it possible to perform a more detailed analysis of  $\mathcal{H}_{\text{dip}}$  [Eq. 1], concentrating in particular on the universality classes of the phase transitions and the nature of the correlations.

### 6.1 Universality of phase transitions

First we look in more detail at how the universality class of the phase transition evolves with  $\delta$ , and this is summarised in the phase diagram shown in Fig. 23.

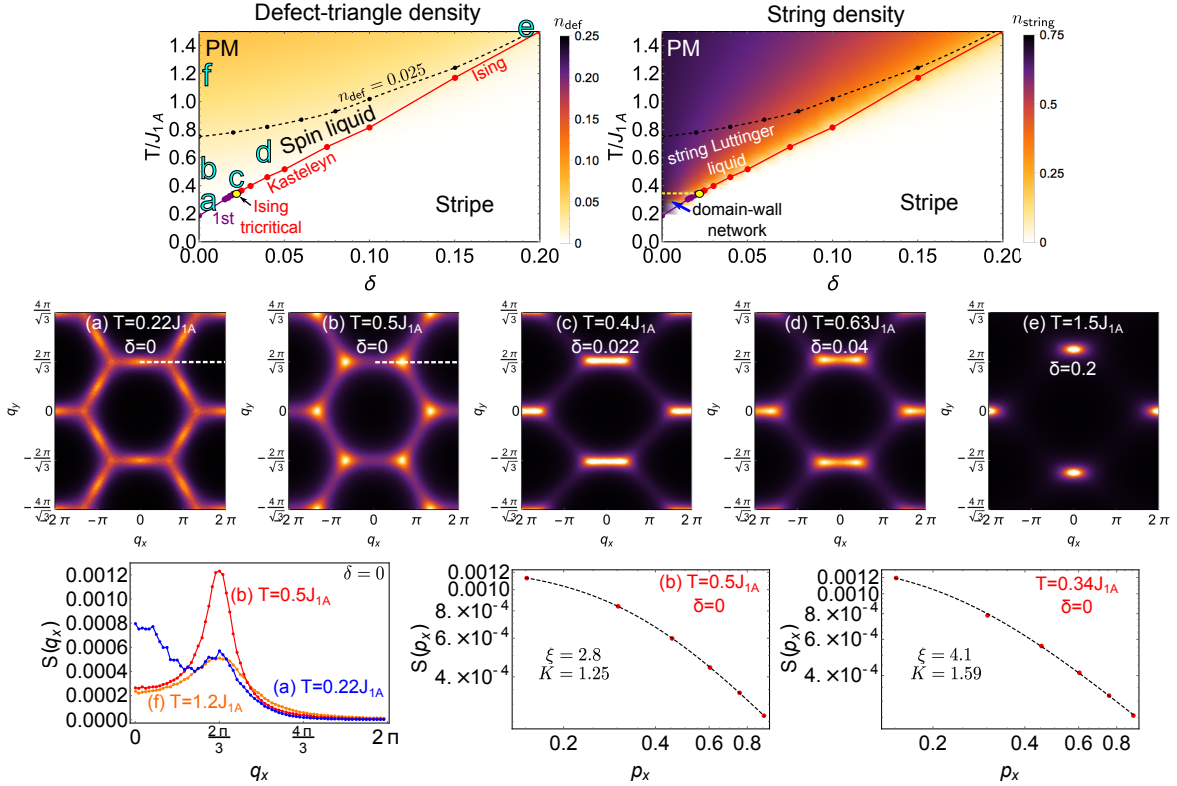


Figure 23: The phase diagram and structure factor of  $\mathcal{H}_{\text{dip}}$  [Eq. 1], as revealed by Monte Carlo simulations. (Top) Phase diagrams showing stripe-ordered, spin-liquid and paramagnetic phases, as well as defect-triangle density (left) and string density (right). The spin-liquid can be subdivided into a string Luttinger liquid with variable Luttinger parameter  $K$  and a domain-wall network region (right). There are four different regions of critical behaviour: first order for  $0 \leq \delta < 0.022$  (purple); Ising tricritical for  $\delta = 0.022$  (yellow dot); Pokrovsky-Talapov for  $0.022 < \delta \lesssim 0.1$  (red); and Ising for  $\delta > 0.1$  (also red). (Middle) Structure factor  $S(\mathbf{q})$  [Eq. 32] calculated by Monte Carlo simulation of an  $L = 48$  hexagonal cluster. Letters correspond to those appearing on the left-hand phase diagram. (Bottom) Cuts through  $S(\mathbf{q})$  and fits to  $S(\mathbf{q} - \mathbf{q}_{\text{string}})$  using Eq. 104. (a) For  $\delta = 0$  and  $T < T_{\text{tri}}$  there is significant spectral weight around the whole perimeter of the triangular-lattice Brillouin zone, which is typical of a domain-wall network. (b) On increasing the temperature a string Luttinger liquid forms with peaks at  $\mathbf{q} = (\pm 2\pi/3, 2\pi/\sqrt{3})$ . (c) At temperatures just above the tricritical point, the structure factor shows behaviour consistent with Pokrovsky-Talapov tricritical behaviour, with lines of spectral weight associated with a quasi-degeneracy between string sectors. (d) Above a second order Kasteleyn transition the string density increases slowly with temperature, and peaks appear at  $\mathbf{q} = \pm \mathbf{q}_{\text{string}}(T, \delta) = (\pm \pi n_{\text{string}}(T, \delta), 2\pi/\sqrt{3}(1 - \delta))$ . (e) For large values of  $\delta$  the Ising temperature window becomes significant, and the critical region has peaks at the ordering vector  $\mathbf{q}_{\text{stripe}}(\delta) = (0, 2\pi/\sqrt{3}(1 - \delta))$ . (f) In the paramagnetic region the peaks become very broad, indicating a short correlation length.

For  $0 \leq \delta < 0.022$  the transition is first order. This can be seen from studying histograms of the configurational energies or string densities in the vicinity of the transition (shown in Fig. 5 for the isotropic case). These are double peaked, with a sharp, low-energy peak associated with the almost fluctuationless stripe phase and a broader high-energy peak associated with the disordered phase.

The first-order nature of the transition is also clear from simulations of the heat capacity, and the case of  $\delta = 0$  is shown in Fig. 24. Integrating  $C/T$  from infinity shows that the disordered state just above the phase transition has an entropy per site of  $S/N \approx 0.22$ . While this is less than the Wannier entropy  $S_{\text{wan}}/N = 0.323\dots$  associated with the ground state of the nearest-neighbour TLIAF [2], it is still considerable. The low-temperature stripe phase



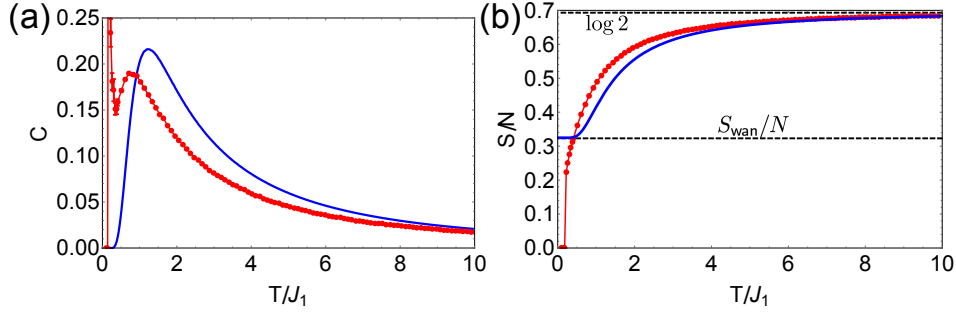


Figure 24: The heat capacity and entropy per site for  $\mathcal{H}_{\text{dip}}$  [Eq. 1] with  $\delta = 0$ . (a) The heat capacity (red) shows a broad maximum centred on  $T = 0.8J_1$ , which corresponds to the freezing out of defect triangles, and a sharp peak at  $T = 0.185J_1$  due to a first-order phase transition. This can be compared to the case of the nearest-neighbour TLIAF (blue), which shows a similar broad maximum centred on  $T = 1.2J_1$ , but no low-temperature phase transition. (b) The entropy per site (red), calculated by integrating the heat capacity from infinity. The entropy passes through  $S_{\text{wan}}/N$ , at  $T = 0.5J_1$ , but does not show an extended plateau, unlike the nearest-neighbour TLIAF (blue). At the phase transition there is an entropy jump of  $\Delta S/N \approx 0.22$ .

has  $S/N = 0$ , and therefore there is a significant entropy release in the first-order transition. As  $\delta$  is increased, the entropy release at the transition decreases, and the transition becomes more weakly first order.

The first-order transition turns into a second-order transition at a tricritical point, and this is located at  $\delta = 0.022$  and  $T = T_{\text{tri}} = 0.343$ . At this point the Ising order parameter,  $m_{\text{stripe}}$  [Eq. 5], shows a convincing data collapse with 2D-Ising tricritical exponents, and this is shown in Fig. 25. It is at first sight surprising that the tricritical behaviour should be in the Ising-tricritical and not the Pokrovsky-Talapov-tricritical universality class, since the density of defect triangles is very low. However, as explained in Section 5.3, the tricritical behaviour is particularly sensitive to low densities of defect triangles, due to the disappearance of the coefficient of the quadratic term in the phenomenological dispersion relation  $\omega_q$  [Eq. 90]. Nevertheless, we will show in the next section that the correlations above the tricritical point do show characteristic features of the Pokrovsky-Talapov-tricritical point.

In the region  $0.022 < \delta \lesssim 0.1$  the phase transition is technically in the 2D Ising universality class, due to the small but finite density of defect triangles. However, the density is low enough that the Ising temperature window is negligible, and the transition is to all intents and purposes of the Kasteleyn type, with Pokrovsky-Talapov critical behaviour. This is shown in Fig. 25, where for  $\delta = 0.05$  there is a convincing data collapse for the string density,  $n_{\text{string}}$ , using Pokrovsky-Talapov critical exponents. Starting from the scaling hypothesis given in Eq. 83, one finds a good collapse for  $\beta = 0.44 \pm 0.07$  and  $\nu_{\parallel} = 0.92 \pm 0.2$ , which is consistent with the expected Pokrovsky-Talapov exponents of  $\beta = 1/2$  and  $\nu_{\parallel} = 1$ .

For  $\delta > 0.1$  the density of defect triangles at the phase transition becomes significant, and the 2D Ising nature of the transition starts to become visible in simulations. This can for example be seen in Fig. 25, where for  $\delta = 0.2$  the Ising order parameter,  $m_{\text{stripe}}$  [Eq. 5] shows a convincing collapse. For  $\delta > 0.15$  the Ising temperature window becomes large enough that there is no spin-liquid region.

## 6.2 Correlations between spins

Next we turn to the spin correlations, the nature of which can be used to attain a more detailed understanding of the phase diagram. The correlations can be probed by simulation

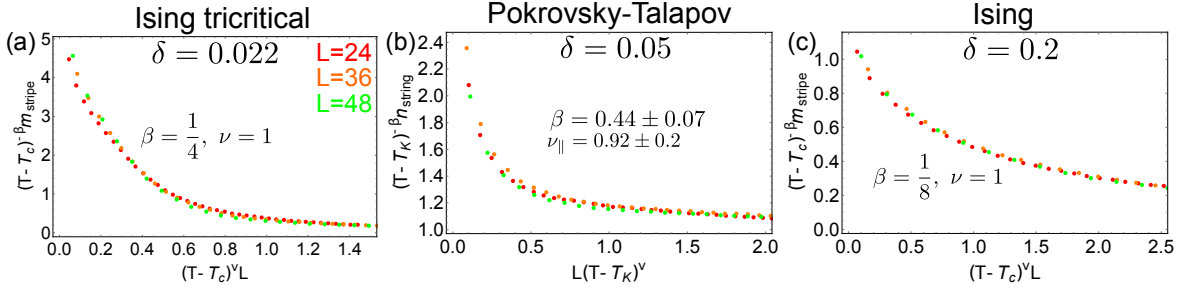


Figure 25: Data collapse close to the critical point for  $\mathcal{H}_{\text{dip}}$  [Eq. 1]. Monte Carlo simulation results are shown for  $m_{\text{stripe}}$  [Eq. 5] and  $n_{\text{string}}$  [Eq. 25] on hexagonal clusters of size  $L = 24$  (red),  $L = 36$  (orange) and  $L = 48$  (green). (a) In the tricritical region the best data collapse is found for  $m_{\text{stripe}}$  at  $\delta = 0.022$  using the scaling hypothesis given in Eq. 89 with Ising tricritical exponents  $\beta = 1/4$  and  $\nu = 1$ . (b) Data collapse at  $\delta = 0.05$  using the scaling hypothesis given in Eq. 83 for Pokrovsky-Talapov critical behaviour and for exponents that minimise the “goodness of collapse” measure proposed in [58]. This gives  $\beta = 0.44 \pm 0.07$  and  $\nu_{\parallel} = 0.92 \pm 0.2$ , which are consistent with the expected Pokrovsky-Talapov exponents  $\beta = 1/2$  and  $\nu_{\parallel} = 1$ . (c) Data collapse at  $\delta = 0.2$  using the scaling hypothesis given in Eq. 89 and the Ising critical exponents  $\beta = 1/8$  and  $\nu = 1$ .

of the structure factor,  $S(\mathbf{q})$  [Eq. 32], and this can be interpreted using the insights built up by studying toy models in Section 4.

In the stripe-ordered phase the structure factor simply shows Bragg peaks at  $\mathbf{q} = \pm \mathbf{q}_{\text{stripe}}(\delta) = (0, 2\pi/\sqrt{3}(1 - \delta))$ . At low temperatures ( $T \ll J_1$ ) fluctuations around the stripe-ordered ground state are almost completely absent and all the weight is in the Bragg peak. At higher temperatures ( $T \sim J_1$ ) the creation of defect triangles becomes energetically viable, and a small amount of spectral weight is redistributed from the Bragg peak, resulting in some diffuse scattering. This only occurs for  $\delta \gtrsim 0.1$ , since for  $\delta < 0.1$  the transition temperature is sufficiently smaller than  $J_1$  that the density of defect triangles is highly suppressed even close to the critical point.

More interesting is the disordered phase, which shows very different behaviour depending on the value of  $\delta$  and  $T$ . This is shown in Fig. 23 where the disordered phase is divided into a weakly-correlated paramagnet and strongly-correlated spin liquid, which is further subdivided into a string Luttinger liquid and a domain-wall-network state.

The spin-liquid region is characterised by a set of strings that mostly wind the system (see Fig. 26), and, since defect triangles act as sources and sinks of strings, this is synonymous with a low density of defect triangles. In consequence, we somewhat arbitrarily designate the crossover between the spin-liquid and paramagnetic regions to be at  $n_{\text{def}} = 0.025$  (10% of the saturation value). The high string tension also results in significant correlation between spins separated by many lattice spacings. Within the spin-liquid region the qualitative behaviour is determined by interactions between the strings, which can be repulsive or attractive depending on the balance between an entropic repulsion due to the non-crossing constraint and an energetic attraction due to the further-neighbour  $J$ -couplings. When the repulsive interaction dominates, the strings avoid one another on average, and this results in the formation of a string Luttinger liquid. When the attractive interaction dominates the strings remain fluctuating but loosely bind together, forming a domain-wall-network state (see Fig. 26).

In contrast to the spin liquid, the paramagnetic region has a high density of defect triangles and the strings mostly form short closed loops or longer floppy loops with many reversals (see Fig. 26). In consequence the correlation length is very short.

It is useful to discuss each of these qualitatively different regions in more detail, and

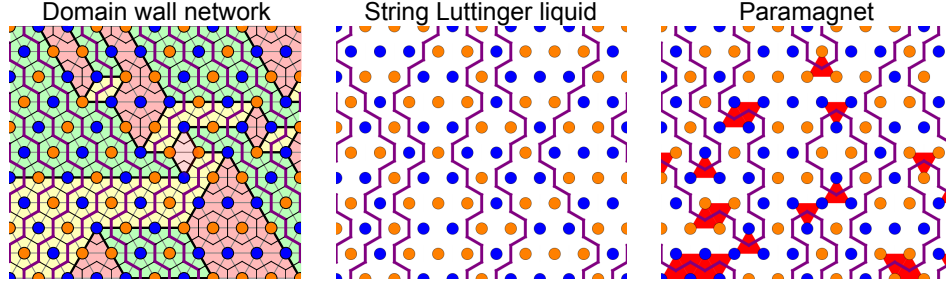


Figure 26: Typical string configurations in the domain-wall-network, string-Luttinger-liquid and paramagnetic regions (see Fig. 23). In the domain-wall-network region strings typically wind the system and attractive string-string interactions cause them to bind together. In the string-Luttinger-liquid region the strings also tend to wind the system, but repulsive interactions result in a grill-like superstructure with strings avoiding one another as far as possible. In the paramagnet there are many defect triangles that act as sources and sinks of pairs of strings, resulting in the strings being floppy and forming short closed loops.

first we turn to the string Luttinger liquid. Since the strings repel one another they form a grill-like superstructure where the average spacing between the strings depends on the string density,  $n_{\text{string}}(T, \delta)$ . In consequence we expect the structure factor,  $S(\mathbf{q})$ , to be peaked at  $\mathbf{q} = \pm \mathbf{q}_{\text{string}}(T, \delta) = (\pm \pi n_{\text{string}}(T, \delta), 2\pi/\sqrt{3}(1-\delta))$ . However, the presence of a low density of defect triangles means that the peaks do not have an algebraic structure but an exponential decay of correlations in real space. In analogy with Section 4.2 and Section 4.3 we make the ansatz that the spin correlations follow the asymptotic form,

$$S(\mathbf{r}) \propto \frac{\cos[\mathbf{q}_{\text{string}} \cdot \mathbf{r}] e^{-\frac{r_x}{\xi_{\perp}}} e^{-\frac{r_y}{\xi_{\parallel}}}}{|\mathbf{r}|^{\frac{K}{2}}}, \quad (103)$$

where  $\xi_{\perp}$  and  $\xi_{\parallel}$  are correlation lengths in the directions perpendicular and parallel to the strings. In the isotropic case ( $\delta = 0$ ) one expects  $\xi_{\perp} = \xi_{\parallel}$ , while for the anisotropic case ( $\delta \neq 0$ )  $\xi_{\perp} \neq \xi_{\parallel}$ . We refer to  $K$  as the Luttinger parameter, and the name comes from interpreting the strings as the worldlines of spinless fermions, resulting in a 1D quantum model with weak fermion-fermion attraction and therefore Luttinger parameter  $K > 1$  (the non-crossing constraint that drives the entropic repulsion between strings maps onto the Pauli exclusion principle and is therefore not considered an interaction in the fermion model).

In practice simulations show that the reciprocal-space structure factor in the string-Luttinger-liquid region is dominated by peaks at  $\mathbf{q} = \mathbf{q}_{\text{string}}$ , but also has spectral weight on the line of  $\mathbf{q}$  values joining  $\mathbf{q}_{\text{string}}$  and  $-\mathbf{q}_{\text{string}}$  (see Fig. 23). In consequence it is better to fit the structure factor in reciprocal space than in real space, and Fourier transforming the asymptotic form given in Eq. 103 in the vicinity of  $\mathbf{q} = \mathbf{q}_{\text{string}}$  and for  $\xi_{\perp} = \xi_{\parallel} = \xi$  gives [59],

$$S(\mathbf{p}) \propto \frac{1}{p^{2-\frac{K}{2}}} g(p\xi), \quad (104)$$

where  $\mathbf{p} = \mathbf{q} - \mathbf{q}_{\text{string}}$ ,  $p = |\mathbf{p}|$  and,

$$g(p\xi) = 2\pi \int_0^{\infty} dx x^{1-\frac{K}{2}} e^{-\frac{x}{p\xi}} J_0(x) = 2\pi (p\xi)^{2-\frac{K}{2}} \Gamma\left(2 - \frac{K}{2}\right) {}_2F_1\left(\frac{6-K}{4}, 1 - \frac{K}{4}; 1; -(p\xi)^2\right) \quad (105)$$

where  $J_0(x)$  is the Bessel function of the first kind,  $\Gamma(x)$  is the Euler Gamma function and  ${}_2F_1(a, b; c; z)$  is the hypergeometric function. The result of fitting this to simulations for  $\delta = 0$  and various  $T$  is shown in Fig. 23, and it can be seen that the Luttinger parameter takes values  $K > 1$ , as expected, and the correlation length is several lattice spacings. A more precise determination of  $K$  and  $\xi$  would require simulations on larger clusters.

For  $\delta > 0$  the string density,  $n_{\text{string}}$ , and therefore  $\mathbf{q}_{\text{string}}$  varies with temperature, and this is reflected in the position of the peaks in  $S(\mathbf{q})$  [see Fig. 23]. Above the second-order transition the string density smoothly increases with increasing temperature, as can be seen in Fig. 23, and thus the peaks move apart. It should be remembered that the asymptotic form of the correlations given in Eq. 103 is only valid above a lengthscale  $\zeta_{\parallel} \sim 1/n_{\text{string}}^2$  (see Section 4.1.4). As such, finite size effects become very important close to the second-order transition where the string density is low.

While the critical exponents close to  $(T, \delta) = (T_{\text{tri}}, \delta_{\text{tri}})$  are best fitted with 2D Ising tricritical exponents, the behaviour of the structure factor for  $T \gtrsim T_{\text{tri}}$  is approximately that of a Pokrovsky-Talapov tricritical point, suggesting that the Ising temperature window is relatively small. The structure factor shows high spectral weight over a range of  $\mathbf{q}$  values close to  $\mathbf{q} = \mathbf{q}_{\text{string}}$  (see Fig. 23) and this is due to the dispersion associated with strings becoming very flat (see Section 5.3).

In the spin-liquid region and at low temperature the energetic attraction between strings can exceed the entropic repulsion, and the strings weakly bind together forming a domain-wall-network state (pictured in Fig. 19 and Fig. 26). It makes intuitive sense that the crossover from a string Luttinger liquid to a domain-wall network occurs at  $T \approx T_{\text{tri}}$ , since this is the temperature at which the cubic term in the free energy changes sign, signifying a change from repulsive to attractive interactions (see Section 5). A simple way to test that this is the case is to perform simulations in a highly restricted manifold of Ising configurations containing two strings, each of which winds the system. The average separation of the strings (defined in Eq. 76) shows a change at  $T \approx T_{\text{tri}}$  indicating a shift from repulsive to attractive interactions (see Fig. 27). We find that the temperature at which this change occurs is essentially independent of  $\delta$  in the relevant region ( $0 < \delta < \delta_{\text{tri}}$ ), and therefore draw a straight crossover line in Fig. 23.

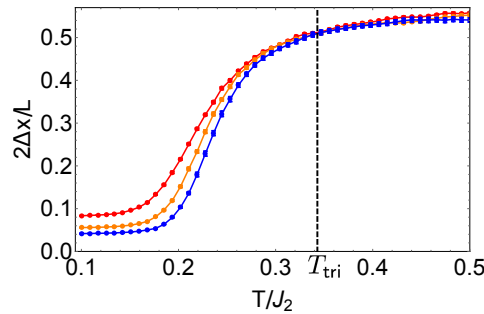


Figure 27: The average separation of a pair of strings,  $2\Delta x/L$  [Eq. 76]. Monte Carlo simulations are carried out at  $\delta = 0.02$  and in a reduced manifold of Ising configurations, constrained to have exactly two strings and no defect triangles. The simulations use a square cluster with linear sizes  $L = 24$  (red),  $L = 36$  (orange) and  $L = 48$  (blue). At low temperature the strings bind together while at higher temperatures the strings repel one another. The dashed line shows the temperature of the tricritical point,  $T_{\text{tri}}$ .

At the crossover between the string Luttinger liquid and domain-wall-network regions the structure factor undergoes a redistribution of weight, with the peaks at  $\mathbf{q} = \pm \mathbf{q}_{\text{string}}$  becoming

less prominent and weight shifting to the perimeter of the triangular lattice Brillouin zone (see Fig. 23). As the temperature is lowered weight starts to build up at  $\mathbf{q} = \mathbf{q}_{\text{stripe}}$ , but there is a first-order phase transition to the stripe phase before the peaks can become very prominent. By changing the ratio of the further-neighbour couplings it is theoretically possible to create domain-wall-networks with larger domains, resulting in sharper peaks at  $\mathbf{q} = \mathbf{q}_{\text{stripe}}$  [11].

In the paramagnetic region the strings form short closed loops or longer floppy loops and the density of defect triangles is high. There is an exponential decay of spin correlations with short correlation length, leading to broad peaks in  $S(\mathbf{q})$  that are no longer located at  $\mathbf{q} = \mathbf{q}_{\text{string}}$ . For  $\delta \gtrsim 0.15$  the structure factor shows the standard behaviour associated with a second-order phase transition in the 2D Ising universality class, with spectral weight building up at the ordering vector  $\mathbf{q} = \mathbf{q}_{\text{stripe}}$  and the associated correlation length diverging as the critical temperature is approached.

## 7 Discussion and Conclusion

We have shown throughout this article that the dipolar TLIAF shows a wide variety of behaviour, with stripe-ordered, spin-liquid and paramagnetic phases. The nature of this spin-liquid region can be tuned by temperature between a “strongly-coupled” domain-wall network and a “weakly-coupled” string Luttinger liquid, where the strength of the coupling refers to a mapping to a 1D fermionic model. The addition of a small anisotropy allows the nature of the spin liquid to be further tuned, and this in turn changes the critical behaviour from first order to Kasteleyn-like, via a tricritical point with mixed tricritical-Ising and tricritical-Pokrovsky-Talapov characteristics.

Here we take a step back and discuss the general features of TLIAF models with monotonically decreasing further-neighbour interactions. We have argued throughout that the most intuitive way to understand such models is by considering the string degrees of freedom, which can be thought of either in their 2D classical incarnation or as the worldlines of spinless fermions in 1D (see Fig. 26 for pictures of typical string configurations). As such we would like to determine which energy scales present in a given microscopic model dictate the behaviour of the strings and therefore the form of the phase diagram and the physical observables.

In general TLIAF models can have a plethora of competing couplings, as is clearly true in the dipolar case. Our claim is that these can in most cases be distilled into four important energy scales (it is worth noting that other energy scales can become important if the further-neighbour interactions are not monotonically decreasing interactions [10, 11]). The first and most important is the isotropic part of the nearest-neighbour interaction; that is the part of the nearest-neighbour interaction that does not vary with the anisotropy (i.e. is independent of  $\delta$  in the dipolar case). This has been labelled as  $J_{1A}$  throughout the article and used as the reference energy scale.  $J_{1A}$  approximately sets the energy cost of creating defect triangles, and therefore “interesting”, strongly-correlated physics only occurs in the region  $T < J_{1A}$ .

Next are two energy scales that combine the isotropic parts of all the further-neighbour couplings. The first of these,  $J_{\text{fn}}$ , is a measure both of the internal energy of a string and also of the string-string interactions. As an example, for the TLIAF with  $J_1$ ,  $J_2$  and  $J_3$  couplings it is given by  $J_{\text{fn}} = J_2 - 2J_3$  [10]. This shows that even if the further-neighbour couplings are comparable with  $J_1$ , their combined effect can still be small due to frustration. The second energy scale is  $J_c$ , and this is related to the energy cost associated with a string changing

direction. In the case of the  $J_1$ - $J_2$ - $J_3$  model this is given by  $J_c = J_2$ , and it can therefore be seen that while it can be comparable to  $J_{\text{fn}}$  it doesn't have to be. One thing that is important to note is that we always consider  $J_{\text{fn}}, J_c > 0$ , and if this is not the case different physics can be expected [11].

The final energy scale we consider is a measure of the anisotropy and is labelled  $J_{\text{an}}$ . For the dipolar TLIAF it clearly depends on  $\delta$ , and a rough estimate is given by the difference in the nearest-neighbour interaction strengths, resulting in,

$$J_{\text{an}}(\delta) \approx J_{1\text{B}} - J_{1\text{A}} = \frac{9\delta}{4} J_{1\text{A}} + \mathcal{O}(\delta^2). \quad (106)$$

The energy scales  $J_{1\text{A}}$ ,  $J_{\text{fn}}$ ,  $J_c$  and  $J_{\text{an}}$  have been constructed with the string degrees of freedom in mind, and we now make the link more explicit. We concentrate in particular on  $J_{1\text{A}} \gg J_{\text{fn}}, J_{\text{an}}$ , which is the requirement for the existence of spin liquid behaviour.

A particularly important quantity is the internal free energy per unit length of an isolated string, which depends on  $J_{\text{fn}}$ ,  $J_c$  and  $J_{\text{an}}$ , and is approximately given by [10, 27],

$$f_{\text{string}}(T) \approx 2J_{\text{an}} + 4J_{\text{fn}} - T \log \left[ 1 + e^{-\frac{2J_c}{T}} \right]. \quad (107)$$

If string-string interactions are ignored, strings will be present in the system above a temperature  $T_{\text{string}}$ , and this is approximately given by,

$$T_{\text{string}} \approx \frac{2J_{\text{an}} + 4J_{\text{fn}} + J_c}{\log 2}. \quad (108)$$

While a number of approximations have been made in order to arrive at this simple expression, except in the extreme case of  $J_c \gg J_{\text{fn}}$ , it matches well to Monte Carlo simulations of simple models [11].

In reality the strings are not isolated, and the transition temperature and the nature of the correlations in the spin liquid depend on the string-string interactions. These have two main contributions, the first of which is an entropically-driven repulsion associated with the no-crossing constraint, and in the fermion language this maps onto the Pauli exclusion principle. The second is an energetically-driven attraction due to the further-neighbour interactions, which is approximately measured by  $J_{\text{fn}}$ , and in the fermion language it is only this second contribution that counts as an interaction.

If the attractive interaction dominates in the vicinity of  $T = T_{\text{string}}$  then an array of strings can lower their energy by binding together, and this binding energy results in a first-order transition with  $T_1 < T_{\text{string}}$ . As a result the string density jumps at the transition from  $n_{\text{string}} \approx 0$  to a finite value. At temperatures just above the transition the string-string interactions remain attractive and the strings loosely bind together, forming a domain-wall-network state. The domain-wall-network state also relies on a positive  $J_c$  which penalises changes in direction of the strings. The larger the value of  $J_c$  and  $J_{\text{fn}}$  relative to  $T$ , the larger the domain size will be. The dominance of attractive interactions in the string picture corresponds to the strong-coupling regime of the fermionic model.

When  $T \gg J_{\text{fn}}$  the entropically-driven repulsion between strings dominates over the energetically-driven attraction. If  $T_{\text{string}} \gg J_{\text{fn}}$  then the strings repel one another in the critical region, resulting in a second-order transition at  $T = T_{\text{string}}$ . As long as  $J_{1\text{A}} \gg T_{\text{string}}$  then this transition is essentially of the Kasteleyn type, since it is driven by the sudden appearance of strings that mostly wind the system. This type of phase transition is quite different from the more usual Ising transition which is driven by the proliferation of local defects.



Above the second-order transition the string density,  $n_{\text{string}}$ , slowly increases with increasing temperature, and, while the strings fluctuate, they on average form an equally-spaced, grill-like structure due to their mutual repulsion. In the fermionic language this corresponds to weak coupling and a 2D classical equivalent of a Luttinger liquid forms.

At temperatures at which the attractive and repulsive interactions balance the phase transition is tricritical, and this occurs when  $J_{\text{an}} \approx J_{\text{fn}}$ . Just above the transition the string or fermion dispersions are soft, resulting in large fluctuations in the string/fermion density.

The crossover between the spin liquid and paramagnet occurs at  $T \approx J_{1A}$  and at this temperature defect triangles become common. As a result strings form short closed or longer floppy loops which typically don't wind the system. If  $T_{\text{string}} \approx J_{1A}$ , then the transition is in the Ising universality class and is driven by the proliferation and growth of local defects, resulting in a direct transition from the ordered phase to the weakly-correlated paramagnet. In the dipolar TLIAF this occurs for  $\delta \gtrsim 0.15$ .

For the dipolar TLIAF it is possible to approximately determine the appropriate energy scales as  $J_{\text{fn}} \approx 0.02J_{1A}$ ,  $J_{\text{an}} \approx 9\delta J_{1A}/4$  and  $J_{\text{c}} \approx 0.08J_{1A}$ . Here  $J_{\text{c}}$  is determined as half the energy cost of an isolated corner, while  $J_{\text{fn}}$  is determined so as to be consistent both with  $T_{\text{string}}$  [Eq. 108] and with Monte-Carlo, worm-update simulations, which are found to work best with approximately this value of  $J_2^{\text{worm}} - 2J_3^{\text{worm}}$  (see Section 3). Despite the slowly decreasing nature of the dipolar interaction with distance, it can be seen that frustration leads to a value of  $J_{\text{fn}}$  that is considerably smaller than  $J_{1A}$ .

An obvious question raised by this analysis is how to further reduce the value of  $J_{\text{fn}}$  and  $J_{\text{c}}$  relative to  $J_{1A}$ , since this would increase the size of the spin-liquid region and give a cleaner realisation of the Kasteleyn transition. One possibility would be to find systems with local interactions such that  $J_1 \gg J_2, J_3 \dots$ , but we are not currently aware of any such systems. A more realistic option is to change the nature of the long-range interaction such that  $J_{ij} \propto |\mathbf{r}_i - \mathbf{r}_j|^{-a}$ , where  $a = 3$  corresponds to the dipolar case. The possibility of changing  $a$  has been realised experimentally using trapped ions that naturally form a triangular lattice, and  $a$  was found to be tuneable in the range  $0 < a < 3$  [26]. Estimating the relationship between  $J_{\text{fn}}$ ,  $J_{\text{c}}$  and  $a$  is complicated, due to the competition between the further-neighbour interactions, but it seems most likely that suppression of  $J_{\text{fn}}$  would require the further-neighbour interactions to fall off faster than in the dipolar case, and therefore  $a > 3$ .

Another possibility is to add a small transverse magnetic field. This would tend to act in opposition to the further-neighbour interactions, since quantum fluctuations favour nearest-neighbour-flippable configurations of Ising spins, while the stripe configuration is maximally unflippable. Therefore a transverse field would be likely to reduce the critical temperature by suppressing  $J_{\text{fn}}$ .

Finally it is worth mentioning a number of potential extensions of this work. While we have studied the equilibrium physics of the dipolar TLIAF, this proved difficult at  $\delta = 0$  due to the inefficiency of local Monte Carlo update schemes in simulating the system. In real systems the underlying dynamics is unlikely to be as carefully tuned as is possible in simulations, and therefore it seems likely that the system will freeze at  $T \approx T_1$ , rather than finding the long-range stripe-ordered phase. This was found to be the case in preliminary simulations where we used a local update scheme in combination with a slow cooling rate. As such an apparently glassy state forms at low temperature even in the absence of disorder, realising a very slowly fluctuating domain-wall network.

A second possible extension is suggested by the mapping onto a 1D quantum model. For



$T > T_{\text{tri}}$  the dipolar TLIAF realises a slightly perturbed version of the Kitaev model of 1D spinless fermions with p-wave superconducting pairing, which is most famous for the existence of Majorana edge modes [51]. Since the disordered classical phase maps onto the topologically non-trivial fermionic phase, it would be interesting to explore the nature of the edge modes in this phase when placed on a cylinder. However, we leave a more detailed exploration of these questions for the future.

## Acknowledgements

We benefited from very useful discussions with Sergey Korshunov at the beginning of this work. We thank Naemi Leo, Oles Sendetskyi and Laura Heyderman for discussions about artificial magnetic systems. We thank Marie Ioannou for discussions concerning the calculation of correlation functions in the Grassmann path integral approach.

**Funding information** We thank the Swiss National Science Foundation and its SINERGIA network “Mott physics beyond the Heisenberg model” for financial support.

## A Defect triangles in the dipolar TLIAF

In this appendix we construct a crude model for the density of defect triangles,  $n_{\text{def}}$ , in the low-temperature paramagnetic state of the dipolar TLIAF. The aim is to justify the use of Eq. 6, which provides a simple functional form for  $n_{\text{def}}$  and is found to give a good fit to the Monte Carlo simulations (see Fig. 6).

Defect triangles are constrained to occur in pairs, and can be considered to appear on top of microstates of the constrained manifold (configurations without defect triangles). We make the crude assumption that the energy cost of these defect triangles is only weakly dependent on position and has an average value  $E_{\text{def}}$ . In this approximation, the total energy due to the defect triangles is given by,

$$E = N_{\text{def}} E_{\text{def}}, \quad (109)$$

where  $N_{\text{def}}$  is the number of defect triangles and interactions between defect triangles have been ignored.

The number of ways  $N_{\text{def}}$  defect triangles can be placed in the system with  $N_{\text{plq}}$  triangular plaquettes is simply given by the binomial coefficient, and therefore the associated partition function is,

$$\begin{aligned} \mathcal{Z}_{\text{def}} &= \sum_{N_{\text{def}}=0,2,4,\dots}^{N_{\text{plq}}} \frac{N_{\text{plq}}!}{N_{\text{def}}!(N_{\text{plq}} - N_{\text{def}})!} e^{-\beta E_{\text{def}} N_{\text{def}}} \\ &= \frac{1}{2} \sum_{N_{\text{def}}=0}^{N_{\text{plq}}} [1 + (-1)^{N_{\text{def}}}] \frac{N_{\text{plq}}!}{N_{\text{def}}!(N_{\text{plq}} - N_{\text{def}})!} e^{-\beta E_{\text{def}} N_{\text{def}}} \\ &= \frac{1}{2} \left[ \left(1 + e^{-\beta E_{\text{def}}}\right)^{N_{\text{plq}}} + \left(1 - e^{-\beta E_{\text{def}}}\right)^{N_{\text{plq}}} \right], \end{aligned} \quad (110)$$

where  $\beta = 1/T$ . In the thermodynamic limit only the first term is significant and,

$$\mathcal{Z}_{\text{def}} \approx \frac{1}{2} \left(1 + e^{-\beta E_{\text{def}}}\right)^{N_{\text{plq}}}. \quad (111)$$

The average number of defect triangles is given by,

$$\langle N_{\text{def}} \rangle = -\frac{1}{\beta} \frac{\partial \log \mathcal{Z}_{\text{def}}}{\partial E_{\text{def}}} = \frac{N_{\text{plq}} e^{-\beta E_{\text{def}}}}{1 + e^{-\beta E_{\text{def}}}} \quad (112)$$

and therefore at temperatures  $T \ll E_{\text{def}}$ ,

$$\langle N_{\text{def}} \rangle \approx N_{\text{plq}} e^{-\beta E_{\text{def}}}. \quad (113)$$

While the above analysis is clearly highly simplified with respect to the true situation in the dipolar TLIAF, it suggests that at low temperature one should expect the density of defect triangles to obey the relationship,

$$n_{\text{def}} \approx n_{\text{def}} = \frac{A e^{-\beta E_{\text{def}}}}{1 + e^{-\beta E_{\text{def}}}}, \quad (114)$$

with  $A$  and  $E_{\text{def}}$  fitting parameters. The result of fitting this to Monte Carlo simulations is shown in Fig. 6, and we find  $E_{\text{def}} = 1.57J_1$  in the isotropic, dipolar TLIAF. This can be compared with the nearest-neighbour TLIAF, where the energy cost per defect triangle is  $2J_1$ .

## B The spin-spin correlation function for the nearest-neighbour TLIAF

Here we show how to calculate the real-space, spin-spin correlation function for the nearest-neighbour TLIAF, working in both the constrained manifold (see Section 4.1) and the full, unconstrained manifold (see Section 4.2.4). Integral expressions for the correlation function can be derived in the thermodynamic limit, and numerical evaluation results in exact results up to to numerical error.

The correlation function at a given spin-spin separation can be expressed as the determinant of a Toeplitz matrix, with the matrix elements given by integrals over the Brillouin zone. The use of Toeplitz matrices in this problem was pioneered in [4, 5]. We include the calculations here, since the Grassmann path integral technique considerably simplifies the construction of the matrices [45], and also in order to generalise the calculations to include  $\delta J \neq 0$ .

In this Appendix we show the mechanical steps used to calculate the correlation functions, while the main text contains a physical discussion of the results.

The spin-spin correlation function is given by,

$$S(\mathbf{r}_j - \mathbf{r}_i) = \langle \sigma_i \sigma_j \rangle, \quad (115)$$

and we consider separation vectors,  $\mathbf{r} = \mathbf{r}_j - \mathbf{r}_i$ , that are either perpendicular or parallel to the average direction of the strings, labelled  $S_{\perp}(\mathbf{r})$  and  $S_{\parallel}(\mathbf{r})$  (corresponding to the  $\hat{e}_x$  and  $\hat{e}_y$  direction in Fig. 28).

## B.1 Spin-spin correlations in the constrained manifold

First we consider the nearest-neighbour TLIAF with a constrained manifold. The calculations are slightly simplified by using a unit cell that contains 2 triangular lattice sites and 4 honeycomb/brick lattice sites, as shown in Fig. 28 (as opposed to the minimal unit cell with 1 triangular and 2 honeycomb/brick sites used in Section. 4.1 of the main text). The two spins contained within the  $i$ th unit cell are labelled  $\sigma_{1,i}$  and  $\sigma_{2,i}$  and the perpendicular and parallel spin-spin correlation functions are,

$$S_{\perp}(r\hat{e}_x) = \langle \sigma_{1,i} \sigma_{1,i+\hat{e}_x} \rangle, \quad S_{\parallel}(r\hat{e}_y) = \langle \sigma_{2,i} \sigma_{2,i+\hat{e}_y} \rangle. \quad (116)$$

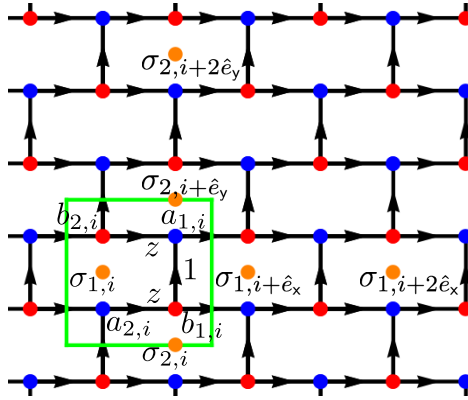


Figure 28: Brick lattice used for calculation of the nearest-neighbour TLIAF spin-spin correlation function in the constrained manifold. The (non-minimal) unit cell contains two spins,  $\sigma_{1,i}$  and  $\sigma_{2,i}$ , as well as four Grassmann variables, labelled  $a_{1,i}$ ,  $b_{1,i}$ ,  $a_{2,i}$  and  $b_{2,i}$ . Correlations between spins can be determined by studying expectation values of pairs of Grassmann variables associated with the intermediate bonds.

The unit cell also contains 4 Grassmann variables, labelled  $a_{1,i}$ ,  $b_{1,i}$ ,  $a_{2,i}$  and  $b_{2,i}$ . These can be used to determine the partition function as in Section 4.1, resulting in,

$$\mathcal{Z}_{\text{hon}} = \int \prod_i da_{1,i} db_{1,i} da_{2,i} db_{2,i} e^{\mathcal{S}_2[a_1, b_1, a_2, b_2]}, \quad (117)$$

where the action is,

$$\mathcal{S}_2[a_1, b_1, a_2, b_2] = \sum_i [b_{1,i} a_{1,i} + b_{2,i} a_{2,i+e_y} + z (a_{2,i} b_{1,i} + b_{2,i} a_{1,i} + b_{1,i} a_{2,i+e_x} + a_{1,i} b_{2,i+e_x})]. \quad (118)$$

Fourier transforming the Grassmann variables results in,

$$\mathcal{S}_2[a_1, b_1, a_2, b_2] = \sum_{\mathbf{k}} (b_{1,-\mathbf{k}}, b_{2,-\mathbf{k}}) \begin{pmatrix} e^{ik_y/2} & 2iz \sin \frac{k_x}{2} \\ 2iz \sin \frac{k_x}{2} & e^{ik_y/2} \end{pmatrix} \begin{pmatrix} a_{1,\mathbf{k}} \\ a_{2,\mathbf{k}} \end{pmatrix}, \quad (119)$$

and this is diagonalised to give,

$$\mathcal{Z}_{\text{hon}} = \prod_{\mathbf{k}} \epsilon_{\mathbf{k}}^{(4)}, \quad \epsilon_{\mathbf{k}}^{(4)} = e^{ik_y} + 2z^2(1 - \cos k_x). \quad (120)$$

### B.1.1 Correlations perpendicular to the strings

In order to calculate the spin-spin correlation function, it is necessary to express products of spins in terms of Grassmann variables. Before considering the general case, it is useful to first consider a pair of spins,  $\sigma_{1,i}$  and  $\sigma_{1,i+\hat{e}_x}$ , separated by a single honeycomb/brick lattice bond (see Fig. 28). If this bond is covered by a dimer then the spins are equivalent and  $\sigma_{1,i}\sigma_{1,i+\hat{e}_x} = 1$ , while if it is not dimer-covered  $\sigma_{1,i}\sigma_{1,i+\hat{e}_x} = -1$ . The expectation value is therefore given by,

$$\langle \sigma_{1,i}\sigma_{1,i+\hat{e}_x} \rangle = P_{b_{1,i};a_{1,i}}^{\text{dim}} - \left(1 - P_{b_{1,i};a_{1,i}}^{\text{dim}}\right) = 2P_{b_{1,i};a_{1,i}}^{\text{dim}} - 1 \quad (121)$$

where  $P_{b_{1,i};a_{1,i}}^{\text{dim}}$  is the probability of finding a dimer on the bond connecting the Grassmann variables  $b_{1,i}$  and  $a_{1,i}$ . In order to determine  $P_{b_{1,i};a_{1,i}}^{\text{dim}}$  one can calculate a reduced partition function in which the sites  $b_{1,i}$  and  $a_{1,i}$  are excluded. Exclusion of these sites effectively fixes a dimer on the bond between them, and therefore  $P_{b_{1,i};a_{1,i}}^{\text{dim}}$  is given by the ratio of the reduced partition function to the original partition function,  $\mathcal{Z}_{\text{hon}}$  [Eq. 120]. In order to exclude the two sites, it is simply necessary to place  $b_{1,i}$  and  $a_{1,i}$  inside the partition function integral, using the properties of Grassmann variables ( $a^2 = 0$ ). In consequence one finds,

$$P_{b_{1,i};a_{1,i}}^{\text{dim}} = \frac{1}{\mathcal{Z}_{\text{hon}}} \int \prod_j da_{1,j} db_{1,j} da_{2,j} db_{2,j} b_{1,i} a_{1,i} e^{\mathcal{S}_2[a_1, b_1, a_2, b_2]} = \langle b_{1,i} a_{1,i} \rangle, \quad (122)$$

and it is clear that  $P_{b_{1,i};a_{1,i}}^{\text{dim}}$  is just the thermodynamic average of  $b_{1,i} a_{1,i}$ . In consequence,

$$\langle \sigma_{1,i}\sigma_{1,i+\hat{e}_x} \rangle = \langle 2b_{1,i} a_{1,i} - 1 \rangle. \quad (123)$$

The thermodynamic average of two Grassmann variables can be calculated using,

$$\langle b_{1,i} a_{1,j} \rangle = \frac{2}{N} \sum_{\mathbf{k}} \langle b_{1,-\mathbf{k}} a_{1,\mathbf{k}} \rangle e^{i\mathbf{k}\cdot(\mathbf{r}_j - \mathbf{r}_i)} e^{ik_y/2}, \quad \langle b_{1,-\mathbf{k}} a_{1,\mathbf{k}} \rangle = \frac{e^{ik_y/2}}{\epsilon_{\mathbf{k}}^{(4)}}. \quad (124)$$

In the isotropic case ( $z = 1$ ) integration yields  $P_{b_{1,i};a_{1,i}}^{\text{dim}} = 1/3$ , as expected, and therefore  $\langle \sigma_{1,i}\sigma_{1,i+\hat{e}_x} \rangle = -1/3$ .

More generally, the correlation between a pair of spins with a separation vector parallel to  $\hat{e}_x$  is given by,

$$S_{\perp}(r\hat{e}_x) = \left\langle \prod_{l=0}^{r-1} (2b_{1,i+l\hat{e}_x} a_{1,i+l\hat{e}_x} - 1) \right\rangle. \quad (125)$$

This can be expanded using Wick's theorem, and rewritten as the determinant of an  $r \times r$ -dimensional Toeplitz matrix, resulting in,

$$S_{\perp}(r\hat{e}_x) = \det \mathbf{M}_{\perp}, \quad (126)$$

with components,

$$(\mathbf{M}_{\perp})_{mn} = 2\langle b_{1,i} a_{1,i+(n-m)\hat{e}_x} \rangle - \delta_{mn}. \quad (127)$$

In the thermodynamic limit the sum can be converted into an integral giving,

$$(\mathbf{M}_\perp)_{mn} = \frac{1}{2\pi^2} \int_{-\pi}^{\pi} dk_x e^{i(n-m)k_x} \int_{-\pi}^{\pi} dk_y \frac{e^{ik_y}}{e^{ik_y} + u} - \delta_{mn}. \quad (128)$$

where  $u = 2z^2(1 - \cos k_x)$ . The integral over  $k_y$  is given by,

$$\frac{1}{2\pi} \int_{-\pi}^{\pi} dk_y \frac{e^{ik_y}}{e^{ik_y} + u} = \begin{cases} 1 & |u| < 1 \\ 0 & |u| > 1 \end{cases}. \quad (129)$$

It follows that,

$$(\mathbf{M}_\perp)_{mn} = \frac{2 \sin [k_F(n-m)]}{\pi(n-m)} - \delta_{mn}, \quad (130)$$

where,

$$k_F = \arccos \left( 1 - \frac{1}{2z^2} \right), \quad (131)$$

is the Fermi wavevector of the quantum model  $\mathcal{H}_{1D}$  [Eq. 34]. It can be seen that  $(\mathbf{M}_\perp)_{mn} = (\mathbf{M}_\perp)_{nm}$  and thus the Toeplitz matrix is symmetric. It is also worth noting that the matrix elements could have been calculated by making use of the exact mapping onto the 1D quantum model given in Section 4.1.5.

### B.1.2 Correlations parallel to the strings

The correlation between spins parallel to  $\hat{e}_y$  can be calculated by an analogous method. The difference is that a pair of spins are separated by not one but two dimers (see Fig. 28). As such the correlation function is given by,

$$S_\parallel(r\hat{e}_y) = \left\langle \prod_{l=0}^{r-1} (2za_{2,i+l\hat{e}_y} b_{1,i+l\hat{e}_y} - 1)(2zb_{2,i+l\hat{e}_y} a_{1,i+l\hat{e}_y} - 1) \right\rangle. \quad (132)$$

where the  $z$ 's take into account the weights of the excluded dimers. Wick's theorem allows this to be rewritten as the determinant of a  $2r \times 2r$ -dimensional Toeplitz matrix,

$$S_\perp(r\hat{e}_x) = \det \mathbf{M}_\parallel, \quad (133)$$

with components,

$$\begin{aligned} (\mathbf{M}_\parallel)_{2m-1,2n-1} &= 2z \langle a_{2,i} b_{1,i+(n-m)\hat{e}_y} \rangle - \delta_{mn} \\ (\mathbf{M}_\parallel)_{2m,2n} &= 2z \langle b_{2,i} a_{1,i+(n-m)\hat{e}_y} \rangle - \delta_{mn} \\ (\mathbf{M}_\parallel)_{2m-1,2n} &= 2z \langle a_{2,i} b_{2,i+(n-m)\hat{e}_y} \rangle \\ (\mathbf{M}_\parallel)_{2m,2n-1} &= 2z \langle b_{1,i} a_{1,i+(n-m)\hat{e}_y} \rangle, \end{aligned} \quad (134)$$

where  $m, n \in \{1 \dots r\}$ . The matrix elements can be calculated from,

$$\begin{aligned}
\langle b_{1,i} a_{2,j} \rangle &= \frac{2}{N} \sum_{\mathbf{k}} \langle b_{1,-\mathbf{k}} a_{2,\mathbf{k}} \rangle e^{i\mathbf{k} \cdot (\mathbf{r}_j - \mathbf{r}_i)} e^{-ik_x/2} \\
\langle b_{2,i} a_{1,j} \rangle &= \frac{2}{N} \sum_{\mathbf{k}} \langle b_{2,-\mathbf{k}} a_{1,\mathbf{k}} \rangle e^{i\mathbf{k} \cdot (\mathbf{r}_j - \mathbf{r}_i)} e^{ik_x/2} \\
\langle b_{2,i} a_{2,j} \rangle &= \frac{2}{N} \sum_{\mathbf{k}} \langle b_{2,-\mathbf{k}} a_{2,\mathbf{k}} \rangle e^{i\mathbf{k} \cdot (\mathbf{r}_j - \mathbf{r}_i)} e^{-ik_y/2} \\
\langle b_{1,i} a_{1,j} \rangle &= \frac{2}{N} \sum_{\mathbf{k}} \langle b_{1,-\mathbf{k}} a_{1,\mathbf{k}} \rangle e^{i\mathbf{k} \cdot (\mathbf{r}_j - \mathbf{r}_i)} e^{ik_y/2},
\end{aligned} \tag{135}$$

where,

$$\begin{aligned}
\langle b_{1,-\mathbf{k}} a_{2,\mathbf{k}} \rangle &= \langle b_{2,-\mathbf{k}} a_{1,\mathbf{k}} \rangle = -\frac{2iz \sin \frac{k_x}{2}}{\epsilon_{\mathbf{k}}^{(4)}} \\
\langle b_{1,-\mathbf{k}} a_{1,\mathbf{k}} \rangle &= \langle b_{2,-\mathbf{k}} a_{2,\mathbf{k}} \rangle = \frac{e^{ik_y/2}}{\epsilon_{\mathbf{k}}^{(4)}}.
\end{aligned} \tag{136}$$

## B.2 Spin-spin correlations in the unconstrained manifold

Calculation of the spin-spin correlation function in the nearest-neighbour TLIAF with an unconstrained manifold follows a very similar pattern to that of the constrained manifold. However it is complicated by having to work with 6 or 12 Grassmann variables in the unit cell, as well as the fact that the extended brick lattice is not bipartite.

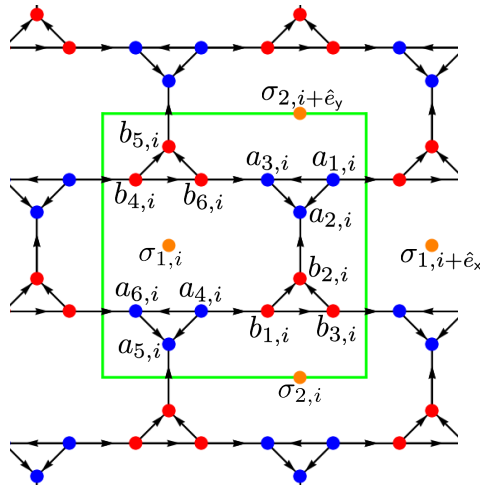


Figure 29: Extended brick lattice used for calculation of the nearest-neighbour TLIAF spin-spin correlation function in the unconstrained manifold. The (non-minimal) unit cell contains two spins,  $\sigma_{1,i}$  and  $\sigma_{2,i}$ , as well as twelve Grassmann variables, labelled  $a_1 \dots a_6$  and  $b_1 \dots b_6$ . Correlations between spins can be determined by studying expectation values of pairs of Grassmann variables associated with the intermediate bonds.

The two-spin unit cell is shown in Fig. 29 and contains 12 sites of the extended brick lattice, and therefore 12 Grassmann variables, which are labelled  $a_1 \dots a_6$  and  $b_1 \dots b_6$ . The

partition function can be calculated as in the constrained case, and this results in,

$$\mathcal{Z}_{\text{exhon}} = \prod_{k_x > 0, k_y} \epsilon_{\mathbf{k}}^{(12)}, \quad (137)$$

with,

$$\begin{aligned} \epsilon_{\mathbf{k}}^{(12)} = & (1 - z_{\mathbb{B}}^4)^2 + 4(z^2 + z_{\mathbb{B}}^2)^2 + 4 \cos k_x (z_{\mathbb{B}}^2 (1 + z_{\mathbb{B}}^4) - 2z^4) \\ & + 4 \cos^2 k_x (z^2 - z_{\mathbb{B}}^2)^2 + 4z^2 (1 - z_{\mathbb{B}}^2)^2 \cos k_y (1 - \cos k_x). \end{aligned} \quad (138)$$

The spin-spin correlation function in the direction perpendicular to the strings (parallel to  $\hat{e}_x$ ) is given by,

$$S_{\perp}(r\hat{e}_x) = \left\langle \prod_{l=0}^{r-1} (2b_{2,i+l\hat{e}_x} a_{2,i+l\hat{e}_x} - 1) \right\rangle, \quad (139)$$

and as in the constrained manifold case the correlation function can be written as the determinant of an  $r \times r$ -dimensional Toeplitz matrix,  $\mathbf{M}_{\perp}$ , with matrix elements,

$$(\mathbf{M}_{\perp})_{mn} = 2\langle b_{2,i} a_{2,i+(n-m)\hat{e}_x} \rangle - \delta_{mn}. \quad (140)$$

The correlation function in the direction parallel to the strings (parallel to  $\hat{e}_y$ ) is given by,

$$S_{\parallel}(r\hat{e}_y) = \left\langle \prod_{l=0}^{r-1} (2z a_{4,i+l\hat{e}_y} b_{1,i+l\hat{e}_y} - 1)(2z b_{6,i+l\hat{e}_y} a_{3,i+l\hat{e}_y} - 1) \right\rangle, \quad (141)$$

and this can be rewritten as the determinant of a  $2r \times 2r$ -dimensional Toeplitz matrix,  $\mathbf{M}_{\parallel}$ , with matrix elements,

$$\begin{aligned} (\mathbf{M}_{\parallel})_{2m-1,2n-1} &= 2z \langle a_{4,i} b_{1,i+(n-m)\hat{e}_y} \rangle - \delta_{mn} \\ (\mathbf{M}_{\parallel})_{2m,2n} &= 2z \langle b_{6,i} a_{3,i+(n-m)\hat{e}_y} \rangle - \delta_{mn} \\ (\mathbf{M}_{\parallel})_{2m-1,2n} &= 2z \langle a_{4,i} b_{6,i+(n-m)\hat{e}_y} \rangle \\ (\mathbf{M}_{\parallel})_{2m,2n-1} &= 2z \langle b_{1,i} a_{3,i+(n-m)\hat{e}_y} \rangle \end{aligned} \quad (142)$$

The matrix elements of interest can be determined from,

$$\begin{aligned} \langle b_{2,i} a_{2,j} \rangle &= \frac{2}{N} \sum_{\mathbf{k}} \langle b_{2,-\mathbf{k}} a_{2,\mathbf{k}} \rangle e^{i\mathbf{k} \cdot (\mathbf{r}_j - \mathbf{r}_i)} e^{ik_y/4} \\ \langle b_{1,i} a_{4,j} \rangle &= \frac{2}{N} \sum_{\mathbf{k}} \langle b_{1,-\mathbf{k}} a_{4,\mathbf{k}} \rangle e^{i\mathbf{k} \cdot (\mathbf{r}_j - \mathbf{r}_i)} e^{-ik_x/4} \\ \langle b_{6,i} a_{3,j} \rangle &= \frac{2}{N} \sum_{\mathbf{k}} \langle b_{6,-\mathbf{k}} a_{3,\mathbf{k}} \rangle e^{i\mathbf{k} \cdot (\mathbf{r}_j - \mathbf{r}_i)} e^{ik_x/4} \\ \langle b_{6,i} a_{4,j} \rangle &= \frac{2}{N} \sum_{\mathbf{k}} \langle b_{6,-\mathbf{k}} a_{4,\mathbf{k}} \rangle e^{i\mathbf{k} \cdot (\mathbf{r}_j - \mathbf{r}_i)} e^{-ik_y/2} \\ \langle b_{1,i} a_{3,j} \rangle &= \frac{2}{N} \sum_{\mathbf{k}} \langle b_{1,-\mathbf{k}} a_{3,\mathbf{k}} \rangle e^{i\mathbf{k} \cdot (\mathbf{r}_j - \mathbf{r}_i)} e^{ik_y/2}, \end{aligned} \quad (143)$$





In the case of the TLIAF, the transfer matrix acts on states of strings, as shown in Fig. 30, and a translation across 4 bonds is necessary before the lattice structure repeats. These string states can be reinterpreted as the fermionic state of a 1D quantum model at a given imaginary time coordinate, and the classical partition function sum is therefore equivalent to the fermionic path integral.

While it is possible to solve the nearest-neighbour TLIAF using a transfer matrix approach [2, 3], the solution is considerably more compact using the Kasteleyn formulation expressed as a multiple integral over Grassmann variables (see Section 4). Furthermore, the Kasteleyn approach provides a good starting point for perturbative studies of more complicated models (see Section 4.3.2). As such it would be useful to know how to link the Kasteleyn action to that of the fermionic path integral.

We demonstrate below that the Kasteleyn action naturally maps onto the quantum action when written in terms of fermionic coherent states. To do this we first re-examine the classical partition function using a non-minimal, 4-site unit cell, motivated by the fact that the string states shown in Fig. 30 involve a translation across 4 sites. We then examine the coherent-state fermionic path integral, and show that the action can be brought to the same form as the Kasteleyn action by introducing and summing over extra degrees of freedom that take into account the intermediate sites present in the honeycomb/brick lattice (see Fig. 30). Finally we link the Kasteleyn spectrum to that of the quantum model.

It should be noted that the mapping could just as well have been performed in the other direction, by starting from the Kasteleyn action and performing a Gaussian integral over half of the Grassmann variables to arrive at the fermionic coherent-state path integral. While this alternative method is probably slightly more direct, we feel that the method we present makes clearer the physical link between the two.

### C.1 Kasteleyn action in 4-site basis

The procedure for determining the Kasteleyn action in terms of Grassmann variables was developed in [6] and is reviewed in Section 4. To ease the comparison with the 1D quantum model,  $\mathcal{H}_{1D}$  [Eq. 34], we here re-determine the Kasteleyn action of the nearest-neighbour TLIAF in the constrained manifold, using a 4-site unit cell and a different set of bond orientations compared to the main text.

The reason for using a 4-site cell is that it is natural to identify a string traversing 4 sites of the honeycomb/brick lattice with a single imaginary timestep in the quantum model (see Fig. 30). The bond orientations are shown in Fig. 31 and the reason they are different from those in the main text is just to simplify the mapping. They are of course chosen in accordance with Kasteleyn's theorem [29] and therefore there is no effect on the physical properties.

Referring to Fig. 31, the partition function  $\mathcal{Z}_{\text{hon}}$  [Eq. 16] can be rewritten as,

$$\mathcal{Z}_{\text{hon}} = \int \prod_i da_{1,i} db_{1,i} da_{2,i} db_{2,i} e^{\mathcal{S}_2[a_1, b_1, a_2, b_2]}, \quad (144)$$

with,

$$\mathcal{S}_2[a_1, b_1, a_2, b_2] = \sum_i -b_{1,i} a_{1,i} - b_{2,i} a_{2,i} + z(b_{1,i+e_y} a_{2,i} + b_{1,i+e_x+e_y} a_{2,i} + b_{2,i} a_{1,i} + b_{2,i-e_x} a_{1,i}), \quad (145)$$

where  $e_x$  and  $e_y$  are the translation vectors of the unit cell.

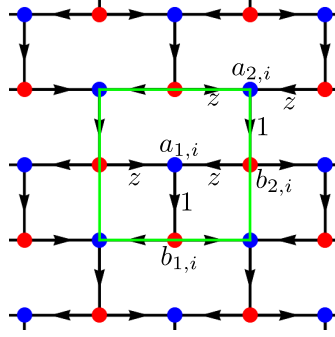


Figure 31: The set-up of the brick lattice used to map between the 2D classical model  $\mathcal{H}_{\text{ABB}}$  [Eq. 10] and the 1D quantum model  $\mathcal{H}_{\text{1D}}$  [Eq. 34]. To simplify the mapping a non-minimal, 4-site (6-bond) unit cell is chosen and the bond directions are different from in the main text. The four Grassmann variables contained within a unit cell are labelled  $a_1$ ,  $b_1$ ,  $a_2$  and  $b_2$ .

The action can be block diagonalised by Fourier transform, resulting in,

$$\mathcal{S}_2[a_1, b_1, a_2, b_2] = \sum_{\mathbf{p}} (a_{1,\mathbf{p}}, a_{2,\mathbf{p}}) \begin{pmatrix} e^{ipy/2} & -2z \cos \frac{p_x}{2} \\ -2z \cos \frac{p_x}{2} & e^{ipy/2} \end{pmatrix} \begin{pmatrix} b_{1,-\mathbf{p}} \\ b_{2,-\mathbf{p}} \end{pmatrix}. \quad (146)$$

The partition function can therefore be written as,

$$\mathcal{Z}_{\text{hon}} = \prod_{\mathbf{p}} \epsilon_{\mathbf{p}}^{\text{K}} = \prod_{\mathbf{p}} \sqrt{\epsilon_{\mathbf{p}}^{\text{K}} \epsilon_{-\mathbf{p}}^{\text{K}}} = \prod_{\mathbf{p}} |\epsilon_{\mathbf{p}}^{\text{K}}| \quad (147)$$

where the determinant of the  $2 \times 2$  matrix is,

$$\epsilon_{\mathbf{p}}^{\text{K}} = e^{ipy} - 4z^2 \cos^2 \frac{p_x}{2}, \quad (148)$$

with modulus,

$$|\epsilon_{\mathbf{p}}^{\text{K}}| = \sqrt{1 - 8z^2 \cos^2 \frac{p_x}{2} \cos py + 16z^4 \cos^4 \frac{p_x}{2}}. \quad (149)$$

## C.2 Fermionic coherent-state path integral

The Kasteleyn action can be mapped onto the fermionic, coherent-state path integral. To make the discussion self-contained, we briefly review how to construct such a path integral, following [62].

The 1D quantum model under consideration is given by,

$$\mathcal{H}_{\text{1D}} = \frac{1}{2} \sum_l \left[ -(2z^2 - 1) c_l^\dagger c_l + z^2 (c_{l+1}^\dagger c_l + c_{l-1}^\dagger c_l) \right], \quad (150)$$

where the coefficients have been chosen in anticipation of the final result. The associated partition function is,

$$\mathcal{Z}_{\text{1D}} = \sum_{\{n\}} \langle n | e^{-\beta \mathcal{H}_{\text{1D}}} | n \rangle, \quad (151)$$

where  $\{n\}$  is a complete set of states in any Hilbert-state basis, and it should be remembered that the quantum inverse temperature,  $\beta$ , is related to the periodicity of the classical model in the  $y$  direction and not to the temperature of the TLIAF.

The idea is to replace the Hilbert-state basis with that of fermionic-coherent states. These are eigenvectors of the annihilation operator,  $c_l$ , and therefore obey the eigenvalue equation,

$$c_l|\eta\rangle = \eta_l|\eta\rangle, \quad (152)$$

where  $\eta_l$  is a Grassmann variable. It follows that the coherent states are described by,

$$|\eta\rangle = \exp\left[-\sum_l \eta_l c_l^\dagger\right] |0\rangle, \quad \langle\eta| = \langle 0| \exp\left[\sum_l \bar{\eta}_l c_l\right], \quad (153)$$

where  $|0\rangle$  is the fermionic vacuum. The action of creation and annihilation operators is given by,

$$c_l|\eta\rangle = \eta_l|\eta\rangle, \quad \langle\eta|c_l^\dagger = \langle\eta|\bar{\eta}_l, \quad (154)$$

where  $\eta$  and  $\bar{\eta}$  are independent variables. The coherent states form an overcomplete basis, with overlap,

$$\langle\theta|\eta\rangle = \exp\left[\sum_l \bar{\theta}_l \eta_l\right] |0\rangle, \quad (155)$$

and the completeness relation,

$$\int \prod_l d\bar{\eta}_l d\eta_l e^{-\sum_l \bar{\eta}_l \eta_l} |\eta\rangle \langle\eta| = \mathbb{1}. \quad (156)$$

Insertion of the completeness relation into  $\mathcal{Z}_{1D}$  [Eq. 151] results in,

$$\mathcal{Z}_{1D} = \int d(\bar{\eta}_0, \eta_0) e^{-\sum_l \bar{\eta}_{l,0} \eta_{l,0}} \langle -\eta_0 | e^{-\beta\mathcal{H}} | \eta_0 \rangle, \quad (157)$$

where,

$$\langle -\eta| = \langle 0| \exp\left[-\sum_l \bar{\eta}_l c_l\right], \quad (158)$$

and

$$\int d(\bar{\eta}, \eta)_m = \int \prod_l d\bar{\eta}_{l,m} d\eta_{l,m}. \quad (159)$$

The path integral is then formed by the usual time slicing procedure to give,

$$\begin{aligned} \mathcal{Z}_{1D} &= \int \left[ \prod_m d(\bar{\eta}, \eta)_m \right] \langle -\eta_0 | e^{-\delta\tau\mathcal{H}_{1D}} | \eta_{L-1} \rangle e^{-\sum_l \bar{\eta}_{l,L-1} \eta_{l,L-1}} \\ &\quad \times \dots \\ &\quad \times \langle \eta_2 | e^{-\delta\tau\mathcal{H}_{1D}} | \eta_1 \rangle e^{-\sum_l \bar{\eta}_{l,1} \eta_{l,1}} \\ &\quad \times \langle \eta_1 | e^{-\delta\tau\mathcal{H}_{1D}} | \eta_0 \rangle e^{-\sum_l \bar{\eta}_{l,0} \eta_{l,0}} \\ &= \int \left[ \prod_m d(\bar{\eta}, \eta)_m \right] e^{\mathcal{S}_{1D}[\eta, \bar{\eta}]} \end{aligned} \quad (160)$$

where  $\delta\tau = \beta/L$  and  $\eta_{l,m}$  is labelled by a spatial index  $l$  and an imaginary time index  $m$ . Since  $\mathcal{H}_{1D}$  [Eq. 150] is normal ordered, its matrix elements are simply calculated using Eq. 154, and,

$$\mathcal{S}_{1D}[\eta, \bar{\eta}] = \sum_m \left[ -\delta\tau \mathcal{H}_{1D}(\bar{\eta}_{m+1}, \eta_m) - \sum_l \bar{\eta}_{l,m+1}(\eta_{l,m+1} - \eta_{l,m}) \right]. \quad (161)$$

### C.3 Matching the fermionic and Kasteleyn actions

The action,  $\mathcal{S}_{1D}[\eta, \bar{\eta}]$ , exactly reproduces the partition function of the nearest-neighbour TLIAF, but it does this by averaging over some of the degrees of freedom of the Kasteleyn action. In order to make the mapping explicit, it is necessary to introduce these extra degrees of freedom into the quantum path integral.

The microscopic relation between the quantum and classical partition functions requires a correspondence between an imaginary timestep and a translation of the classical system across 4 bonds in the  $y$  direction (see Fig. 32). In the classical set-up the string can hop by a maximum of one 1D lattice site per imaginary timestep, and the expansion of the quantum time-translation operator can therefore be truncated to first order without approximation, giving

$$e^{-\delta\tau \mathcal{H}_{1D}} \rightarrow \mathbb{1} - \delta\tau \mathcal{H}_{1D}. \quad (162)$$

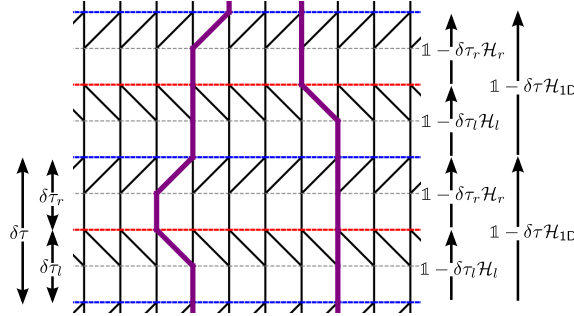


Figure 32: A redrawing of the honeycomb/brick lattice that clarifies the mapping between the nearest-neighbour TLIAF in the constrained manifold and  $\mathcal{H}_{1D}$  [Eq. 150].  $\mathcal{H}_{1D}$  translates the strings/fermions (purple lines) by four bonds, from dashed blue line to dashed blue line (the four possible paths are shown). Knowing the string/fermion configuration only on the blue dashed lines does not completely specify the Ising configuration, since the string can take two possible routes that result in no change in its  $x$  position. As a result, it is necessary to introduce into the coherent-state path integral extra states that take into account the string/fermion configuration on the red dashed lines (see Eq. 165). In order to do this the Hamiltonian is split into  $\mathcal{H}_l$  and  $\mathcal{H}_r$ , describing hopping to the left and right [Eq. 163].

However, it can be seen in Fig. 32 that, if the string configuration is only known every 4 bonds (i.e. on the blue dashed lines in Fig. 32), there is an ambiguity, since a string can take two possible routes that leave its  $x$  coordinate invariant. In terms of the original Ising spins, these two possible routes describe different configurations. In order to explicitly describe all the classical degrees of freedom, it is necessary to consider the translation of a string by only 2 bonds at a time, and therefore the quantum Hamiltonian is split into,

$$\mathcal{H}_l = \sum_l \left[ -(z-1)c_l^\dagger c_l - zc_{l-1}^\dagger c_l \right], \quad \mathcal{H}_r = \sum_l \left[ -(z-1)c_l^\dagger c_l - zc_{l+1}^\dagger c_l \right], \quad (163)$$

where the effect of the non-Hermitian operator  $\mathcal{H}_l$  is to translate from the blue to red dashed lines in Fig. 32, while  $\mathcal{H}_r$  translates from red to blue dashed lines. It is clear from Fig. 32 that  $\mathcal{H}_l$  only includes left-hopping while  $\mathcal{H}_r$  only includes right-hopping. The coefficients of  $\mathcal{H}_l$  and  $\mathcal{H}_r$  have been chosen such that the matrix elements obey the relationship,

$$\langle n_{m+1} | (\mathbb{1} - \delta\tau\mathcal{H}_{1D}) | n_m \rangle = \sum_{\{u\}} \langle n_{m+1} | (\mathbb{1} - \delta\tau_r\mathcal{H}_r) | u \rangle \langle u | (\mathbb{1} - \delta\tau_l\mathcal{H}_l) | n_m \rangle, \quad (164)$$

with  $\{u\}$  a complete set of states in any Hilbert-space basis and  $\delta\tau = \delta\tau_l + \delta\tau_r$ . Furthermore we have set  $\delta\tau_l = \delta\tau_r = 1$  to correspond to the lattice spacing of the classical model.

The splitting of the Hamiltonian can be built into the coherent-state path integral by introducing sets of intermediate coherent states that are associated with the red dashed lines in Fig. 32. These are labelled by  $\theta$ , and the resulting path integral is,

$$\begin{aligned} \mathcal{Z} &= \int \left[ \prod_m d(\bar{\eta}, \eta)_m d(\bar{\theta}, \theta)_m \right] \langle \eta_0 | e^{-\mathcal{H}_r} | \theta_{L-1} \rangle e^{-\sum_l \bar{\theta}_{l,L-1} \theta_{l,L-1}} \\ &\quad \times \langle \theta_{L-1} | e^{-\mathcal{H}_l} | \eta_{L-1} \rangle e^{-\sum_l \bar{\eta}_{l,L-1} \eta_{l,L-1}} \\ &\quad \times \dots \\ &\quad \times \langle \eta_2 | e^{-\mathcal{H}_r} | \theta_1 \rangle e^{-\sum_i \bar{\theta}_{i,1} \theta_{i,1}} \langle \theta_1 | e^{-\mathcal{H}_l} | \eta_1 \rangle e^{-\sum_i \bar{\eta}_{i,1} \eta_{i,1}} \\ &\quad \times \langle \eta_1 | e^{-\mathcal{H}_r} | \theta_0 \rangle e^{-\sum_i \bar{\theta}_{i,0} \theta_{i,0}} \langle \theta_0 | e^{-\mathcal{H}_l} | \eta_0 \rangle e^{-\sum_i \bar{\eta}_{i,0} \eta_{i,0}} \\ &= \int \left[ \prod_m d(\bar{\eta}, \eta)_m d(\bar{\theta}, \theta)_m \right] e^{\mathcal{S}_{1D}[\eta, \bar{\eta}, \theta, \bar{\theta}]}, \end{aligned} \quad (165)$$

where,

$$\mathcal{S}_{1D}[\eta, \bar{\eta}, \theta, \bar{\theta}] = \sum_{l,m} [-\bar{\eta}_{l,m} \eta_{l,m} - \bar{\theta}_{l,m} \theta_{l,m} + z(\bar{\eta}_{l,m+1} \theta_{l,m} + \bar{\eta}_{l+1,m+1} \theta_{l,m} + \bar{\theta}_{l,m} \eta_{l,m} + \bar{\theta}_{l-1,m} \eta_{l,m})]. \quad (166)$$

The fermionic action is now in a form that can be directly compared with the Kasteleyn action  $\mathcal{S}_2[a_1, b_1, a_2, b_2]$  [Eq. 145]. It can be seen that these can be brought to the same form simply by identifying,

$$\eta_{l,m} \rightarrow a_{1,i}, \quad \bar{\eta}_{l,m} \rightarrow b_{1,i}, \quad \theta_{l,m} \rightarrow a_{2,i}, \quad \bar{\theta}_{l,m} \rightarrow b_{2,i}, \quad (167)$$

where there is an equivalence between  $i$ , which labels the unit cells in the 2D lattice, and  $(l, m)$ , which labels the sites and timeslices in the 1D quantum problem. This justifies the mapping between the quantum and classical coefficients stated in the main text in Eq. 35.

#### C.4 Matching the classical and quantum spectrums

As well as showing how the Kasteleyn and fermionic coherent state actions can be brought to the same form, it is also useful to show the link between the spectrums. Since the fermions/strings are free, the partition functions can be simply evaluated by Fourier transform, and the spectrums compared.

The Kasteleyn spectrum is given by  $|e_{\mathbf{p}}^K|$  [Eq. 149], and the partition function,  $\mathcal{Z}_{\text{hon}}$  [Eq. 147] is the product of this spectrum.

The fermionic spectrum is (see Section 4.1.5),

$$\omega_{p_x} = 2t \cos p_x - \mu = 2z^2(\cos p_x - 1) + 1, \quad (168)$$

and this appears in the Fourier transform of  $\mathcal{S}_{1D}[\eta, \bar{\eta}]$  [Eq. 161],

$$\mathcal{S}_{1D}[\eta, \bar{\eta}] = \sum_{\mathbf{p}} \epsilon_{\mathbf{p}}^{1D} \bar{\eta}_{\mathbf{p}} \eta_{\mathbf{p}}, \quad (169)$$

where  $\delta\tau = 2$  has been used,

$$\epsilon_{\mathbf{p}}^{1D} = -\omega_{p_x} e^{ip_y} - 1 + e^{ip_y} \quad (170)$$

and,

$$\bar{\eta}_{\mathbf{p}} = \frac{1}{L^2} \sum_{l,m} \bar{\eta}_{l,m} e^{i(lp_x + mp_y)}, \quad \eta_{\mathbf{p}} = \frac{1}{L^2} \sum_{l,m} \eta_{l,m} e^{-i(lp_x + mp_y)}. \quad (171)$$

Since the action is diagonal, the partition function is just given by,

$$\mathcal{Z}_{1D} = \prod_{\mathbf{p}} \epsilon_{\mathbf{p}}^{1D}. \quad (172)$$

The equivalence between  $\mathcal{Z}_{\text{hon}}$  [Eq. 147] and  $\mathcal{Z}_{1D}$  is now clear since the modes can be matched according to,

$$\epsilon_{\mathbf{p}}^K = -e^{ip_y} \epsilon_{p_x+\pi, -p_y-\pi}^{1D} = -\omega_{p_x+\pi} + e^{ip_y} + 1. \quad (173)$$

In conclusion, there is an exact mapping between the Kasteleyn action and that of the fermionic, coherent-state path integral with Hamiltonian  $\mathcal{H}_{1D}$  [Eq. 150]. This mapping also makes it clear that the Grassmann variables introduced in the Kasteleyn formulation of the classical partition function describe coherent states of strings, and therefore demonstrates the link between the Kasteleyn and transfer matrix approach to solving the nearest-neighbour TLIAF.

## D Perturbative expansion of the action: a simple example

The Grassmann path integral representation of interacting dimer problems, as used in Section 4.3.2, is not unknown [52, 63] but has not been widely explored in the literature. As an aid to the interested reader, we here consider  $\mathcal{Z}_{\text{hon2}}$  [Eq. 61], and show a worked example of how to evaluate this partition function via Grassmann path integration on the simplest, non-trivial lattice: the hexagonal plaquette. This provides useful insights into the construction of a perturbation theory for the infinite lattice, as presented in Section 4.3.2.

We consider the dimer covering of a hexagonal plaquette with a dimer weight of 1 on A bonds,  $z$  on B and C bonds and a dimer interaction with weight  $z_2$  between dimers separated by one unfilled bond (see Fig. 33). For a single plaquette there are only two possible dimer coverings, shown in Fig. 33, and each of these has a weight  $z^2 z_2^3$ . The partition function,  $\mathcal{Z}_{\text{hon2}}$  [Eq. 61], is therefore given by,

$$\mathcal{Z}_{\text{hon2}} = 2z^2 z_2^3 = 2z^2 [(z_2 - 1)^3 + 3(z_2 - 1)^2 + 3(z_2 - 1) + 1], \quad (174)$$



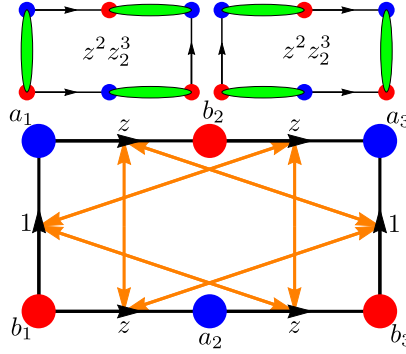


Figure 33: Dimer covering and Grassmann path integral representation of the partition function for the hexagonal plaquette. The interacting dimer model,  $\mathcal{Z}_{\text{hon2}}$  [Eq. 61], has dimer weight 1 on A bonds and  $z$  on B and C bonds, and there is a weight  $z_2$  associated with interactions between dimers separated by a single unfilled bond. (Top) The two dimer coverings of the hexagonal plaquette are shown, along with the associated weights. (Bottom) The partition function can be recast as a path integral over Grassmann variables associated with vertices of the plaquette (red and blue disks). The action consists of 2, 4 and 6 body interactions, and the allowed 4-body interactions are represented as orange arrows connecting pairs of bonds.

where the second equality is an exact rewriting that will prove useful below.

While in such a simple case the partition function can be calculated exactly just by inspection, it is instructive to perform the calculation via the Grassmann path integral representation. On a finite lattice the highest order term in the action is  $\mathcal{S}_{2N}[a, b]$ , where  $2N$  is the number of honeycomb lattice sites, and for the 6-site plaquette the partition function can therefore be rewritten as,

$$\mathcal{Z}_{\text{hon2}} = \int \prod_i da_i db_i e^{\mathcal{S}_2[a, b] + \mathcal{S}_4[a, b] + \mathcal{S}_6[a, b]}, \quad (175)$$

where  $i = \{1, 2, 3\}$ .

The quadratic term in the action does not take into account the  $z_2$  interaction, and is given by,

$$\mathcal{S}_2 = b_1 a_1 + b_3 a_3 + z (a_1 b_2 + b_1 a_2 + b_2 a_3 + a_2 b_3). \quad (176)$$

If the action is truncated at quadratic order, then the usual rules of Grassmann integration can be used to find,

$$\int \prod_i da_i db_i e^{\mathcal{S}_2[a, b]} = 2z^2. \quad (177)$$

Comparison with the exact value of the partition function [Eq. 174] shows that this quadratic approximation becomes exact in the limit  $z_2 - 1 \rightarrow 0$ .

The quartic term in the action takes into account pairwise interactions of the dimers in isolation from other pairwise interactions, and is given by,

$$\mathcal{S}_4 = z(z_2 - 1) (b_1 a_1 b_2 a_3 + b_1 a_1 a_2 b_3 + b_3 a_3 a_1 b_2 + b_3 a_3 b_1 a_2) + z^2 (z_2 - 1) (b_1 a_2 a_1 b_2 + a_2 b_3 b_2 a_3). \quad (178)$$

The factor  $z_2 - 1$  is chosen such that if there were a configuration with only 1 dimer-dimer interaction, the -1 would remove the contribution from the purely quadratic action, while the

$z_2$  would replace this with a contribution that takes the interaction into account. In the case of the hexagonal plaquette the allowed dimer configurations contain 3 mutually interacting dimers, and this mutual interaction is not fully taken into account by the quartic term. Direct evaluation results in,

$$\int \prod_i da_i db_i e^{\mathcal{S}_2[a,b] + \mathcal{S}_4[a,b]} = 2z^2 [3(z_2 - 1) + 1], \quad (179)$$

reproducing the exact partition function [Eq. 174] to first order in  $z_2 - 1$ .

Finally, the hexatic term takes into account the fact that the dimers are not interacting in isolation, but are all mutually interacting, and is given by,

$$\begin{aligned} \mathcal{S}_6 &= z^2 [z_2^3 - 3(z_2 - 1) - 1] (b_1 a_1 b_2 a_3 a_2 b_3 + b_1 a_2 a_1 b_2 a_3 b_3) \\ &= z^2 [(z_2 - 1)^3 + 3(z_2 - 1)^2] (b_1 a_1 b_2 a_3 a_2 b_3 + b_1 a_2 a_1 b_2 a_3 b_3), \end{aligned} \quad (180)$$

where in the first line the  $-1$  removes the contribution from the quadratic action, the  $3(z_2 - 1)$  removes the contribution from the quartic action and the  $z_2^3$  replaces these with a contribution that correctly reproduces the weight of three mutually interacting dimers. Direct calculation including quadratic, quartic and hexatic terms correctly reproduces Eq. 174 for the partition function,

$$\int \prod_i da_i db_i e^{\mathcal{S}_2[a,b] + \mathcal{S}_4[a,b] + \mathcal{S}_6[a,b]} = 2z^2 [(z_2 - 1)^3 + 3(z_2 - 1)^2 + 3(z_2 - 1) + 1] = 2z^2 z_2^3. \quad (181)$$

As the lattice size is increased, it rapidly becomes impossible to determine the partition function by inspection. A full expansion of the partition function in terms of Grassmann variables also becomes complicated due to the increase in the number of terms in the action. However, the advantage of this method is that it provides a way of systematically carrying out perturbation theory around the non-interacting limit  $|z_2 - 1| \rightarrow 0$ . For large or infinite lattices direct evaluation of Grassmann actions with quartic and higher order interacting terms is not possible, but approximate diagrammatic methods can be used, and the order of expansion matched to that of the truncation of the action.

## References

- [1] C. Lacroix, P. Mendels and F. Mila, *Introduction to Frustrated Magnetism*, Springer (2011).
- [2] G. H. Wannier, *Antiferromagnetism. the triangular ising net*, Phys. Rev. **79**, 357 (1950), doi:10.1103/PhysRev.79.357.
- [3] R. Houtappel, *Order-disorder in hexagonal lattices*, Physica **16**(5), 425 (1950), doi:http://dx.doi.org/10.1016/0031-8914(50)90130-3.
- [4] J. Stephenson, *Ising-model spin correlations on the triangular lattice*, Journal of Mathematical Physics **5**(8), 1009 (1964), doi:http://dx.doi.org/10.1063/1.1704202.

- [5] J. Stephenson, *Ising-model spin correlations on the triangular lattice. iii. isotropic antiferromagnetic lattice*, Journal of Mathematical Physics **11**(2), 413 (1970), doi:http://dx.doi.org/10.1063/1.1665154.
- [6] S. Samuel, *The use of anticommuting variable integrals in statistical mechanics. i. the computation of partition functions*, Journal of Mathematical Physics **21**(12), 2806 (1980), doi:http://dx.doi.org/10.1063/1.524404.
- [7] J. Glosli and M. Plischke, *A monte carlo and renormalization group study of the ising model with nearest and next nearest neighbor interactions on the triangular lattice*, Canadian Journal of Physics **61**(11), 1515 (1983), doi:10.1139/p83-197.
- [8] T. Takagi and M. Mekata, *New partially disordered phases with commensurate spin density wave in frustrated triangular lattice*, Journal of the Physical Society of Japan **64**(12), 4609 (1995), doi:10.1143/JPSJ.64.4609.
- [9] E. Rastelli, S. Regina and A. Tassi, *Monte carlo simulations on a triangular ising antiferromagnet with nearest and next-nearest interactions*, Phys. Rev. B **71**, 174406 (2005), doi:10.1103/PhysRevB.71.174406.
- [10] S. E. Korshunov, *Nature of phase transitions in the striped phase of a triangular-lattice ising antiferromagnet*, Phys. Rev. B **72**, 144417 (2005), doi:10.1103/PhysRevB.72.144417.
- [11] A. Smerald, S. Korshunov and F. Mila, *Topological aspects of symmetry breaking in triangular-lattice ising antiferromagnets*, Phys. Rev. Lett. **116**, 197201 (2016), doi:10.1103/PhysRevLett.116.197201.
- [12] E. Mengotti, L. J. Heyderman, A. Bisig, A. Fraile Rodríguez, L. Le Guyader, F. Nolting and H. B. Braun, *Dipolar energy states in clusters of perpendicular magnetic nanoislands*, Journal of Applied Physics **105**(11), 113113 (2009).
- [13] O. Sendetskyi, N. Leo and L. Heyderman, Private communication.
- [14] R. F. Wang, C. Nisoli, R. S. Freitas, J. Li, W. McConville, B. J. Cooley, M. S. Lund, N. Samarth, C. Leighton, V. H. Crespi and P. Schiffer, *Artificial /‘spin ice/’ in a geometrically frustrated lattice of nanoscale ferromagnetic islands*, Nature **439**(7074), 303 (2006).
- [15] M. Tanaka, E. Saitoh, H. Miyajima, T. Yamaoka and Y. Iye, *Magnetic interactions in a ferromagnetic honeycomb nanoscale network*, Phys. Rev. B **73**, 052411 (2006), doi:10.1103/PhysRevB.73.052411.
- [16] Y. Qi, T. Brintlinger and J. Cumings, *Direct observation of the ice rule in an artificial kagome spin ice*, Phys. Rev. B **77**, 094418 (2008), doi:10.1103/PhysRevB.77.094418.
- [17] E. Mengotti, L. J. Heyderman, A. Fraile Rodríguez, A. Bisig, L. Le Guyader, F. Nolting and H. B. Braun, *Building blocks of an artificial kagome spin ice: Photoemission electron microscopy of arrays of ferromagnetic islands*, Phys. Rev. B **78**, 144402 (2008), doi:10.1103/PhysRevB.78.144402.

- [18] E. Mengotti, L. J. Heyderman, A. F. Rodriguez, F. Nolting, R. V. Hugli and H.-B. Braun, *Real-space observation of emergent magnetic monopoles and associated dirac strings in artificial kagome spin ice*, Nat Phys **7**(1), 68 (2011).
- [19] J. P. Morgan, A. Stein, S. Langridge and C. H. Marrows, *Thermal ground-state ordering and elementary excitations in artificial magnetic square ice*, Nat Phys **7**(1), 75 (2011).
- [20] L. J. Heyderman and R. L. Stamps, *Artificial ferroic systems: novel functionality from structure, interactions and dynamics*, Journal of Physics: Condensed Matter **25**(36), 363201 (2013).
- [21] C. Nisoli, R. Moessner and P. Schiffer, *Colloquium*, Rev. Mod. Phys. **85**, 1473 (2013), doi:10.1103/RevModPhys.85.1473.
- [22] A. Farhan, P. M. Derlet, A. Kleibert, A. Balan, R. V. Chopdekar, M. Wyss, J. Perron, A. Scholl, F. Nolting and L. J. Heyderman, *Direct observation of thermal relaxation in artificial spin ice*, Phys. Rev. Lett. **111**, 057204 (2013), doi:10.1103/PhysRevLett.111.057204.
- [23] J. Cumings, L. J. Heyderman, C. H. Marrows and R. L. Stamps, *Focus on artificial frustrated systems*, New Journal of Physics **16**(7), 075016 (2014).
- [24] L. Anghinolfi, H. Luetkens, J. Perron, M. G. Flokstra, O. Sendetskyi, A. Suter, T. Prokscha, P. M. Derlet, S. L. Lee and L. J. Heyderman, *Thermodynamic phase transitions in a frustrated magnetic metamaterial*, Nature Communications **6**, 8278 EP (2015).
- [25] O. Sendetskyi, L. Anghinolfi, V. Scagnoli, G. Möller, N. Leo, A. Alberca, J. Kohlbrecher, J. Lüning, U. Staub and L. J. Heyderman, *Magnetic diffuse scattering in artificial kagome spin ice*, Phys. Rev. B **93**, 224413 (2016), doi:10.1103/PhysRevB.93.224413.
- [26] J. W. Britton, B. C. Sawyer, A. C. Keith, C. C. J. Wang, J. K. Freericks, H. Uys, M. J. Biercuk and J. J. Bollinger, *Engineered two-dimensional ising interactions in a trapped-ion quantum simulator with hundreds of spins*, Nature **484**(7395), 489 (2012).
- [27] A. Smerald and F. Mila, *Disorder-driven spin-orbital liquid behavior in the  $\text{Ba}_3\text{Vsb}_2\text{O}_9$  materials*, Phys. Rev. Lett. **115**, 147202 (2015), doi:10.1103/PhysRevLett.115.147202.
- [28] S. Mahmoudian, L. Rademaker, A. Ralko, S. Fratini and V. Dobrosavljević, *Glassy dynamics in geometrically frustrated coulomb liquids without disorder*, Phys. Rev. Lett. **115**, 025701 (2015), doi:10.1103/PhysRevLett.115.025701.
- [29] P. W. Kasteleyn, *Dimer statistics and phase transitions*, Journal of Mathematical Physics **4**(2), 287 (1963), doi:http://dx.doi.org/10.1063/1.1703953.
- [30] M. E. Fisher, *On the dimer solution of planar ising models*, Journal of Mathematical Physics **7**(10), 1776 (1966), doi:http://dx.doi.org/10.1063/1.1704825.
- [31] C. S. O. Yokoi, J. F. Nagle and S. R. Salinas, *Dimer pair correlations on the brick lattice*, Journal of Statistical Physics **44**(5), 729, doi:10.1007/BF01011905.

- [32] Y. Jiang and T. Emig, *Ordering of geometrically frustrated classical and quantum triangular ising magnets*, Phys. Rev. B **73**, 104452 (2006), doi:10.1103/PhysRevB.73.104452.
- [33] O. F. Syljuåsen and A. W. Sandvik, *Quantum monte carlo with directed loops*, Phys. Rev. E **66**, 046701 (2002), doi:10.1103/PhysRevE.66.046701.
- [34] A. W. Sandvik and R. Moessner, *Correlations and confinement in non-planar two-dimensional dimer models*, Phys. Rev. B **73**, 144504 (2006), doi:10.1103/PhysRevB.73.144504.
- [35] F. Alet, Y. Ikhlef, J. L. Jacobsen, G. Misguich and V. Pasquier, *Classical dimers with aligning interactions on the square lattice*, Phys. Rev. E **74**, 041124 (2006), doi:10.1103/PhysRevE.74.041124.
- [36] W. Zhang, T. M. Garoni and Y. Deng, *A worm algorithm for the fully-packed loop model*, Nuclear Physics B **814**(3), 461 (2009), doi:http://dx.doi.org/10.1016/j.nuclphysb.2009.01.007.
- [37] Q. Liu, Y. Deng and T. M. Garoni, *Worm monte carlo study of the honeycomb-lattice loop model*, Nuclear Physics B **846**(2), 283 (2011), doi:http://dx.doi.org/10.1016/j.nuclphysb.2011.01.003.
- [38] G. Rakala and K. Damle, *Cluster algorithms for frustrated two dimensional Ising anti-ferromagnets via dual worm constructions* 1612.00851.
- [39] A. Grzybowski, E. Gwózdź and A. Bródka, *Ewald summation of electrostatic interactions in molecular dynamics of a three-dimensional system with periodicity in two directions*, Phys. Rev. B **61**, 6706 (2000), doi:10.1103/PhysRevB.61.6706.
- [40] U. K. Rößler, *Ising dipoles on the triangular lattice*, Journal of Applied Physics **89**(11), 7033 (2001), doi:http://dx.doi.org/10.1063/1.1358336.
- [41] V. L. Pokrovsky and A. L. Talapov, *Ground state, spectrum, and phase diagram of two-dimensional incommensurate crystals*, Phys. Rev. Lett. **42**, 65 (1979), doi:10.1103/PhysRevLett.42.65.
- [42] V. L. Pokrovsky and A. L. Talapov, Zh. Eksp. Teor. Fiz **78**, 269 (1980).
- [43] A. Ioselevich, D. A. Ivanov and M. V. Feigelman, *Ground-state properties of the rokhsar-kivelson dimer model on the triangular lattice*, Phys. Rev. B **66**, 174405 (2002), doi:10.1103/PhysRevB.66.174405.
- [44] P. Fendley, R. Moessner and S. L. Sondhi, *Classical dimers on the triangular lattice*, Phys. Rev. B **66**, 214513 (2002), doi:10.1103/PhysRevB.66.214513.
- [45] S. Samuel, *The use of anticommuting variable integrals in statistical mechanics. ii. the computation of correlation functions*, Journal of Mathematical Physics **21**(12), 2815 (1980), doi:10.1063/1.524405.
- [46] D. A. Huse and M. E. Fisher, *Commensurate melting, domain walls, and dislocations*, Phys. Rev. B **29**, 239 (1984), doi:10.1103/PhysRevB.29.239.

- [47] Villain, J. and Bak, P., *Two-dimensional ising model with competing interactions : floating phase, walls and dislocations*, J. Phys. France **42**(5), 657 (1981), doi:10.1051/jphys:01981004205065700.
- [48] P. Bak, *Commensurate phases, incommensurate phases and the devil's staircase*, Reports on Progress in Physics **45**(6), 587 (1982).
- [49] T. Bohr, *Dislocations in the commensurate-incommensurate transition*, Phys. Rev. B **25**, 6981 (1982), doi:10.1103/PhysRevB.25.6981.
- [50] S. B. Rutkevich, *Spin - spin correlation function for the free-fermion model: crossover from two-dimensional ising to pokrovsky - talapov critical behaviour*, Journal of Physics A: Mathematical and General **30**(11), 3883 (1997).
- [51] A. Y. Kitaev, *Unpaired majorana fermions in quantum wires*, Physics-Uspekhi **44**(10S), 131 (2001).
- [52] S. Samuel, *The use of anticommuting variable integrals in statistical mechanics. iii. unsolved models*, Journal of Mathematical Physics **21**(12), 2820 (1980), doi:http://dx.doi.org/10.1063/1.524406.
- [53] S. M. Bhattacharjee and J. F. Nagle, *Finite-size effect for the critical point of an anisotropic dimer model of domain walls*, Phys. Rev. A **31**, 3199 (1985), doi:10.1103/PhysRevA.31.3199.
- [54] H. J. Schulz, *Critical behavior of commensurate-incommensurate phase transitions in two dimensions*, Phys. Rev. B **22**, 5274 (1980), doi:10.1103/PhysRevB.22.5274.
- [55] T. Giamarchi, *Quantum Physics in One Dimension*, Oxford University Press (2004).
- [56] V. Emery and S. Kivelson, *Frustrated electronic phase separation and high-temperature superconductors*, Physica C: Superconductivity **209**(4), 597 (1993), doi:http://dx.doi.org/10.1016/0921-4534(93)90581-A.
- [57] U. Löw, V. J. Emery, K. Fabricius and S. A. Kivelson, *Study of an ising model with competing long- and short-range interactions*, Phys. Rev. Lett. **72**, 1918 (1994), doi:10.1103/PhysRevLett.72.1918.
- [58] S. M. Bhattacharjee and F. Seno, *A measure of data collapse for scaling*, Journal of Physics A: Mathematical and General **34**(33), 6375 (2001).
- [59] J. L. Jacobsen and H. C. Fogedby, *Monte carlo study of correlations near the ground state of the triangular antiferromagnetic ising model*, Physica A: Statistical Mechanics and its Applications **246**(3-4), 563 (1997), doi:https://doi.org/10.1016/S0378-4371(97)00323-3.
- [60] S. Powell and J. T. Chalker, *Classical to quantum mappings for geometrically frustrated systems: Spin-ice in a [100] field*, Phys. Rev. B **78**, 024422 (2008), doi:10.1103/PhysRevB.78.024422.
- [61] S. Powell and J. T. Chalker, *Classical to quantum mapping for an unconventional phase transition in a three-dimensional classical dimer model*, Phys. Rev. B **80**, 134413 (2009), doi:10.1103/PhysRevB.80.134413.

- [62] A. Altland and B. Simons, *Condensed Matter Field Theory*, Cambridge University Press (2010).
- [63] M. Clusel, J.-Y. Fortin and V. N. Plechko, *Alternative description of the 2d blume–capel model using grassmann algebra*, *Journal of Physics A: Mathematical and Theoretical* **41**(40), 405004 (2008).